

ABSTRACT

Title of Dissertation: EXPERIMENTAL DEMONSTRATION OF
 LIGHT TRAPPING AND INTERNAL
 LIGHT SCATTERING IN SOLAR CELLS

Joseph B. Murray, Doctor of Philosophy,
2016

Dissertation directed by: Professor Jeremy N. Munday

 Department of Electrical and Computer
 Engineering

Renewable energy technologies have long-term economic and environmental advantages over fossil fuels, and solar power is the most abundant renewable resource, supplying 120 PW over earth's surface. In recent years the cost of photovoltaic modules has reached grid parity in many areas of the world, including much of the USA. A combination of economic and environmental factors has encouraged the adoption of solar technology

and led to an annual growth rate in photovoltaic capacity of 76% in the US between 2010 and 2014.

Despite the enormous growth of the solar energy industry, commercial unit efficiencies are still far below their theoretical limits. A push for thinner cells may reduce device cost and could potentially increase device performance. Fabricating thinner cells reduces bulk recombination, but at the cost of absorbing less light. This tradeoff generally benefits thinner devices due to reduced recombination. The effect continues up to a maximum efficiency where the benefit of reduced recombination is overwhelmed by the suppressed absorption. Light trapping allows the solar cell to circumvent this limitation and realize further performance gains (as well as continue cost reduction) from decreasing the device thickness.

This thesis presents several advances in experimental characterization, theoretical modeling, and device applications for light trapping in thin-film solar cells. We begin by introducing light trapping strategies and discuss theoretical limits of light trapping in solar cells. This is followed by an overview of the equipment developed for light trapping characterization. Next we discuss our recent work measuring internal light scattering and a new model of scattering to predict the effects of dielectric nanoparticle back scatterers on thin-film device absorption. The new model is extended and generalized to

arbitrary stacks of stratified media containing scattering structures. Finally, we investigate an application of these techniques using polymer dispersed liquid crystals to produce switchable solar windows. We show that these devices have the potential for self-powering.

EXPERIMENTAL DEMONSTRATION OF LIGHT TRAPPING AND
INTERNAL LIGHT SCATTERING IN SOLAR CELLS

by

Joseph B. Murray

Dissertation submitted to the Faculty of the Graduate School of the
University of Maryland, College Park, in partial fulfillment
of the requirements for the degree of

Doctor of Philosophy

2016

Advisory Committee:

Professor Jeremy N. Munday, Chair

Professor Christopher Davis

Professor Thomas Murphy

Professor Martin Peckerar

Professor Lourdes Salamanca-Riba

© Copyright by

Joseph B Murray

2016

Dedication

I dedicate this work to my wife Sarah and our baby boy Gus.

Acknowledgements

First and foremost, I would like to thank and acknowledge my advisor Jeremy Munday who has supported me throughout my time at the University of Maryland. Professor Munday has always been incredibly generous with his time, insight, and attention. I would also like to thank all of the members of Professor Munday's group for their help throughout my studies. In particular, I would like to thank Lisa Krayner, Dakang Ma, Joe Garret, Dongheon Ha, David Somers, Tao Gong and Dan Goldman for their assistance in editing this thesis. Joe Garret was also of great help with AFM measurements. To my officemates Tao Gong, Yunlu Xu, and Dongheon Ha, thank you for the numerous discussions we have had over the past five years, particularly those regarding calculations and for helping to generate new ideas.

Outside of our lab, many others at UMD have been instrumental to this work. I am grateful for the cleanroom staff, who generously provided training and support and freely shared expertise. I am also grateful to Professor Leite for her advice and generosity in sharing resources. I would also like to acknowledge her students Beth Tennyson and Chen Gong for their help with equipment.

Table of Contents

Dedication	ii
Acknowledgements	iii
Table of Contents	iv
List of Tables	ix
List of Figures	x
List of Publications.....	xiv
Chapter 1: Introduction.....	1
1.1. Light management techniques.....	3
1.2. Strategies for light trapping.....	5
1.2.1. Thin-film coatings.....	6
1.2.2. Texturing.....	8
1.2.3. Metallic nanostructures.....	8
1.2.4. Dielectric nanostructures	9
1.3. Considerations for diffuse/indirect illumination.....	11
1.4. Outline of this thesis	12
Chapter 2: Light trapping limits	15
2.1. Introduction to light trapping.....	15

2.2. The $4n^2$ limit	16
2.2.1. Assumption 1: ergodicity	16
2.2.3. Assumption 2: thick slab	17
2.2.4 Assumption 3: weak absorption	18
2.2.5. Regimes of validity	18
2.3. Limiting Cases	20
2.3.1. Waveguide approach.....	20
2.3.2. The local density of optical states approach	22
2.3.3. Rigorous coupled-mode theory approach	24
2.4. Exceeding the $4n^2$ limit	27
2.4.1. Waveguide approach.....	28
2.4.2. LDOS approach	30
2.4.3. Rigorous coupled-mode approach	32
2.4.4. Non-random scattering	34
2.4. Conclusions.....	37
Chapter 3: Instrumentation	39
3.1. Multipurpose Spectroscopy Station overview.....	40
3.1.1. Monochromatic light source and beam conditioning optics	41
3.1.2. Integrating sphere and EQE stage	47

3.1.3. MSS Signal processing and driving electronics	50
3.1.4. LabVIEW front end	60
3.1.5. Measurement details	66
3.2. Scattering Distribution Station overview	69
3.2.1. SDS mechanical hardware	71
3.2.2. SDS electrical	74
3.2.3. LabVIEW frontend	75
3.3. High Voltage Square Wave Drive	83
3.4. Instrumentation applications	86
Chapter 4: Experimental demonstration of internal light scattering	88
4.1. Overview	88
4.2. Modeling of random dielectric scatterers	91
4.3. Measurement of the scattering profile within a material	97
4.3. Measured and calculated absorption	107
4.4. Discussion	114
Chapter 5: A generalized approach to modeling absorption with light scattering structures	116
5.1. Calculating total absorption	118
5.2. Calculating absorption in individual layers	124

5.3. Special cases	133
5.3. Numerical demonstrations	138
5.4. Conclusions.....	144
5.5. Summary of special cases and variables.....	145
Chapter 6: Electrically controllable light trapping.....	149
6.1. Self-powered switchable solar windows.....	150
6.2. Fabrication methods and experimental details	164
6.2.1. Sample preparation.....	165
6.2.2. Material characterization	165
6.2.3. Calculating absorption	169
6.2.4. Calculating power generation.....	170
6.2.5. Characterizing scattering	172
6.3. Discussion	175
Chapter 7: Conclusions and outlook.....	177
7.1. Enhancements to PDLC switchable solar windows.....	178
7.2. Improvement of model for absorption with scattering layers	182
7.3. Integrating sphere measurement with liquid immersion.....	183
Appendices	189
APPENDIX A: Chopper driver source code	189

APPENDIX B: Integrated motor controller source code	227
APPENDIX C: Multipurpose spectroscopy station SOP	246
Bibliography	255

List of Tables

Table 5.1: Absorption modelling of special cases.....	137
Table 5.2: Table of additional special cases	146
Table 5.3: Table of variables for absorption modelling	147

List of Figures

Figure 1.1: Effect of device thickness on performance.	5
Figure 2.1: Dispersion diagram for modes available to P3HT:PCBM structures	30
Figure 2.2: Comparing limits of absorption in a polymer/metal waveguide.	32
Figure 2.3: Surpassing the ergodic limit through non-Lambertian scattering.	37
Figure 3.1: Overview of MSS.....	41
Figure 3.2: Overview of MSS optics.	45
Figure 3.3: Integrating sphere parts.	49
Figure 3.4: MSS control board.	55
Figure 3.5: MSS control box.	59
Figure 3.6: LabVIEW frontend for MSS system.....	61
Figure 3.7: Schematic of the absorption measurement sequence.....	69
Figure 3.8: Image showing basic operation of the Scattering Distribution Station.	70
Figure 3.9: DSS mechanical components.	72
Figure 3.10: Image of the LabVIEW frontend used to control the SDS.....	76

Figure 3.11: LabVIEW frontend for the SDS variant.....	79
Figure 3.12: Basic alignment procedure for planar structures when using the SDS.	81
Figure 3.13: Basic alignment procedure for hemispherical structures when using the SDS.....	82
Figure 3.14: H-bridge configurations.	85
Figure 3.15: Implementation of the High Voltage Square Wave Drive.	86
Figure 4.1: Scattering profiles within an absorbing slab	92
Figure 4.2: Absorption in a GaP slab with barium sulfate scattering particles.	96
Figure 4.3: Schematic showing the collection of scattered light.....	99
Figure 4.4: Internal scattering distributions.	101
Figure 4.5: Normalized scattering intensity measurements	106
Figure 4.6: Comparison of modeled and measured absorption.....	113
Figure 5.1: Schematic of structure containing a scattering layer.....	123
Figure 5.2: Schematic of the electric field components in each layer	128
Figure 5.3: Numbering scheme for a generic stack of coherent and incoherent layers.....	131
Figure 5.4: Examples of absorption calculated in individual layers.....	141

Figure 5.5: Experimentally determined total absorption	144
Figure 6.1. Switchable solar cell image and schematic.	153
Figure 6.2. Absorption and power generation of switchable solar windows.	156
Figure 6.3. Electrical characteristics of the PDLC switchable self-powered solar window.....	159
Figure 6.4. (a) Transmission spectra for the PDLC switchable solar windows	161
Figure 6.5. Switchable smart solar window at 45 degree illumination.	164
Figure 6.6. Thin-film absorption measurements and modeling.....	168
Figure 6.7. PDLC characterization.....	168
Figure 6.8 AFM step height measurements used to determine thickness	169
Figure 6.9: Modeled performance of solar cells.....	171
Figure 6.10: Determination of the scattering within a PDLC device.....	173
Figure 7.1: Potential design for a fully functional PDLC/solar cell device....	179
Figure 7.2: Potential avenues for optimization of the switchable solar cell .	182
Figure 7.3: Schematic view of the diffuse absorptivity liquid immersion experiment.	185

List of Publications

Portions of this thesis have been drawn from the following publications:

J. Murray & J. N. Munday. Experimental demonstration and modeling of the internal light scattering profile within solar cells due to random dielectric scatterers. *J. Appl. Phys.* 119, 023104 (2016).

J. Murray & J. N. Munday. Electrically controllable light trapping for self-powered switchable solar windows. *Submitted* (2016).

J. Murray & J. N. Munday. A generalized approach to modeling absorption and photocurrent in solar cells with light scattering structures. *Submitted* (2016).

J. Murray & J. N. Munday. Light trapping principles and limits for photovoltaics. *Submitted* (2016).

D. Ha, **J. Murray**, Z. Fang, L. Hu & J. N. Munday. Advanced Broadband Antireflection Coatings Based on Cellulose Microfiber Paper. *IEEE J. Photovolt.* 5, 577–583 (2015).

C. Preston, Z. Fang, **J. Murray**, H. Zhu, J. Dai, J. N. Munday, & L. Hu. Silver nanowire transparent conducting paper-based electrode with high optical haze. *J. Mater. Chem. C* 2, 1248–1254 (2014).

Y. Xu, **J. Murray** & J. N. Munday. in *Quantum Dot Solar Cells* 349–382 (Springer New York, 2014).

Chapter 1: Introduction

Recent decades have seen tremendous advancements in photovoltaics (PV) both in terms of research and market expansion. Solar markets have expanded at a rate of 45% per year over the past two decades. In recent years solar has made up the majority of new renewable energy capacity, both globally and in the US [1], [2]. Domestically, solar capacity exceeded 20 GW in 2015 and 14.5 GW are projected to come on-line in 2016 [3], [4]. In 2014, 0.8% of all energy in the US was produced by solar.

While this is partly driven by a general interest in renewable resources to decrease the pace of climate change, solar energy has been driven primarily by more immediate, practical concerns. Recently, some localities have surpassed grid parity (the point where power produced by solar energy is equal in cost to power generated by traditional means), and the a large majority of the rest of the world is expected to follow by 2020 [5]. By 2035 the price of solar is expected to drop to half of its 2006 value from \$3.8/W in 2006 to \$1.78/W in 2035, driving expected global capacity to >650 GW [6]. Part of this growth is propelled by its abundance, which greatly exceeds any other renewable with 120 PW of power arriving at the earth's surface [7] and by the overlap of peak solar output with peak electricity demand [8]. Thus for future scenarios of very

high penetrations of renewable energy (90%), solar would be projected make up ~20% of all capacity [8].

Despite the enormous market growth and resources devoted to solar energy, there are still many opportunities for significant advancement. In general there is a push for thinner cells, which may reduce device cost and increase device performance. Thinner cells benefit from reduced bulk recombination but at the expense of decreased absorption. To further improve device efficiency, one needs to either make higher quality material (*i.e.* reduce bulk recombination) or increase light absorption (*e.g.* light trapping). Light trapping allows the solar cell to circumvent this limitation and realize further performance gains (as well as continue cost reduction) from decreasing the device thickness [9]–[11].

It may seem that light trapping could improve the performance of photovoltaics until some structural constraint was reached; however, light trapping is itself constrained. The traditional limit for this phenomenon was developed in 1982 by Yablonovich and Cody [9]. They demonstrated that absorption due to lighted trapping is limited to, what is now known as the $4n^2$ *limit*. This value, which represents the path length enhancement for light rays propagating through the material, can be very large. In silicon, for example, this value equates to approximately a 50-fold increase in the path length. Thus

a thin slab with light trapping can absorb the same amount of light as a slab that is 50 times thicker that does not have light trapping.

In order to actually implement light trapping, a large variety of strategies have been proposed and/or demonstrated. These may be implemented as structures on the front of the cell, as back reflectors or by integrating scattering sites into the absorber itself. The light trapping might be accomplished with surface roughening, random dielectrics, plasmonics, gratings, emission by quantum dots, etc. This wide variety might make it difficult to compare them or to consider how well a given type might perform. However, by considering the limits of light trapping, some headway can be made.

1.1. Light management techniques

Absorption enhancement through light trapping was originally motivated by a need to increase the near bandgap absorption of bulk, indirect absorbers. However, as solar cell development moved toward thinner devices, light trapping became more critical across the entire spectrum. Thinner devices provide several benefits including reduced material costs, improved charge separation through the possibility of increased field gradients, and reduced bulk recombination due to less material use. These benefits come at the cost of

reduced absorption, thus increasing the need for effective light trapping. Figure 1.1 shows the ideal short circuit current density, J_{sc} , for various photovoltaic materials calculated for either a single pass through the material (solid lines) or for absorption at the $4n^2$ limit (dashed lines). In this limit, the fraction of the incident light absorbed is calculated as [9]:

$$A = \frac{4n^2\alpha h}{[4n^2\alpha h + 1]} \quad (1.1)$$

where, h is the thickness of the slab, n is the real part of the refractive index of the material, and α is the absorption coefficient. Eq (1.1) assumes weak absorption, a perfect anti-reflection coating, and a small dependence of transmission on angle (as described in the following chapter). For all the films in Fig. 1.1, the maximum current density, even with enhanced absorption, is significantly below the bulk absorption value when the materials are thinner than ~100 nm. The difference is even more dramatic for silicon and P3HT (used here as a proxy for the P3HT:PCBM blend, which is a common polymer solar cell composite). These results illustrate the need for improved light trapping in nearly all of the common thin-film technologies. In addition, Fig. 1.1b illustrates tradeoff between film thickness and efficiency. Here the efficiency of the GaAs cell is calculated including Auger recombination. Again, the dashed line is for no light trapping (single pass) and the solid line gives the efficiency at the $4n^2$ limit. Perhaps surprisingly the efficiency initially

improves as the device becomes thinner. This is because the bulk GaAs cell will absorb nearly all the light but will have greater non-radiative recombination. The cell continues to improve by reducing the thickness of the GaAs until the benefit of lower recombination no longer outweighs the lower absorption. However, further improvements in light trapping can allow for a thinner cell while maintaining high absorption.

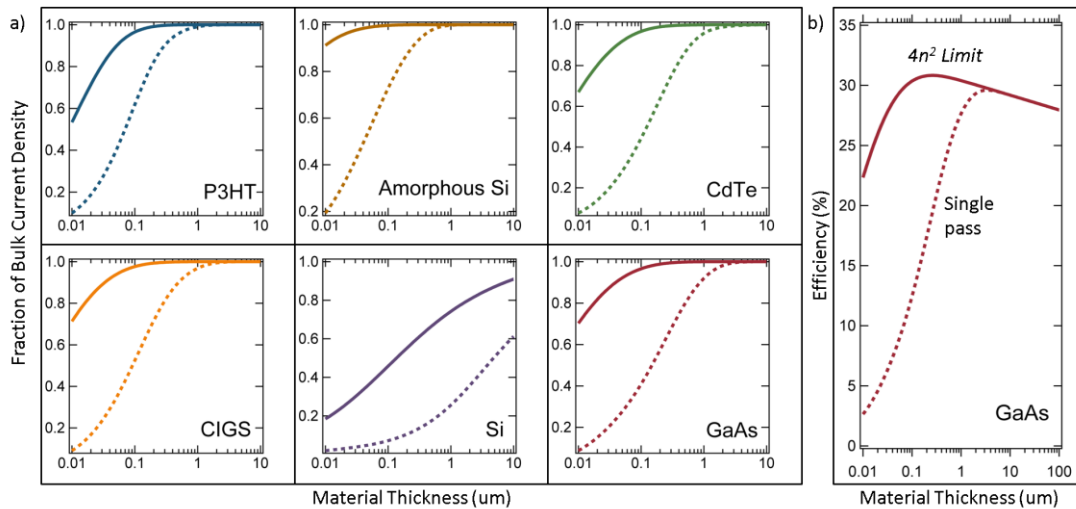


Figure 1.1: Effect of device thickness on performance. For thin-film semiconductors, absorption at the $4n^2$ limit may not be enough. Short-circuit current density vs thickness for various solar cell materials with absorption calculated for either a single pass (solid) or for absorption at the $4n^2$ limit (dashes). In both cases, it is assumed that light is perfectly coupled into the structure.

1.2. Strategies for light trapping

A brief review is presented in order to create a clear overview of light trapping and practical applications. The next sub-sections outline some traditional methods for improving light trapping and more recent advances.

1.2.1. Thin-film coatings

The simplest and perhaps the most common method to increase absorption is the application of an anti-reflection coating (ARC). For this implementation, an additional thin ARC coating is applied to the device with a thickness and refractive index such that the optical thickness of the coating is one quarter wavelength. This results in light reflected from the surface of the ARC and light reflected from the ARC/device interface being out of phase by 180 degrees (negative interference), creating zero reflected field. With the optical thickness of the coating maintained at a quarter wavelength, the ideal index for the ARC is given by the requirement that the amplitude of the two waves are equal, thus:

$$n_{\text{ideal}} = \sqrt{n_{\text{device}}} \quad (1.2)$$

This resonant effect is, however, by nature, limited to a small band of wavelengths and/or incident angles. Designing where this band lies in the solar spectrum is a matter of optimization based on the incident spectrum and on the absorption spectrum. Additional reflection minima can be created with the addition of multiple layers of ARC of varied indices. With several minima, the anti-reflection effect can cover the entire absorption spectrum of a device. In depth analysis of these thin-film structures can be found in many optics texts (see [12] for instance).

Another approach to reduce the reflection losses is to use a graded index layer above the device. With respect to anti-reflection, two small steps in index is better than one large step. This is in fact one of the benefits of the traditional ARC. However, unlike the traditional ARC, a graded index ARC is not (unless specifically designed as such) a resonant structure so it is inherently broad band and has less angular selectivity. This principle can be used either by applying several coatings with progressively lower refractive index or by using some method to continuously change the index from that of the device to that of air. The former may ostensibly be accomplished by choosing several dielectrics with a variety of indices between that of air and that of the absorber. However, producing low index films to act as the first layer can be challenging. Generally this is done by taking an existing low index material such as SiO_2 and creating nano-occlusions in it to produce a low index porous material comprised of air and the chosen substance. Broadband ARC coatings with exceptionally low reflection have been produced in this way [13]–[18]. The ultimate limit of this approach is continuous grading. There has been several theoretical investigations of optimal grading index profiles [19]–[22] demonstrating different advantages such as bandwidth or angle independence.

1.2.2. Texturing

Light trapping by texturing can broadly be divided into two categories: texturing where the feature size is smaller than the wavelength of the light or larger. The former will be discussed below with dielectric nanostructures. The latter is a very common light trapping strategy, which relies on two effects. When employed on the front surface of a device, a textured surface allows for multiple reflections, increasing the likelihood of transmission into the device. When texturing is employed either on the front or rear surface, it can allow light to scatter into otherwise inaccessible angles for a planar slab (beyond the critical angle). These rays scattered into large angles (or waves travelling with large in-plane k -vectors), have exponentially higher absorption, and cannot escape through a planar surface.

1.2.3. Metallic nanostructures

Another possibility for light trapping that has drawn significant attention is the use of metallic nanoparticles. There are several advantages to this method. The first is scattering, which in the simple case just increases the average path length, increasing absorption. However, metals allow for scattering into optical modes of the absorber that would not otherwise be accessible. This includes plasmonic modes, photonic modes outside of the critical angle (forbidden k -vectors) and lossy surface modes [23], [24]. The large number of

short range modes leads to very high fields in small volumes and allows for reduced device thicknesses. Because the absorption is proportional to the field intensity, this behavior results in high absorption. Further, scattering is achieved, in contrast to traditional texturing, without changing the morphology of the surface of the absorber. These structures allow for deep sub-wavelength thicknesses of the cell without increased surface recombination due to non-planar morphology [25]. These advantages have been demonstrated in many experiments [26]–[36]. In addition to scattering, planar metallic surfaces can benefit photovoltaics by enabling new waveguide modes. Surface plasmon modes can have large propagation lengths and low group velocity but are also tightly confined to the surface of the metal. This phenomenon allows for very high absorption in very thin layers [23]. This is discussed further in section 2.3.

1.2.4. Dielectric nanostructures

One drawback of metallic structures is their high optical loss. This limitation can be overcome by using high index of refraction dielectric nanostructures. For this case many of the advantages of metallic structures are maintained: high fields in small volumes, sub-wavelength feature size (minimum cell thickness not significantly constrained) and scattering into wide angles. These dielectric structures also fall into two categories of either random

or periodic (though recent work has explored intermediate cases [37]–[40]). Absorption enhancements with random structures relies on scattering, index grading (discussed above), and/or resonant behavior in the structure itself [41]. The first two mechanisms have been discussed above, but structural resonance requires further attention. Here, energy is efficiently transmitted to these resonances, benefiting the cell when the electric field of the resonance overlaps with the absorber and/or when the structure preferentially couples to the absorber (as opposed to back to freespace). Structures such as nanowires [42]–[47], nanospheres (whispering gallery modes) [48]–[50], nanodomes [51] and nanocones [52], [53] have been used to demonstrate this effect for absorption enhancement (though some of these benefit additionally from periodic arrays or graded index effects). Periodic structures also rely on the above effects with the differences being that the resonances of the individual structures are coupled (though perhaps weakly). This too is a widely applied strategy [11], [40], [54]–[56] and will be discussed more in later sections. One drawback of these resonant structures, however, is the potential for angular selectivity. As with metallic structures, light can be confined on the nanoscale with careful design. The absorber can be surrounded with a higher index material to improve the absorption in the device by increasing the effective index of the waveguide, thereby reducing the group velocity. The slot waveguide (high-

low-high index) with the absorber in the center is of particular interest for this reason and because it also allows for a mode mostly confined to the low index center (TM mode only) [10].

1.3. Considerations for diffuse/indirect illumination

Often a solar cell will be illuminated partially or completely with diffuse rather than direct light due to scattering from the atmosphere, cloud cover or other objects in the environment. Similarly, unless sun tracking is incorporated, the light will impinge on the device over a full range of angles. This fact requires some special consideration for light trapping. As noted above, many of these light trapping strategies have angle dependence which degrades their performance when illuminated at all but a small subset of angle. Note that an ideal scatterer, which couples equally to and from all modes (by reciprocity, in and out coupling must be equal), has no angle dependence (see Chapter 2 for in depth discussion). Non-ideal scatterers sacrifice angular independence for resonant absorption. They, however, also benefit from the fact that scattering out of the cell can only take a limited number of paths, which reduces the total energy leaving the absorbing system. Thus, whether a given light trapping strategy performs better or worse than the ideal scatterer depends on the overlap of illumination profile and coupling profile of the device [11]. This situation implies that completely diffuse illumination will always be best absorbed by using an ideal scatterer. Note that over the course of a year the sun does not sweep through all possible angles which implies that a non-ideal scatterer may still outperform an perfect one on average.

1.4. Outline of this thesis

This thesis focuses on measurement, modeling, and applications of light trapping in solar cells. An overview of the following chapters is given here:

- Chapter 2 reviews limits of light trapping. This chapter gives an overview of the traditional light trapping limit and its assumptions. We then review more recent work that explores design spaces, which break these assumptions, and discuss how doing so offers the potential for exceeding this traditional limit. This chapter is based in part on the material in J. Murray & J. N. Munday. "Light trapping principles and limits for photovoltaics." *Submitted* (2016) and Y. Xu, J. Murray & J. N. Munday in *Quantum Dot Solar Cells* 349–382 (Springer New York, 2014).
- Chapter 3 describes the equipment developed for the work presented in this thesis. Details of the equipment design, construction, and operation are given.
- Chapter 4 focuses on our work measuring and modeling internal scattering intensity distributions. In this chapter we discuss our measurement technique, which enabled the development of the index ensemble model. We show how this model describes dielectric scattering layers physically, and we demonstrate the effectiveness of the model in predicting absorption. Chapter 4 is based on the published

work described in J. Murray & J. N. Munday. "Experimental demonstration and modeling of the internal light scattering profile within solar cells due to random dielectric scatterers." *J. Appl. Phys.* 119, 023104 (2016).

- Chapter 5 explores an extension of the index ensemble model to calculate absorption in individual layers of arbitrary stratified planar media (having any combination of thin coherent films and thick incoherent slabs) containing randomizing scattering structures. We explore several applications of this extended theory and compare it to experiment. This chapter is based in part on the manuscript J. Murray & J. N. Munday "A generalized approach to modeling absorption and photocurrent in solar cells with light scattering structures." *Submitted* (2016).
- Chapter 6 describes a solar cell smart window with switchable light trapping using polymer dispersed liquid crystals. In this chapter, we use the previously described experiments and models to evaluate the performance of this device. We are able to show that this smart window has the potential to self-power. Chapter 6 is derived in part from the work given in J. Murray & J. N. Munday. "Electrically controllable light trapping for self-powered switchable solar windows." *Submitted* (2016).

- Chapter 7 offers concluding remarks and potential extensions of the work described in this thesis.

Chapter 2: Light trapping limits

In order to improve the optical absorption in thin-film materials, light trapping techniques are needed. Understanding the limits of light trapping allows researchers to evaluate the objective effectiveness of their designs and to focus on the fundamental issues involved. In this chapter, we review the traditional light trapping limit and discuss methods for surpassing it using nanophotonic design principles.

2.1. Introduction to light trapping

Yablonovich's 1982 derivation [9] of the ergodic limit for light trapping serves as a benchmark for the calculation of absorption limits in materials and as a reference point for measured absorption in solar cells. The result shows that, for optically thick materials, and in the limit of diminishing absorption, the path length enhancement is bounded by $4n^2$, where n is the refractive index of the material (note: the enhancement can more generally be written as $4n^2/\sin^2(\theta)$, where θ is the emission angle into the material surrounding the cell and is usually taken to be $\pi/2$, resulting in simply $4n^2$) [57]. Part of the appeal of this approach is its simplicity; however, this simplicity results in a limited range of applicability. In fact, the new generation of ultra-thin and/or nanostructured solar cells cannot be treated with this formalism. Here we

review the fundamental limits of light trapping. We present a cohesive picture of the traditional $4n^2$ limit, the various proposed limits and terms used to describe these. We then review how, based on the more recently proposed limits, the traditional limit may be exceeded. Section 2.2 reviews the traditional limit and characterizes other limit calculations based on which assumptions of the traditional limit they adhere to. Section 2.3 covers these more recent limit calculations. Section 2.4 explores how, by considering these calculations, the traditional limit can be overcome.

2.2. The $4n^2$ limit

In this section, we will review the assumptions of the original calculations for the absorption limit in order to make a distinction between several terms that are sometimes used interchangeably: the ergodic limit, the ray optics limit, the $4n^2$ limit, and the Yablonovitch limit. As these terms often refer to Yablonovitch's original work, we first consider the assumptions of that formalism [9], [58]. These terms will be defined by their inclusion or exclusion of these assumptions.

2.2.1. Assumption 1: ergodicity

We first assume that as light enters a slab, it is fully randomized (defined here as having all modes or optical states equally filled or occupied) before

significant absorption occurs. It is usually posited that the light is randomized via surface texturing. Such a surface displays uniform, isotropic reflectance inside the slab and is referred to as Lambertian. While it is difficult in practice to obtain an ideal Lambertian scatterer, many roughened surfaces will randomize the light to a high degree after only a few reflections. In the most general sense, we will refer to the ergodic limit as the light trapping limit for fully randomized light, which contains no further assumptions. The ergodic limit is thus a broadly applicable limit whose explicit mathematical form requires additional information or assumptions about the system under consideration.

2.2.3. Assumption 2: thick slab

Next, we assume that the slab is thick compared to the wavelength of the light so that the slab can support a near continuum of modes and that ray optics may be employed. The ray optics limit is thus determined by ray tracing and enables the inclusion of absorption. While it is not necessary to employ assumption 1 in the ray optics limit, the general case can be computationally intensive to calculate, and approximate analytical expressions are often used that consider both assumptions 1 and 2. For fully randomized light and for weak to moderate absorption, the ray optics limit can be written as [58]:

$$A = \frac{(1 - e^{-4\alpha h})T_{\text{in}}}{\left[1 - e^{-4\alpha h} \left(1 - \bar{T}_{\text{esc}}/n^2\right)\right]} \quad (2.1)$$

where T_{in} is the incident transmission, and \bar{T}_{esc} is the weighted transmission of light exiting from the slab through the escape cone (defined as $\bar{T}_{\text{esc}} = 2n^2 \int_0^{\sin^{-1}(1/n)} T_{\text{esc}}(\theta) \cos \theta \sin \theta d\theta$ and where θ is the angle from normal inside the slab and $T_{\text{esc}}(\theta)$ is the transmission out of the cell), α is the absorption coefficient, and h is the slab thickness. For an ideal antireflection coating, we can also make the approximation $\bar{T}_{\text{esc}} = T_{\text{in}} \approx 1$ to further simplify Eq 2.1.

2.2.4 Assumption 3: weak absorption

Finally, we assume that the absorption is sufficiently weak so that it may be considered as a perturbation. For small αh , the absorption is small, and $1 - e^{-4\alpha h} = 4\alpha h$. With this approximation, Eq. 2.1 becomes:

$$A = \frac{4n^2\alpha h T_{\text{in}}}{[4n^2\alpha h + \bar{T}_{\text{esc}}]} \quad (2.2)$$

The $4n^2$ limit is achieved with the additional approximation that $T_{\text{in}} = \bar{T}_{\text{esc}} = 1$. Thus, the $4n^2$ limit, which is also often called the Yablonovitch limit, is given by Eq (1.1).

2.2.5. Regimes of validity

It could be argued that the ergodic limit is the most general limit, which requires only that the light fully occupy all available modes upon scattering,

thus allowing the violation of assumptions 2 and 3. The ergodic limit is thus the limit of absorption when light is scattered in the slab in a random process but no other assumptions need be made. Despite its generality, there is some parameter space where even this assumption does not hold. This would include various resonant structures or ones with non-Lambertian scattering mechanisms. We note that this limit may always be exceeded over a small wavelength range when a resonant condition exists.

It should be noted that while the $4n^2$ limit approximation is not valid when the thickness of the material becomes small compared to the wavelength of the incident light, it is still generally used as a benchmark for comparing measured and calculated absorption in structures. Thus, the following discussion will maintain this benchmark even as the assumptions underpinning the formalism are broken. However, it is not immediately apparent how the relaxation of these assumptions might allow the $4n^2$ limit to be exceeded. The next two sections will investigate ways to calculate the limit of absorption in a general way, which is valid for thick and thin films.

2.3. Limiting Cases

In this section, we will address various limiting cases and how the assumptions that go into the derivation of the $4n^2$ limit can be broken to surpass this limit.

2.3.1. Waveguide approach

As the thickness of the absorbing structure decreases, so does the number of available guided modes until they can no longer be approximated as a continuum (breaking assumption 2 of the previous section). When this happens, the $4n^2$ limit is no longer appropriate to describe the absorption limit. To calculate the absorption in this case, each set of modes should be considered individually. The absorption can be described more generally by the waveguide limit [10], [59], [60]:

$$A = \frac{\rho_{\text{rad}}(\omega)}{\rho_{\text{tot}}(\omega)} A_{\text{rad}} + \sum_m \frac{\rho_m(\omega)}{\rho_{\text{tot}}(\omega)} A_m, \quad (2.3)$$

where

$$A_{\text{rad}} = \frac{\alpha}{\alpha + \left[4 \frac{\rho_{\text{tot}}(\omega) h v_{\text{g}}^{\text{rad}}}{\rho_{\text{inc}}(\omega) v_{\text{g}}^{\text{inc}}} \right]^{-1}} \quad (2.4)$$

and

$$A_m = \frac{\alpha\Gamma_m}{\alpha\Gamma_m + \left[4 \frac{\rho_{\text{tot}}(\omega)h v_g^m}{\rho_{\text{inc}}(\omega)v_g^{\text{inc}}}\right]^{-1}}, \quad (2.5)$$

m is the mode number, Γ_m is the modal confinement factor (fraction of total energy for the mode in the absorber), and v_g^x is the appropriate group velocity either for the radiation modes, v_g^{rad} , the incident modes, v_g^{inc} (typically a subset of the radiation modes), or the guided modes, v_g^m , corresponding to the absorption rate $\gamma_{\text{abs}}^m = \alpha v_g^m \Gamma_m$ (note: in general this rate must be computed as $\gamma_{\text{abs}}^m = \text{Im}(\beta_m)$ where β_m is the modal propagation constant [60]). Lastly, $\rho_x(\omega)$ is the density of each type of mode with angular frequency, ω , and $\rho_{\text{tot}}(\omega)$ is the sum of all modes. This calculation is derived by noting that the ratios of the density of states gives the fraction of light that enters each mode and A_{rad} and A_m give fraction of energy loss due to absorption. This formalism encompasses all guided modes including surface modes, which are not considered in the $4n^2$ limit.

When there are no surface modes and h becomes large, the $4n^2$ limit is recovered from the waveguide approach. Assuming the incident light comes from air/vacuum, $\rho_{\text{tot}}(\omega)$ approaches $n^3 \rho_{\text{inc}}(\omega)$, the bulk density of states. With no dispersion, v_g^m and v_g^{rad} also approach the bulk value of $\frac{c}{n}$. Lastly, the confinement factor approaches one. This behavior yields:

$$A_{\text{rad}} = A_m = \frac{4n^2\alpha h}{[4n^2\alpha h + 1]}, \quad (2.6)$$

and

$$A = A_{\text{rad}} \left[\frac{\rho_{\text{rad}}(\omega)}{\rho_{\text{tot}}(\omega)} + \sum_m \frac{\rho_m(\omega)}{\rho_{\text{tot}}(\omega)} \right] = \frac{4n^2\alpha h}{[4n^2\alpha h + 1]}. \quad (2.7)$$

2.3.2. The local density of optical states approach

The strength of the waveguide approach is that it is easy to understand the absorption process, and it draws on the vast literature on waveguides. However, when material losses become moderate so that modes can no longer be described by discrete k -vectors or when localized resonances are of interest, this approach becomes harder to implement. Calculating the absorption limit by considering the Local Density of Optical States (LDOS) resolves these issues and offers its own advantages for intuitive design of solar cells or detectors [61].

This approach considers the rate of emission at all points in a structure from a randomly oriented dipole and relates the dipole emission rate to light intensity, and thus the rate of absorption. This method exploits the fact that the absorption and emission rates are proportional to the LDOS by Fermi's golden rule. The absorption at each point may thus be increased above or reduced below the bulk value based on the local environment. Finally, the average

absorption enhancement of the structure is obtained from the averaged LDOS [61].

One simple way to change the LDOS is to allow the test dipole to evanescently couple to an adjacent structure with a higher (or lower) mode density. As an example, if a dipole is placed near the interface of a material with a higher index, the number of modes available is increased as evanescent coupling into modes outside the critical angle (modes which cannot be supported in the lower index material) is possible. Another option is to allow evanescent coupling into modes that would not even be available in a bulk, such as surface plasmon modes. The strength with which the dipole radiates (couples) into modes not available in the bulk will on average decrease with distance (deviation from this relationship can occur when the dipole interferes with its scattered field). Thus, for planar geometries the enhancement (or reduction) is minimal for optically thick structures but can be enormous (factors of 10s to 1,000s for a variety of simple geometries [61]–[63]) as the thickness of the absorber decreases to the order of 10-100 nm.

Structures may be qualitatively compared using the above considerations; however, exact calculations of the LDOS require care as the structures become small, conducting, or lossy. Calculations for planar geometries were presented in the 1970's [64]–[66]; although, non-local effects

can dominate in the regions of most interest, *e.g.* very near interfaces, complicating these calculations. For brevity these calculations will not be presented here; however, Ford and Weber [24] offer an often cited primer, and Tomáš [62], [67] has extended these calculations to absorbing materials. For complex geometries, such as photonic crystals or nano-structures, numerical simulation must, in general, be used. Once the LDOS is determined, the absorption enhancement (or reduction) when all modes are filled can be calculated as [61]:

$$\frac{\langle \rho(\omega, r) \rangle}{\rho_{\text{bulk}}(\omega)} = \frac{\langle \rho(\omega, r) \rangle}{n^3 \omega^2 / \pi^2 c^3}, \quad (2.8)$$

where $\langle \rho(\omega, r) \rangle$ is the spatial average of the LDOS. This ratio reduces to unity in a bulk where $\langle \rho(\omega, r) \rangle = \rho(\omega)_{\text{bulk}}$.

2.3.3. Rigorous coupled-mode theory approach

Both of the above approaches represent upper limits to absorption assuming perfect coupling to all modes. However, by reciprocity in-coupling into a mode and out-coupling out of the mode must be proportional. So there can be some benefit to limiting the available modes of the structure. Moreover, ideal coupling is not a trivial matter. For this reason, it might be appropriate to consider relaxing the assumption of ergodicity to allow for higher absorption and to find more accurate solutions. In doing so, Coupled-mode

Theory has been employed to investigate the limit of absorption when non-ideal coupling is considered. As will be shown below, these results agree with the above approaches and shed light on what is meant by ideal coupling. Ultimately, the waveguide and LDOS approaches represent solutions to the ergodic limit of the coupled-mode theory. However, relaxing the assumption of ergodicity may also allow for improvements beyond those limits.

The basic approach is to consider the rate of energy gained and lost from each mode by inter-mode coupling or absorption, then balancing these to solve for the steady state absorption. While situations with simple gratings can be easily calculated analytically, these structures by their nature result in strong narrow band resonant behavior. However, photovoltaic applications require broadband coupling and absorption. To achieve this behavior, a large number of broad bandwidth resonances are needed, which requires more complex gratings or structures. These complex situations are generally simulated rather than calculated exactly. The limiting cases, however, are amenable to analytic forms and provide useful insight into what is required for solar applications.

The steady state absorption of a mode is given by [54]:

$$A(\omega) = \frac{\gamma_{\text{abs}}^m \gamma_e}{(\omega - \omega_0)^2 + (\gamma_{\text{abs}}^m + N\gamma_e)^2}, \quad (2.9)$$

where N is the number radiation modes, which can be coupled to (from), and γ_e is the in- or out-coupling rate into (out of) the mode and ω_0 is the angular frequency of the mode. A more convenient form for considering the limiting case is to describe the resonance in terms of the spectral cross section:

$$\sigma(\omega) = \int A_m(\omega) d\omega = 2\pi\gamma_{\text{abs}}^m \frac{1}{N + \gamma_{\text{abs}}^m/\gamma_e}. \quad (2.10)$$

When the input spectrum, $\Delta\omega$, is broad compared to the cross section as is typically the case for solar applications and when the cross section is maximized by operating in the over-coupling regime (*i.e.* $\gamma_{\text{abs}}^m \ll \gamma_e$):

$$A = \sum_m 2\pi\gamma_{\text{abs}}^m / N\Delta\omega = \frac{2\pi\gamma_{\text{abs}}^m M}{\Delta\omega N}, \quad (2.11)$$

where M is the number of modes per unit frequency. This can be connected to the Yablonovich limit by considering a thick slab. In which case:

$$A = \frac{2\pi\gamma_{\text{abs}}^m}{\Delta\omega} \frac{h}{2\pi} \frac{\rho_{\text{tot}}(\omega)}{\rho_{\text{inc}}(\omega)} \left(\frac{4\Delta\omega}{c} \right) = 4n^2 h\alpha. \quad (2.12)$$

Here M has been replaced by the bulk material density of states times the bandwidth and N has been replaced by the free space density of states divided by the thickness of the slab over 2π as the number of radiation modes that can couple into the slab is given by the number of modes with appropriate parallel k -vector ($<\omega/c$). Finally γ_{abs}^m has been replaced by the absorption coefficient times the group velocity in the bulk material and the confinement factor (set to

unity). It should be noted that Eq. 2.12 is different from the more precise version of the Yablonovich limit given in Eq. 1.1. This results from the simplifying assumption of over-coupling. It is also useful to see that this formalism agrees with the LDOS and waveguide approaches as it must, given that all of them represent solutions to Maxwell's equations only with different ranges of applicability. Eq. 2.12 shows that, in the limit of over-coupling regime, the absorption is proportional to the normalized LDOS, $\rho_{\text{tot}}(\omega)/\rho_{\text{inc}}(\omega)$. Eq. 2.4, 2.5, and 2.12 all give rise to the same absorption enhancement factor assuming (as above) that bulk parameters can be used throughout and total absorption is small. Finally, it should be noted that Eq. 2.12 applies to the case of equal coupling from all incident radiation modes. It is possible to produce grating structures or photonic crystals that couple only to or from a small subset of modes, which further enhances the absorption by reducing N .

2.4. Exceeding the $4n^2$ limit

In this section, we calculate light trapping for specific structures that can surpass the $4n^2$ limit. We discuss alternative approaches to this calculation using the methods discussed above and the various advantages of each method.

2.4.1. Waveguide approach

To surpass the $4n^2$ limit, we must consider a system that violates one of the assumptions discussed in section 2.2. We begin by considering a thin slab, which violates assumption 2. While the absorption in a thin slab cannot be accurately determined using the ray optics limit or the $4n^2$ limit, it can be treated using the waveguide approach [7,8], the LDOS approach [61], or an approach based on a statistical temporal coupled-mode theory formalism [54]. As the slab gets thinner, the density of guided modes becomes the dominant contribution with the limiting case being one mode for a very thin waveguide. For this case, Eqs (3-5) reduce to:

$$A \approx A_m = \frac{\alpha\Gamma_m}{\alpha\Gamma_m + \left[4 \frac{\rho_{\text{tot}}(\omega)h\nu_g^{\text{rad}}}{\rho_{\text{inc}}(\omega)\nu_g^{\text{inc}}}\right]^{-1}} = \frac{\alpha\Gamma_m}{\alpha\Gamma_m + \left[4 \frac{\beta_m\pi c^3}{2\omega^2 h\nu_g^m n}\right]^{-1}}, \quad (2.13)$$

where the surrounding material is taken as vacuum. By comparing this expression to Eq (1.1), it is evident that the $4n^2$ limit will be exceeded when the following condition is met [10]:

$$\frac{\beta_m\nu_g^{\text{rad}}}{k_0\nu_g^m}\Gamma_m > 4n\frac{h}{\lambda}. \quad (2.14)$$

Using the above equation, the ideal mode would be highly confined, have small group velocity, large propagation constant, and exist in a thin waveguide. Figure 2.1 shows the dispersion relation for various types of

modes. Most photonic modes will not exceed the $4n^2$ limit due to low confinement in thin films and the fundamentally smaller propagation constant, as shown by Stuart and Hall [59]. However, it can be seen that sets of modes exist that can surpass the $4n^2$ limit. For example, surface modes most clearly meet the condition of high confinement in a thin slab. Surface plasmon polariton (SPP) modes by their nature have large propagation constants and low group velocity [68]. Another set of mode is the slot waveguide modes defined by high-low-high index structures, where the mode may propagate at the lower velocity and larger propagation constant defined by the high index material.

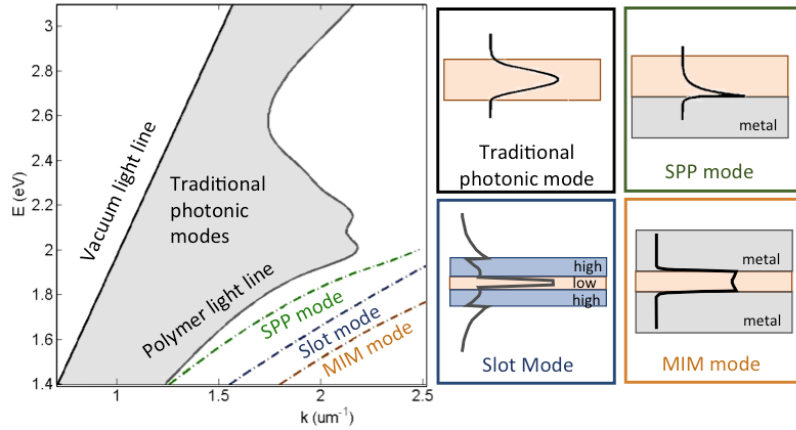


Figure 2.1: Dispersion diagram for modes available to P3HT:PCBM structures as an illustrative example for finding modes that may exceed the $4n^2$ limit. Modes that exist between the vacuum light line and the polymer light line correspond to traditional photonic modes. Modes that may lead to absorption enhancements in excess of the $4n^2$ limit are also shown (dashed lines): surface plasmon polariton (SPP) mode (green), high-low-high index (slot) waveguide mode (blue), and metal-insulator-metal (MIM) mode (orange). Right: schematic representation of various modes.

2.4.2. LDOS approach

Structures that surpass the $4n^2$ limit based on the waveguide approach also surpass the limit based on the LDOS approach. Both the waveguide approach and the LDOS approach are two equivalent ways of describing the absorption as both represent solutions to Maxwell's equations giving the \vec{E} -field at every point in the structure. The LDOS approach is more broadly applicable than the waveguide approach, because it can also be used for more complex structures; however, different approaches may be used depending on

which one gives the best physical insight into the problem. From the LDOS approach, the use of a metal or high index cladding layer introduces new molecular decay (or absorption) channels that would otherwise be unavailable to the bare slab. Further, as discussed above, the absorbing material should be thin so that most of the molecules of the slab can easily radiate into the new modes presented by the cladding layers.

The absorption in a 50 nm film of P3HT:PCBM on silver is shown in Fig. 2.2 for the $4n^2$ limit, the waveguide limit, and the LDOS limit. In both the waveguide and LDOS formalisms, large fields exist near the metal-polymer interface as determined by the mode profile of the fundamental TM mode (Fig. 2.2b) and the LDOS profile (Fig. 2.2c). These profiles demonstrate the predicted strong absorption enhancement. There is agreement between the waveguide and LDOS calculations with only a small deviation due to an under estimation of absorption from low Q modes at shorter wavelengths (using the waveguide calculation) and a slight reduction in LDOS due to boundary calculation effects (*i.e.* <5 nm nearest the boundaries were neglected for simplification of the calculation).

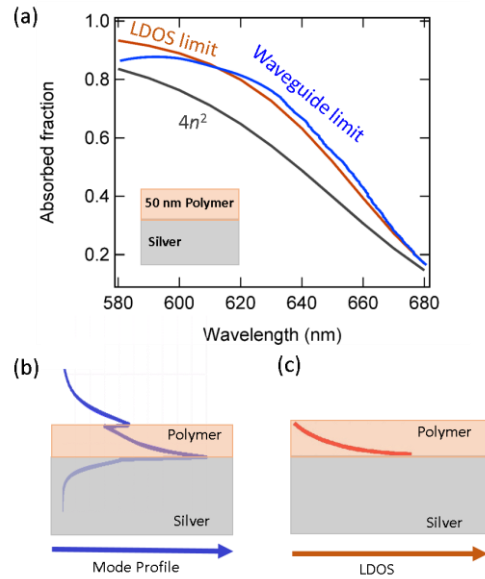


Figure 2.2: Comparing limits of absorption in a polymer/metal waveguide. In a thin film, both the waveguide limit and the LDOS limit predict absorption enhancements in excess of the $4n^2$ limit. (a) Comparison of absorption limits for a 50 nm thick slab of P3HT:PCBM on silver show similar results for both the waveguide and the LDOS method. Schematic (based on calculations) of (b) the mode profile and (c) the LDOS for the polymer on silver structure.

2.4.3. Rigorous coupled-mode approach

The calculations for the waveguide and LDOS approaches assume that perfect in- and out-coupling are achieved to and from all modes (maintaining assumption 1). This neglects the reality of non-ideal coupling and eliminates an additional degree of freedom which could potentially further enhance absorption. Grating structures can be incorporated into the waveguides discussed above but can also break assumption 1 which results in resonant scattering structures (limited bandwidth and increased angle dependence)

[11]. However, it is possible to exploit the angular dependence. From Eq. 2.11 it can be seen that reducing the number of modes that can couple into (out of) the system, N , the absorption may be enhanced. This can be achieved by reducing the grating lattice size or periodicity, L . The system can only scatter into freespace modes that have a k -vector greater than to that of the grating and meet the phase matching condition:

$$k_{\parallel} = 2\pi m/L, \quad (2.15)$$

where m is an integer. A trade off however exists, as the number of modes in the absorber to which the structure may couple, assuming a bulk structure, is given by:

$$M = \frac{8\pi n^3 \omega^2}{c^3} \left(\frac{L}{2\pi}\right)^2 \left(\frac{h}{2\pi}\right) \Delta\omega. \quad (2.16)$$

Thus a larger lattice size implies a larger number of absorber modes but also a larger number of available outgoing modes (increasing the out coupling). However, the number of outgoing freespace modes changes in discrete steps while M increases monotonically. In fact, for a structure that may only couple to normal incidence, a bulk structure can absorb $4n^2\pi$ times as much as a single pass but the absorption only exceeds the $4n^2$ limit over a limited spectral range (see Ref [11]). For larger lattices, this approaches $4n^2$ as a Lambertian scatterer implies an infinite lattice constant. Non-bulk structures where M is small may also benefit from this principle but the relationship will be determined by the

factors discussed above. Regardless, all of the approaches (Waveguide, LDOS, and Statistical Coupling Mode) agree with a sufficiently large lattice size [69].

2.4.4. Non-random scattering

Much of the preceding discussion has been concerned with fully randomized light such that all of the modes are equally populated. However, producing truly Lambertian scattering can be difficult and may, as discussed with in section 2.4.3, be counter-productive. The potential effect of non-random scattering can be demonstrated by considering a structure that couples light from an incident radiation mode into many guided modes. It would seem that reciprocity would demand that coupling out of these modes would occur just as strongly as the in-coupling, and nothing would be gained. However, this observation ignores the loss incurred between coupling into and coupling out of the guided mode, as well as energy exchange between the modes themselves.

When light is not fully randomized there are opportunities to exceed the $4n^2$ limit. Consideration of non-Lambertian scattering actually precedes calculations of the ergodic limit [70]. Practical geometries that might exceed the ergodic limit have been investigated by Green [71] who proposed that 1D pyramidal gratings can enhance absorption beyond that of a randomizing

texture for top and bottom gratings that run perpendicularly to each other. The absorption enhancement works on the principle described above where the first few scattering events direct light preferentially outside of the escape cone. The light distribution eventually becomes approximately randomized, but the first few round trips, which are critical, lose less light through the escape cone than would be lost by a Lambertian scatterer. This concept was further explored in a more general way by Rau *et al.* [72].

Another scheme which might fall under this category is angle restrictive filters. The role of angular restrictive filters in light trapping is to reduce the number of freespace modes that can propagate away from the solar cell. As mentioned above, angle restriction can be incorporated into the $4n^2$ limit, assuming the light is fully randomized in the cell, by changing it to $4n^2/\sin^2(\theta)$, where θ is the emission angle from the cell ($\theta = \frac{\pi}{2}$ for a regular, planar cell). This can lead to very high absorption with the maximum enhancement occurring when the emission angle matches the divergence angle of the illumination source. For direct illumination from the sun this angle is 0.267 degrees, resulting in an additional path length enhancement factor 46,000. This type of structure has the additional advantage of increasing intrinsic cell performance [73], [74].

In recent years there has also been great interest in periodic nanostructures for scattering, which create non-Lambertian scattering distributions. While ultimately, these structures can be described under rigorous coupled mode theory, some specific discussion is appropriate. Demonstration of absorption beyond the $4n^2$ limit using a 2D grating has been shown by simulation but with high incident angle selectivity [11]. This enhancement has also been shown using other photonic structures but only for a select range of wavelengths [75], [76]. Structures can be designed to efficiently couple into beneficial modes [55], [77]–[79], and psuedo-random structures have been designed based on considerations of spatial correlation [80] and by optimization of a Gaussian distribution of sphere sizes [81]. Similarly, disordered photonic crystals have also been used [38], [39]. However, for these structures the effect of scattering is wavelength dependent and the absorption enhancement is similarly limited. Plasmonic scattering structures have also been compared favorably to Lambertian scattering structures but with their own advantages and disadvantages [31]. Figure 2.3 shows examples of different scattering architectures including both ergodic and non-ergodic types. Lambertian texturing guarantees equal occupation of all possible modes and yields the ergodic limit (Fig. 2.3a), while non-Lambertian (Fig. 2.3b) and scattering couplers (Fig. 2.3c) can provide new

opportunities by violating one of the assumptions (complete light randomization) of Yablonovitch's original derivation.

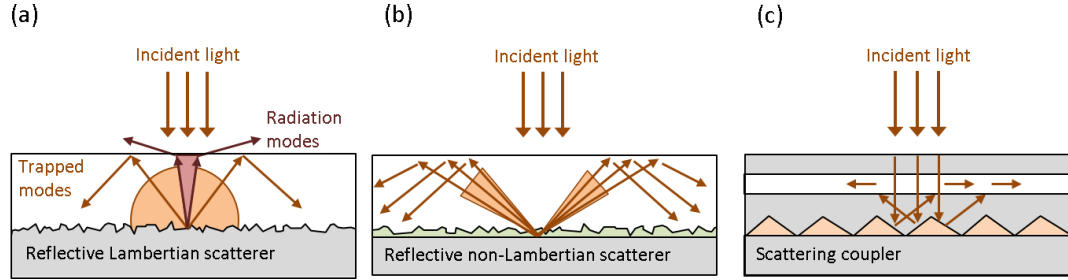


Figure 2.3: Surpassing the ergodic limit through non-Lambertian scattering. (a) Lambertian scatterer creating absorption at the ergodic limit. (b) Example of a beneficial non-Lambertian scatterer. Because less light escapes through the escape cone this structure can result in absorption beyond the ergodic limit even if light eventually becomes fully randomized. (c) Scattering coupler designed to couple incident light directly into desirable modes. Coupling out of this mode also occurs but significant absorption may take place between such events.

2.4. Conclusions

In this chapter we have shown both the need and necessary conditions for exceeding the $4n^2$ limit. In order to surpass this limit, at least one of the assumptions of its derivation must be broken, *e.g.* the use of non-randomizing scattering structures, the use of thin-films or nanoscale structures, or the use of highly absorptive materials. Structures that provide enhanced LDOS and/or non-random scattering are found to exceed the $4n^2$ limit when appropriately

designed, making possible new architectures for ultra-thin photodetectors and solar cells.

Chapter 3: Instrumentation

This chapter discusses the development of two experimental setups, which enabled much of the work that is discussed in later sections of this dissertation, as well as several other projects [82]–[88]. The first system is a multipurpose tool for characterizing material absorption, transmission, and reflection as well as solar cell quantum efficiency and will be referred to as the Multipurpose Spectroscopy Station (MSS). This setup enabled absorption and transmission measurements for validation of the models discussed in Chapters 4 and 5 and for the characterization of the switchable solar cell described in Chapter 6. The external quantum efficiency (EQE) and transmission measurements are also used in several other projects discussed under *Applications* later in this chapter. The second system is designed for measurement of angularly resolved optical scattering and will be referred to as the Scattering Distribution Station (SDS). This setup enabled the creation of the internal scattering distribution measurement described in Chapter 4, which is necessary for the materials characterization described in Chapters 5 and 6. In addition to these setups, the experiments in Chapter 6 required an apparatus for creating a high voltage (>100 V) square wave, referred to as the high voltage square wave drive. The rest of this chapter fully describes the equipment for each experimental setup and their uses.

3.1. Multipurpose Spectroscopy Station overview

As a broad overview, the MSS consists of a white light source that is steered along three possible light paths leading to one of two integrating sphere ports or to the EQE stage. At the end of each path, the light intensity is converted to current by either a photodiode or a photovoltaic device (current is used here because it is proportional to light intensity, to a very good approximation). The current is measured by a lock-in amplifier which digitizes the signal and improves the signal-to-noise ratio. The data is then sent to a computer that also controls the other mechanical processes of the MSS. Figure 3.1 (a),(b) shows an overview of the entire system and interactions between each of its parts. The entire system is mounted on a portion of a large optical table. The major components of the MSS can be broken into four subsystems: the monochromatic light source and conditioning optics, the integrating sphere and EQE stage, signal processing and driving electronics, and the LabVIEW front end. These subsystems will each be explored in detail below.

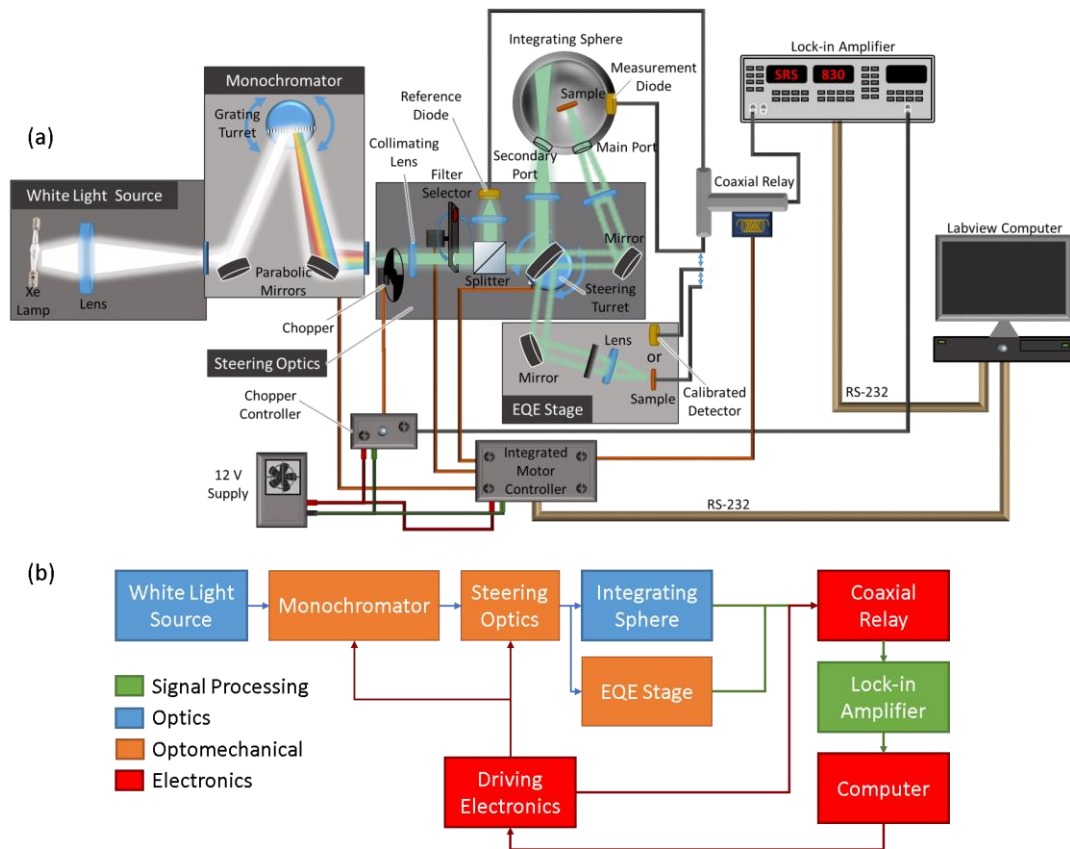


Figure 3.1: Overview of MSS. (a) Schematic overview of the Multipurpose Spectroscopy Station. (b) Block diagram of MSS showing major components and connections.

3.1.1. Monochromatic light source and beam conditioning optics

Monochromatic light is produced and steered by a set of optical and optomechanical components. The light originates from a white light source, ozone free 150 W Xenon Arc lamp (6255, Newport Corp.). The explosion proof lamp housing is an Oriel 66902 that contains the arc lamp itself, cooling fans, and lamp start-up electronics. The housing is controlled by an Oriel 69907

regulated power supply that stabilizes and monitors power to the lamp housing.

The light from the Xe lamp is coupled into a half-meter monochromator (SPEX 500M). The connection between the lamp housing and the 500M is enclosed by a custom tube to prevent UV exposure to the users but to allow future access to the white light sources. The monochromator has an aperture of $f/4$, which is matched by a 1.5" aspheric fused silica lens at the input (fused silica used here for its UV transmission; other components are BK7 glass) and a 1" BK7 lens at the output. The 500M is driven by a custom integrated motor controller.

The monochromatic source required adjustment before incorporation into the setup to maximize its functionality. This monochromator has a dispersion of 1.6 nm per mm of slit width and a set point resolution of 0.005 nm. For all the experiments described here we use a slit width of 3 mm for high throughput, resulting in a bandwidth of 4.8 nm. A single point calibration of the device was performed by comparing the output of the monochromator to a HeNe laser (Thorlabs HNL050L). Both light sources are fed into a fiber-coupled spectrometer (Thorlabs CCS100), and the monochromator was adjusted so that the peaks of the two spectra coincided. The set point is

manually read from a 5-digit mechanical counter on the face of the 500M. To adjust the calibration, a setscrew on the dial of the monochromator was loosened and the dial was set to the HeNe wavelength, 632.8 nm. The feet of the 500M were removed so that the monochromator was parallel with the optical table (note that all other optics were aligned to this device). The lamp housing and output optics were then aligned to the 500M by adjusting the mounting posts, and the lamp housing mirror was adjusted for maximum optical throughput.

Figure 3.2 shows the beam conditioning optics of the MSS subsystem. As the light leaves the lamp housing, it passes through various components including: an optical chopper, filters, beam-splitter and reference detector, and mirror turn-table. The optical chopper creates a binary modulation of the light to produce a narrowband signal of known frequency for later signal processing by the lock-in amplifier (discussed below). The filter selection motor rotates filters in or out of the optical path to block second order diffraction from the monochromator at longer wavelengths. In the current configuration, only one filter is used, a longpass filter with a cutoff at 610 nm. Due to the Xe lamp and the optical materials used in the rest of the setup, essentially no light below 350 nm is transmitted, so the second order diffraction from the monochromator (which would be produced at 700 nm) is fully filtered. However the MSS is

also limited to ~1100 nm at long wavelengths due to the use of silicon photodetectors so second order diffraction from 610 nm light (which would be produced at 1220 nm) isn't a concern. This filter selector is followed by a glass beam-splitter which diverts ~10% of the light to the reference detector. This light is focused, the intensity is reduced by a factor of 2 using neutral a density filter, and the intensity is measured by a silicon photodiode (Thorlabs FDS100). This detector allows for normalization of the optical power to eliminate the effect of lamp output power drift with time. The photodiode is mounted in a custom aluminum enclosure with wire leads soldered to a panel mount BNC connector. The enclosure helps to isolate the diode from electromagnetic interference (EMI). The enclosure itself is mounted on a plastic post to avoid electrical connection to the optics table, which could otherwise provide overwhelming noise to the lock-in amplifier. The remaining ~90% of the light that passes through the beam-splitter is reflected along one of three paths determined by the mirror turn-table. The device is a set of two mirrors placed back to back and mounted on a motor driven turntable. The light is directed either through the sample port (or "main port") of the 6" integrating sphere (Labsphere RTC-060-SF) where a lens focuses the light at the center of the sphere, through the diffuse illumination port (or "secondary port") of the integrating sphere where a lens focuses it through a small opening into the

sphere, or the light is directed to the EQE stage. Two ports are used with the integrating sphere to account for secondary diffuse illumination (full measurement details are discussed below).

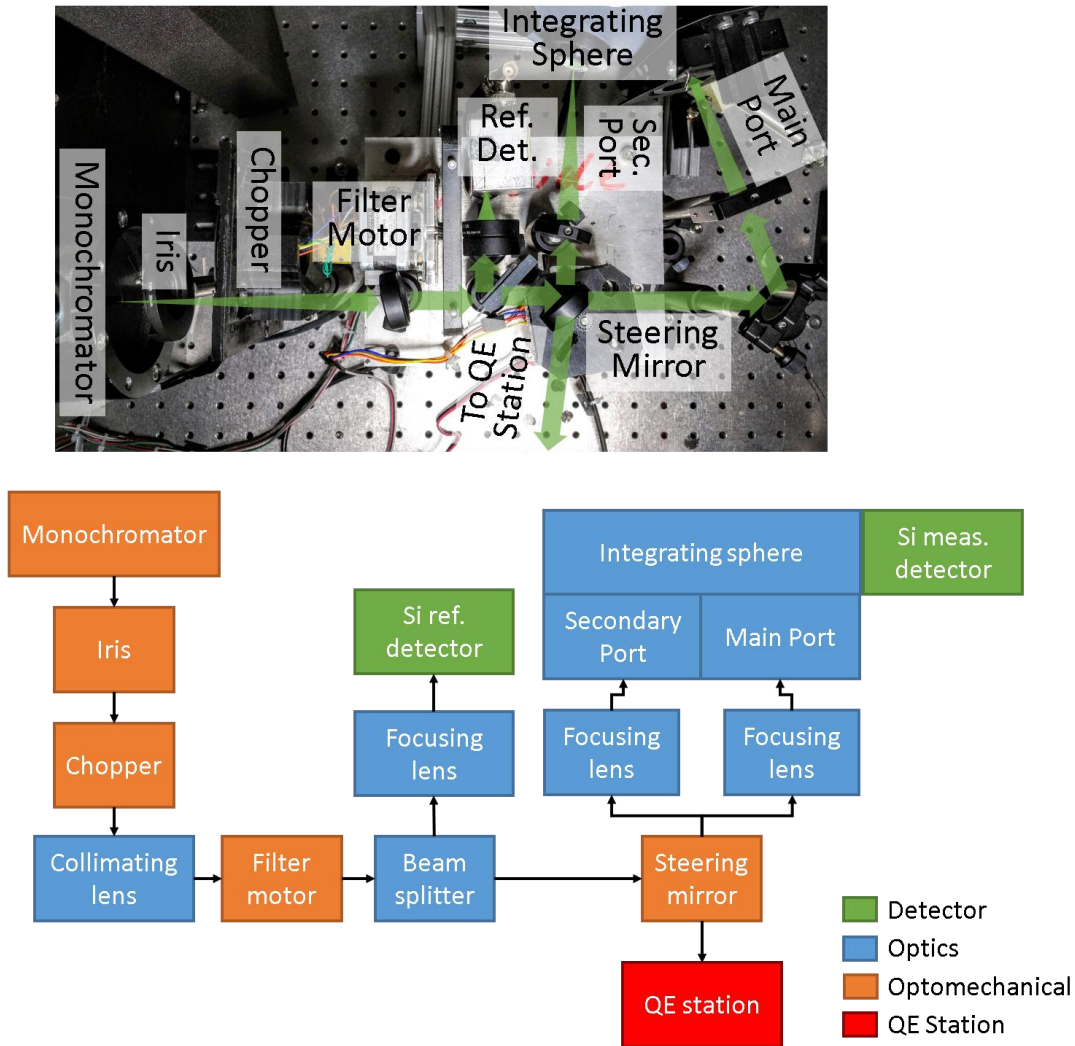


Figure 3.2: Overview of MSS optics. (a) Optical image of the Multipurpose Spectroscopy Station subsystems showing the beam conditioning optics with an overlay of light paths. Tapering of these paths represent focusing or defocusing of the beam. The splitting at the steering mirror shows possible beam paths (the image shows the system set to direct light through the secondary port of the integrating sphere). (b) Schematic view of the same.

The optical chopper is a custom built device but is based on an original commercial system. The main improvement to the commercial system is the use of a brushless driving motor which greatly reduces EMI and ultimately lowers the system noise floor by a factor of ~50. The driving circuitry in the motor also improved the frequency stability compared to the commercial system by a factor of ~10. The chopper is driven by a set of custom electronics that set the frequency, which is monitored using the lock-in amplifier (electronics discussed below). The optical chopper also includes a shield to prevent stray light from being chopped.

The filter selector and mirror turn-table are also custom built. They are both rotated by stepper motors that are in turn driven by the same custom integrated motor controller as the SPEX 500M. The stepper motors are driven by open loop control. However, each device has a stationary Hall Effect switch mounted on the frame and a small (1/4") neodymium magnet attached to the rotating peice. The zero position of the rotation is found by stepping the magnet past the sensor. This process is discussed in greater detail below.

3.1.2. Integrating sphere and EQE stage

The integrating sphere has several features for measuring optical properties. The main port is equipped with a sample clip at the entrance to the sphere, which allows for transmission measurements. A rotatable center post extends from the top of the sphere to mount samples. Figure 3.3b shows an image of this top. The rotation of the center post was originally read by a dial on the top of the sphere. However, the 1° graduations only allowed for a precision of about a degree and the accuracy can vary if the light path leading to the sphere is adjusted. To overcome these limitations a custom readout was added. A large gear is mounted to a cap, which fits over the original rotation knob and smaller mating gear (3:1 gear ratio) is attached to 10 k Ω , 10 turn potentiometer which is held in place by a fixture that replaced the original dial retaining ring. In addition, a stepper motor is attached to the fixture to allow for automated angle dependence measurements. This new angle readout allows for a precision of 0.012° (based on the typical digital multi-meter used) but with accuracy limited to $\sim 0.1^\circ$ based on setup procedures. Samples are mounted to this center post either with a clip for absorption measurements (or reflection measurements for samples with negligible transmission) or with a clamp holding samples in front of an absorbing black disk for reflection measurements. However, this black disk is found to have a reflectivity of 3%

rather than the ideal 0%. This non-ideality causes an error, ΔR , of approximately $0.03 * T_{\text{sample}}^2 / (1 - 0.03 * R_{\text{sample}})$, where T_{sample} and R_{sample} are the transmission and reflection of the sample respectively. This error can be very small for strongly reflective materials (ΔR of 0.1% for 90% reflective sample), but quite large for highly transparent samples (ΔR approaches 3% as T_{sample} goes to 100%). Our target for precision and accuracy in measurements is generally $<0.5\%$. As a result, reflection measurements are not used in this work and in general reflection measurements should be eschewed in favor of a combination of absorption and transmission measurements, both of which can achieve an accuracy of $\sim 0.1\%$. Regardless of the type of measurement, the intensity of light inside the integrating sphere is monitored with a photodiode (again, Thorlabs FDS100). This photodiode, which is mounted at the bottom of the sphere, is enclosed in the same manner as the normalization photodiode to reduce noise. The integrating sphere also incorporates several baffles, which prevent direct illumination of the photodiode; these baffles allow the light sufficient reflections inside the sphere for the complete optical randomization necessary for measurements with an integrating sphere. Figure 3.3b shows an inside cutaway of the integrating sphere.

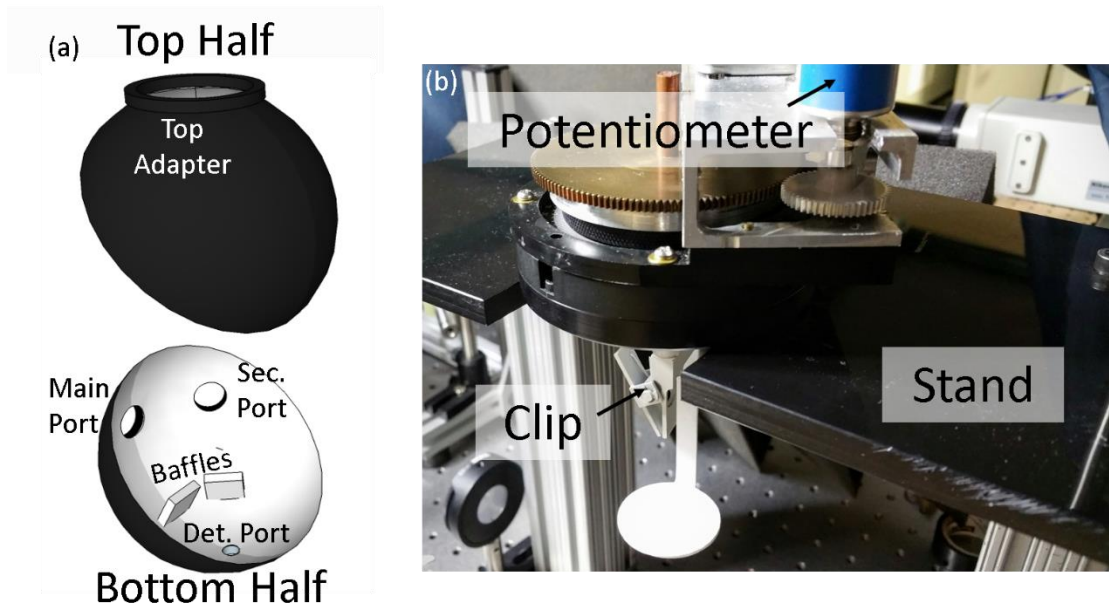


Figure 3.3: Integrating sphere parts. (a) Inside cutaway of the integrating sphere. (b) Image of the top of the integrating sphere sitting on the lid stand. The clip holds the sample in the center of the sphere for absorption measurements and the potentiometer allows for accurate determination of angle.

The EQE stage is composed of directing mirrors, focal lenses and movable platforms for illumination of either a calibrated detector or a sample. The calibrated detector (Thorlabs FDS100-CAL) is used to calculate the power arriving at the stage, which is necessary for determining EQE. This detector is also mounted in the same manner as the reference detector, in an aluminum enclosure and isolated from the optical table. The stage is equipped with two iron plated stands to mount micro-positioning probes for electrical connections to solar cells and other photovoltaic devices. In practice, connections are also

commonly made using silver epoxy to avoid contacting issues. The focusing lens is mounted in a threaded lens holder, which allows neutral density filters to be added. The neutral density filters can be used to ensure that the photo-generated current never exceeds the maximum current measurable by the lock-in amplifier. Finally, while the lock-in amplifier and the chopper create very good broadband noise rejection, samples with large photoactive areas (larger than approximately 1 in²) can absorb much more light from the room than from the EQE stage illumination. In such cases, the lock-in input can be saturated, and the signal is unreadable. To overcome this problem, a movable enclosure can be used to block ambient room light. Note that this is never a concern in the integrating sphere as it has only two small openings; as a result the total noise in integrating sphere measurements is dominated by electrical noise.

3.1.3. MSS Signal processing and driving electronics

In the Multipurpose Spectroscopy Station, the current signal going into the lock-in amplifier can come from one of two origins: the reference detector or the measurement detectors, because connections to the integrating sphere detector and EQE stage device connections are manually swapped. However, the lock-in amplifier has only one current input channel. There are several

options to address this limitation. One option is to take separate sample and reference measurements. However, even though the monochromatic source is stable over the short term (on the order of minutes), the power may drift in the long term (tens of minutes to hours). Thus normalization using the reference detector must be done in real time. To accommodate this requirement, BNC cables from the detectors are combined at a coaxial mechanical relay (TohTsu Electric Co. CX-230). A mechanical relay was chosen for its negligible leakage and bias current and very low input resistance. This behavior is in contrast to an analog MUX integrated circuit where these leakage and bias currents are typically 10's of pA's to 1 nA, and the on state resistance is typically 1-100's Ω 's. A coaxial relay is used instead of a simple mechanical relay to reduce the effects of EMI and eliminate the crosstalk typically associated with non-coaxial relays. This switching is controlled by the integrated motor controller.

The reference signal for the lock-in amplifier is produced by the optical chopper. To produce this reference signal, an opto-interrupter switch is added to the chopper wheel, which turns on and off as the chopper wheel moves past it. The opto-interrupter switch is mounted on a custom board, with the board design based on a commercial chopper. The brushless motor chosen for the chopper includes circuitry to run as a standard fan motor, and thus it accepts a pulse width modulation (PWM) signal. This signal is provided by a custom

circuit built around a Microchip PIC24FJ64GB002 16-bit microcontroller, which was chosen due to existing code from a separate project. The microcontroller accepts pulses from a quadrature encoder with a push button. Turning the knob of the encoder increases or decreases the width of the PWM signal. Holding the button increases or decreases the pulse width quickly (accelerating at first) based on the last direction of the encoder knob. The PWM signal then goes to an N-channel MOSFET in common source configuration for level shifting (the microcontroller runs at 3.3 V and the motor runs at 12 V). This box also provides power to the opto-interrupter circuit (5 V) including current to the opto-interrupter LED (25 mA), and forwards the chopper signal to the lock-in amplifier. The total circuit is powered by a single 12 V supply with 3.3 V and 5 V produced on board by linear regulators. APPENDIX A contains the source code for this device (note that this code includes support for a WS2812 LED on a SPI bus to indicate the current setting and UART communications for reporting quadrature encoder changes to the computer but these are not implemented in hardware). Code is compiled using Microchip xc16 compiler and the Microchip MLA USB bootloader.

The signal coming from the relay is conducted by a BNC coaxial cable to the digital lock-in amplifier (Stanford Research Systems SR830) which measures and digitizes the signal. A lock-in amplifier uses a reference signal

to extract a narrow band signal of the same frequency from a signal containing broad band noise (including other off-frequency signals) using a homodyne detection scheme.

The stepper motors and relay are controlled by the integrated motor controller. This controller is a custom circuit designed around the Microchip PIC16f690 8-bit microcontroller. As with the chopper motor controller, this specific microcontroller was largely chosen due to existing code from a previous project. Figure 3.4 shows a schematic and a board level implementation of this circuit (note that the red, top level traces are actually hand wired in the physical implementation to avoid a two sided PCB). This board has several headers for connections related to programming the firmware (see Figure 3.4 for details). The microcontroller receives commands via UART (Baud Rate: 9600; Flow Control: None; Parity: None; Data Bits: 8; Stop Bits: 1) from the computer with a MAX203 transceiver doing the 5 V UART to RS-232 conversion. These commands are sent in 7 character packets including one start character '&' and one end char '*'. In general, these packets contain commands to either: move one of four stepper motors, change the relay switch position, change the program configuration (change motor speed, enable interrupts, etc.), or query a program value (*e.g.* current motor speed). The microcontroller receives and parses the commands and then responds with

some information related to the command such as the query result, current motor position, current switch state, etc. The microcontroller could also be configured, via commands, to accept hardware interrupts (a hardware controlled jump to a predetermined program address) with two interrupts associated with each motor, excluding the integrating sphere rotation motor (each pair could be individually enabled). With the interrupts enabled, a digital voltage change on the pins associated with either of the interrupt pairs stops the associated motor and sends a notification over RS-232.

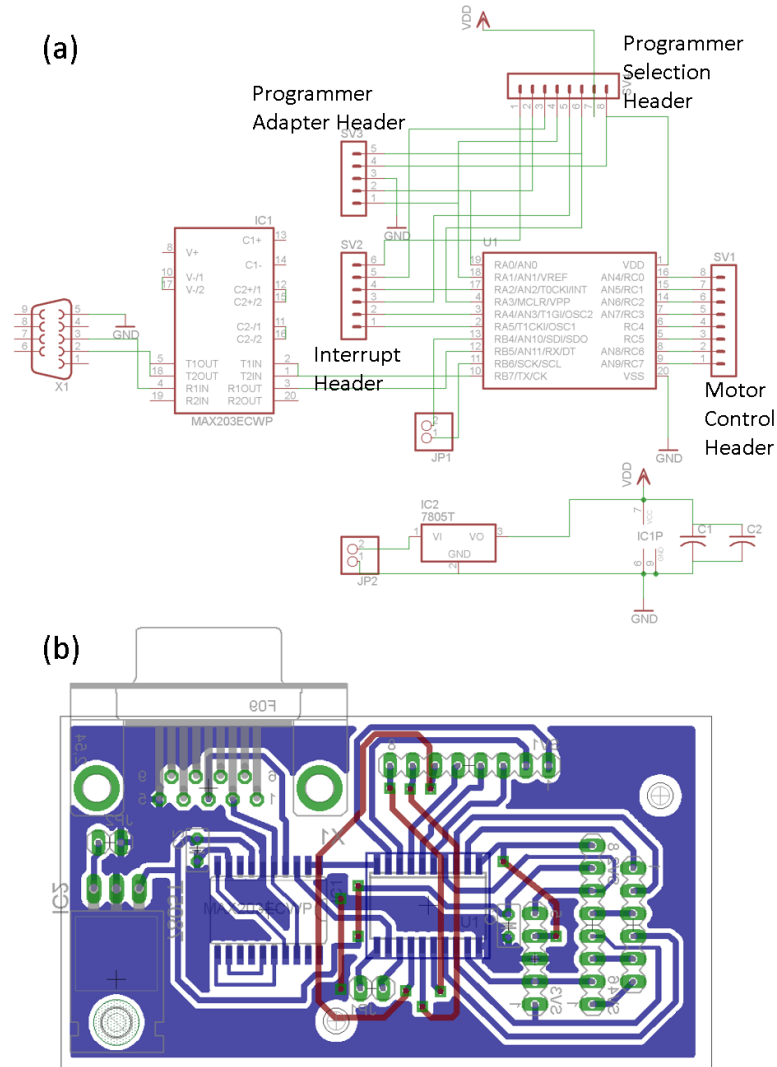


Figure 3.4: MSS control board. (a) Schematic of the MSS control board. This board is centered on the PIC16F690 microcontroller. The schematic shows several labeled headers. The Motor Control and Interrupt Headers connect as their names suggest. The Programming Header allows the chip to be reprogrammed and is pinout compatible with the Microchip PICKIT (versions 2 or 3). The Programmer Selection Header allows for disconnecting the Interrupt Header from the microcontroller (connecting every other pin on the Selection Header connects the Interrupt Header). Programming the chip with connections to peripherals can damage the chip or a PIC microcontroller firmware programmer. (b) Board level design for this circuit.

The microcontroller motor commands require a bit more explanation than given above by the general command overview. Each motor has a 2x8 bit register (step register) that stores the number of steps left for that motor to take. As steps are taken, this registry counts down. However, the motors also have a prescaler registry that it counts down for each step in the step register (the use of a prescaler instead of a larger step register is for legacy reasons). The prescaler start point is globally set and a value of 0 produces 1 step per value in the step register. The period of each step is given by a single global period value (variable from 1 to 65,536 μ s).

Stepper motors are controlled via a two-wire signal with pulses on one wire to signal the motor to step and a binary signal for direction. These wires connect to stepper motor driver boards, which are based around the A4988 Stepper Motor Driver (Pololu A4988 Stepper Motor Driver Carriers, Part #1182). The A4988 allows for setting micro stepping (partial steps of the motor via analog stepper motor coil control) up to sixteenth steps. Micro-stepping is set by hard wiring three board connections. This control scheme sacrifices holding torque for higher resolution and lower noise. The motor driver for the SPEX 500M is set to full stepping because the step resolution already far exceeds our needs, while the other motor drivers are set to sixteenth steps for

the higher resolution and because only minimal torque is required. The motor driver boards also include a potentiometer for setting the stepper motor coil current. The 500M motor driver is set to ~1 A, and the other drivers are set to ~0.3 A. These values are set by trial and error to ensure motor holding and avoid skipping steps but without overheating the motors. All motors are wired in bipolar configuration.

Interrupts are physically accommodated by a set of six pins leaving the controller board. While the controller is configured to allow for two interrupts per motor (a general configuration that allows for a start and stop point), no interrupt is used for the 500M and only one interrupt per motor is actually implemented for the steering optics motors. As noted above, these interrupt ports are connected to Hall effect switches (Allegro A3144) that are powered by the 5 V supply on the controller board. The output of these switches is an open collector BJT. To read the signal, a 1 k Ω resistor is tied to the 5 V supply. Note that electrical noise or mechanical vibration of the magnet can cause the Hall effect sensor to toggle repeatedly. To avoid multiple switching events a 0.1 μ F bypass capacitor is added in parallel with the switch output. Unused interrupt inputs are shorted to ground to avoid spurious interrupts due to noise (either electrical).

All parts of the integrated motor controller are housed in a single custom enclosure. The motor driver boards are mounted to an aluminum plate, which acts as a heat sink, and held in place with an ABS plastic back plate. This sandwich is attached to the lid of the integrated motor controller and holes are drilled in the lid to allow the driving current potentiometer to be adjusted. Slots are cut into the ABS back plate to allow for connections to the boards. Outputs to each motor, including the associated interrupts, are bundled together as a panel mount DB9 connector. Output to the relay coil which requires 12 V operation, is driven by an N-channel MOSFET in common source mode. The output is provided by a panel mount BNC connector. Figure 3.5 shows a schematic and an image of the inside of the integrated motor controller box. Full source code for the integrated motor controller is available in APPENDIX B.

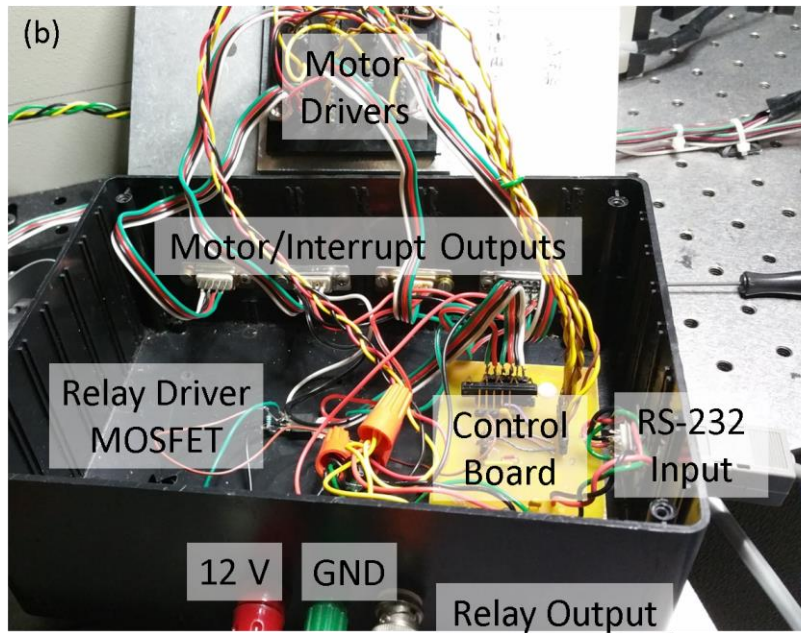
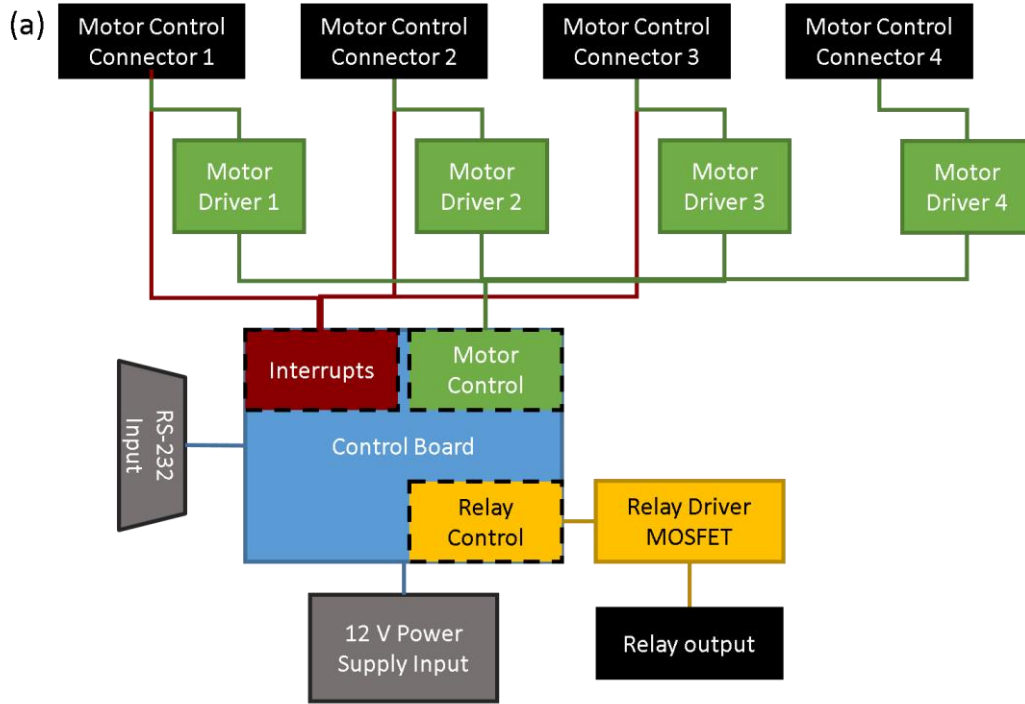


Figure 3.5: MSS control box. (a) Schematic view of the MSS control box. Sub systems are color-coded. (b) Image of the inside of the MSS control box. This box contains all the connections and electronics to drive the optics of the MSS from the computer.

3.1.4. LabVIEW front end

Figure 3.6 shows an image of the LabVIEW control program for the Multipurpose Spectroscopy Station. The controls are split into manual and automatic controls. The manual controls allow the user to select a wavelength for the monochromator to advance to (“Manual Goto”), change the relay switch setting (“Detector Select”), or move the steering mirror to one of several preset positions (“Manual Optical Channel”). The automatic controls run the absorption/transmission or EQE measurements. While not included in the “Automatic Control Options” box (for simplicity of legacy users), the untitled angle rotation box, which allows the absorption measurements to be run at multiple angles, should properly be considered an automatic control. The “Instantaneous Outputs” give the most recent values of the system during an automated measurement. The discussion below will outline each of these controls. However, this main program displays only a small fraction of the code with sub-VI’s (LabVIEW virtual instruments) remaining hidden. Exploding the full VI tree would be enormous and so the source code is available upon request rather than provided in the appendix.

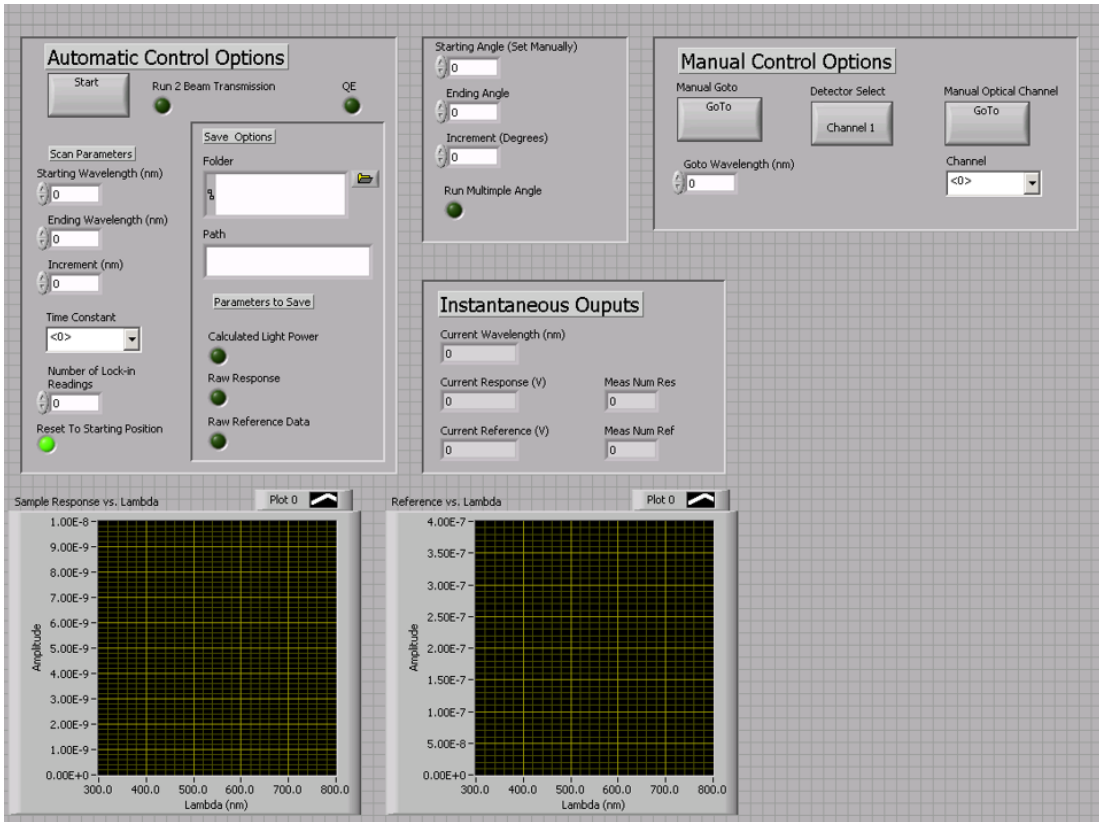


Figure 3.6: LabVIEW frontend for MSS system. This panel provides all the controls for the MSS including manual controls used for setup and automated controls for measurement runs. This also displays some instantaneous data for monitoring runs.

Instead of a full description of the extensive code, the basic function of the LabVIEW program will be given here. The program starts by finding the RS232 ports used by the microcontroller and the lock-in amplifier by querying all ports for an identifying response (if the program fails to find either of these, the system quits with a message to the user). With these ports enumerated, setup routines are executed to set each device to default values. Concurrent with the setup, a popup appears to the user, requesting the current setting of

the SPEX 500M because, as mentioned above, this must be manually read and input. This value is stored and updated throughout the program routine. LabVIEW then enters an infinite loop during which the program waits for some action on the front panel and upon receiving an action, it checks whether the “Start” button or any of the “Manual Control Options” buttons were pressed.

The manual controls underlie all run subroutines of the automatic controls and will thus be described first. If the “Goto” button is pressed, the program compares the current monochromator setting to the desired setting and moves the SPEX 500M motor accordingly. The movement uses an acceleration routine whereby the microcontroller step speed is updated based on the number of steps taken so as to ramp up and then down the motor speed. This reduces wear and prevents skipping steps (it also plays a nice series of tones). If the “Detector Select” button is pressed, LabVIEW sends a command, based on the current switch setting, to the microcontroller to toggle the relay switch state. If the “Manual Optical Channel” button is pressed, the program enters the “Microcontroller-Optical Channel Select.iv” sub-routine. This routine checks the current microcontroller speed setting, stores this value, sets the microcontroller motor speed to a low value and the prescaler to 0 (for fine control), tells the steering motor to move a full revolution, then activates the global and individual motor interrupts. When the steering mirror table rotates

to the zero position (indicated by the Hall Effect sensor) an interrupt is triggered and the motor stops. The subroutine then turns off the interrupts, rotates the steering mirror table to the desired position based on the setting from the "Channel" drop down menu, and resets the motor speed and prescaler back to the previous values.

The automatic controls offer a number of options. There are several run types but all of the runs will use "Scan Parameters" and "Save Options". The "Starting Wavelength", "Ending Wavelength" and "Increment" are, as the names suggest, the starting, ending, and increment per measurement of the monochromator setting. The "Time Constant" defines the integration time that the lock-in will use for each measurement and has one of three options: 300 ms, 1 s, and 3 s; where increased integration time equates to higher accuracy but longer run times (note that many other options are available from the lock-in but this covers most of the range of interest). The "Number of Lock-in Readings" defines the number of measurements taken at each wavelength. This setting is primarily for legacy reasons, as it is generally better to increase integration time rather than do multiple measurements. However this setting may potentially be used to easily achieve effective integration times beyond 3 s. The "Save Options" allow the user to choose location and type of data to save. By pressing the folder icon, the user can select a destination folder for

saving files. The “Path” box allows the user to input a base file name. If the user doesn’t set these file name options, they will be prompted at the end of each wavelength scan (this prevents the automated 2 beam measurements, discussed below). Finally, the user can decide what types of data to save by clicking on the green buttons under “Parameters to Save.” By default, wavelength and the ratio of the measured current from the sample (“response”) and the reference photodiodes, are recorded. The user can add raw data from the reference and/or response results and the calculated light power (EQE measurements only). In practice the reference and response currents are almost always saved for potential diagnostic reasons. With all of these options specified, the program will automatically save data in comma separated variable form with a date and run type prefix added to the filename. Lastly the user can tell the program to do multiple runs with a rotation of the integrating sphere center post between each run by toggling the “Run Multiple Angle” button and specifying the desired start, end, and increment angles. This will generate a file for each angle position with a prefix added to the filename specifying the angle of that sub-run. In practice however, this option was not used. Note that this option has no effect on “QE” runs (the program option to measure EQE).

All runs follow the same general process. The monochromator is set to the starting wavelength, the filter is rotated to a non-filter position (filter out of beam path) and the steering mirror is rotated to shine light along the desired path. The program then begins a loop. The loop starts by setting the relay to read from the reference detector. The program checks if the next wavelength setting will require a filter and rotates the filter in place as needed. The wavelength is then incremented. The lock-in is switched to a short integration time so that it can settle quickly, followed by a short wait and then a command is sent to start an auto-gain routine on the lock-in (there is a built in function to find the optimal settings). The integration time is then reset to the value defined by the user, and a longer wait timer is started with the length based on the chosen integration time (per the lock-in manual). At the end of this wait, LabVIEW repeatedly checks the lock-in current reading to determine if the measurement is stable. If the value is unstable, this implies a fault with the setup, and an error message is given to the user. Once stable, the program reads from the lock-in amplifier based on the "Number of Lock-in Readings" option. The relay is switched to the response detector, and the read process is started again (set short integration time, wait, set user defined integration time...). After completing both measurements the loop is reset. This loop repeats until

the wavelength reaches the end value. The entire measurement may be repeated depending on run type with appropriate changes.

Several run types can be chosen for the MSS. The basic options for run type are “Run 2 Beam Transmission” or “QE”. The 2 beam transmission option is generally used for absorption and transmission measurements. The light shines through the main port for one wavelength scan, then through the secondary port in a second wavelength scan to account for second order reflection and absorption in the sample (discussed in more detail below). This concludes with the output of two files, one for each scan. A “QE” run does a single sweep of the wavelength range but with the steering mirror sending light to the QE stage. The user first does a run using the calibrated detector to measure relative power at the QE stage. They then do a second run using their sample. Upon completion of this run, the user is prompted to give the reference file that contains the previously measured relative power at the QE stage. LabVIEW then uses this power data to calculate the EQE.

3.1.5. Measurement details

Though a full standard operation procedure (SOP) for the MSS can be found in APPENDIX C, a brief overview of measurement and data analysis will be given in this subsection. EQE is defined as the steady state number of

electrons per second generated from the device divided by the steady state number of photons per second incident on this device. Thus EQE requires two measurements. For the first run, the user puts a calibrated detector with responsivity, R , at the EQE stage to measure the relative (to the reference detector) power arriving at the stage, given as the responsivity times the relative current, I_{cal} . The second measurement, the user places their sample on the stage and the relative current, I_{sam} , is measured. EQE is then given by:

$$EQE = \frac{I_{sam}/e}{I_{cal}/(Rhc/\lambda)}, \quad (3.1)$$

where e , h , c , and λ are the electron charge, Planck's constant, speed of light in vacuum, and the wavelength of light respectively.

The absorption (or transmission) measurement also takes two runs. The first one has no sample in the sphere, or on the main port clip, to establish a baseline relative system response for light shining through the main port, $I_{b,1}$, and the secondary port, $I_{b,2}$. The second run is with a sample inside the sphere and measures the effect on system response when the sample is added, again for main port, $I_{sam,1}$, and secondary port, $I_{sam,2}$. The absorption, A , and transmission, T , are calculated by:

$$A = 1 - \frac{I_{sam,1} \frac{I_{b,2}}{I_{sam,2}}}{I_{b,1}}, \quad (3.2)$$

$$T = \frac{I_{sam,1} \frac{I_{b,2}}{I_{sam,2}}}{I_{b,1}}, \quad (3.3)$$

where the variables are grouped to emphasize that the ratio of the secondary port measurements ($I_{b,2}/I_{sam,2}$) determines how much the main port sample measurement should be corrected to account for signal lost to second order absorption. Finally, with EQE and absorption measurements both completed, one can determine the internal quantum efficiency IQE, defined as the number of electrons per second collected per photon absorbed. This is given by:

$$IQE = \frac{EQE}{A}, \quad (3.4)$$

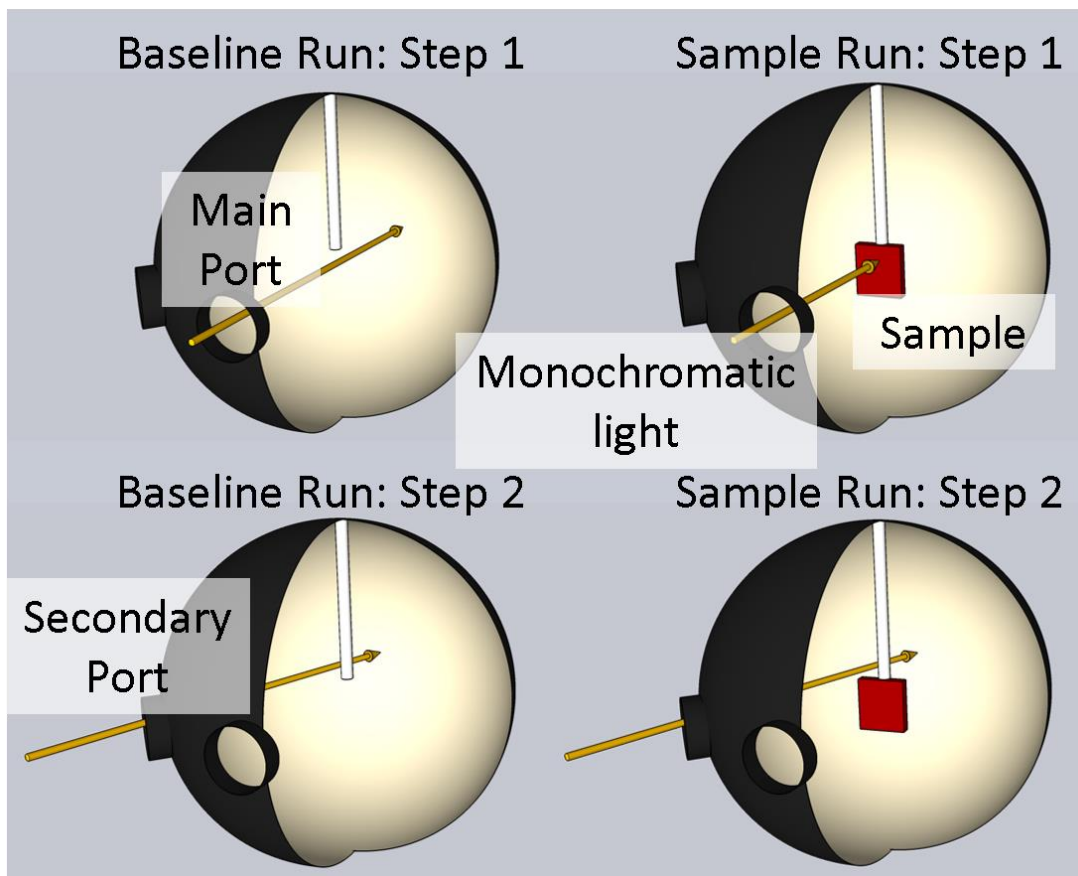


Figure 3.7: Schematic of the absorption measurement sequence. The user makes two sets of measurements: one with the sample and one without.

3.2. Scattering Distribution Station overview

The Scattering Distribution Station (SDS) is designed to measure how light scattering from samples varies with both incident and emission angles with high angular resolution. Figure 3.8 shows the basic parts and operation of the SDS. This system allows users to determine the wavelength dependent reflected and transmitted scattering distribution. Variants of these measurements include internal scattering distributions and haze

measurements. The basic components of the system include, a stationary laser, dark box casing, rotary sample holder post, detector arm, beam optics, and electronics. The user places a sample at the center of the apparatus on the rotary sample holder post. Beam steering optics direct the light into the dark box and illuminates the sample. The detector arm and the rotary sample holder post can then be independently rotated and current measurements are made at each detector and sample angle.

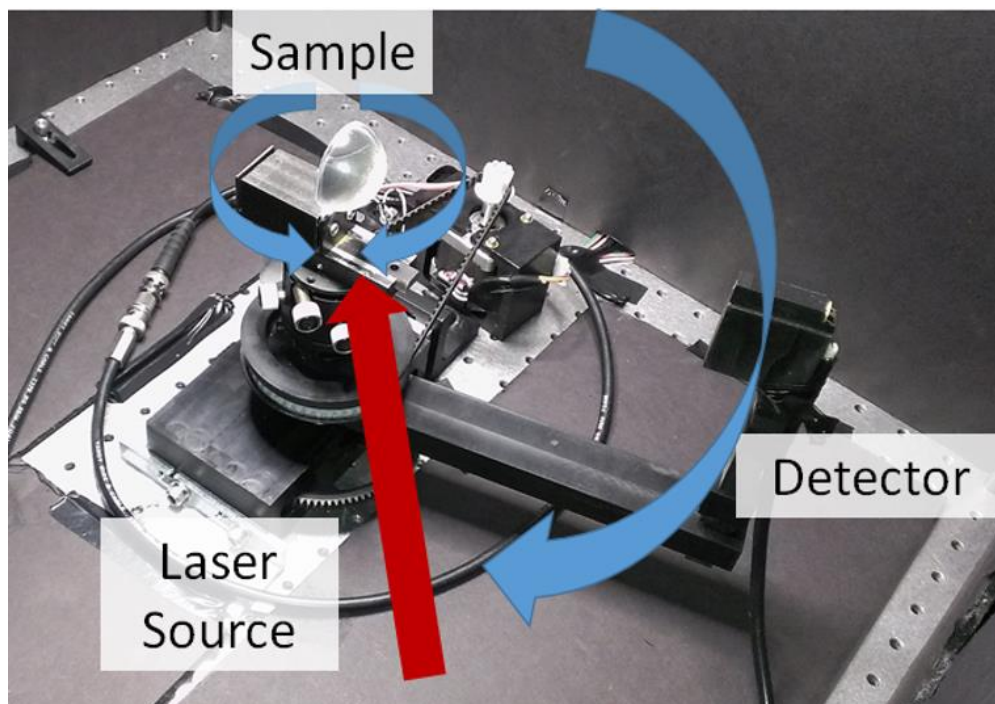


Figure 3.8: Image showing basic operation of the Scattering Distribution Station.

3.2.1. SDS mechanical hardware

Figure 3.9 depicts the hardware parts of the SDS. The rotation hardware is centered on two concentric drive rods. The outer drive rod is a 1/2" tube of Teflon with inner diameter of 3/8" and is attached to the detector arm and the spur gear which is designed to mate with a worm. The 3/8" inner rod, which resides in the Teflon tube, is stainless steel and is attached to the timing belt pulley and to the sample holder. A black Delrin bearing block holds two 1" OD × 1/2" ID bearings (press fit). The bearing block is attached to the table by mounting brackets. The Teflon tube is press fit into the two bearings, thus fixing the rotatory assembling in space. The timing belt pulley and spur gear are driven by a timing belt and worm gear respectively. The drives are powered by stepper motors attached to the optical table by mounting blocks (black Delrin for the sample drive and aluminum for the detector drive).

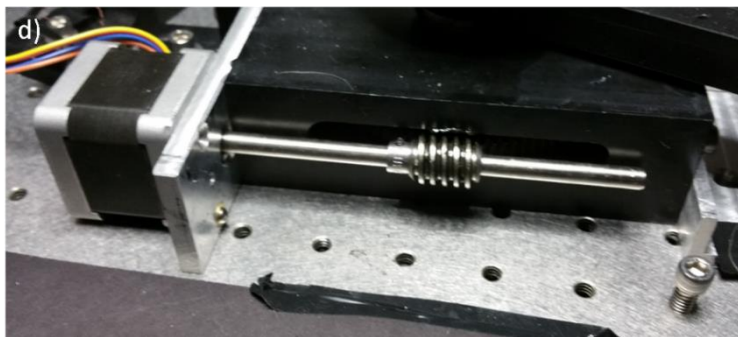
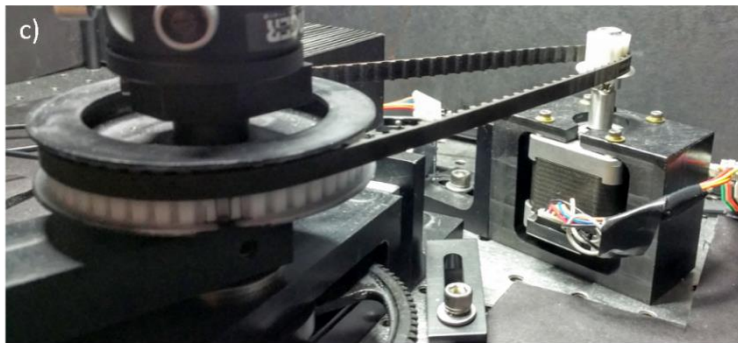
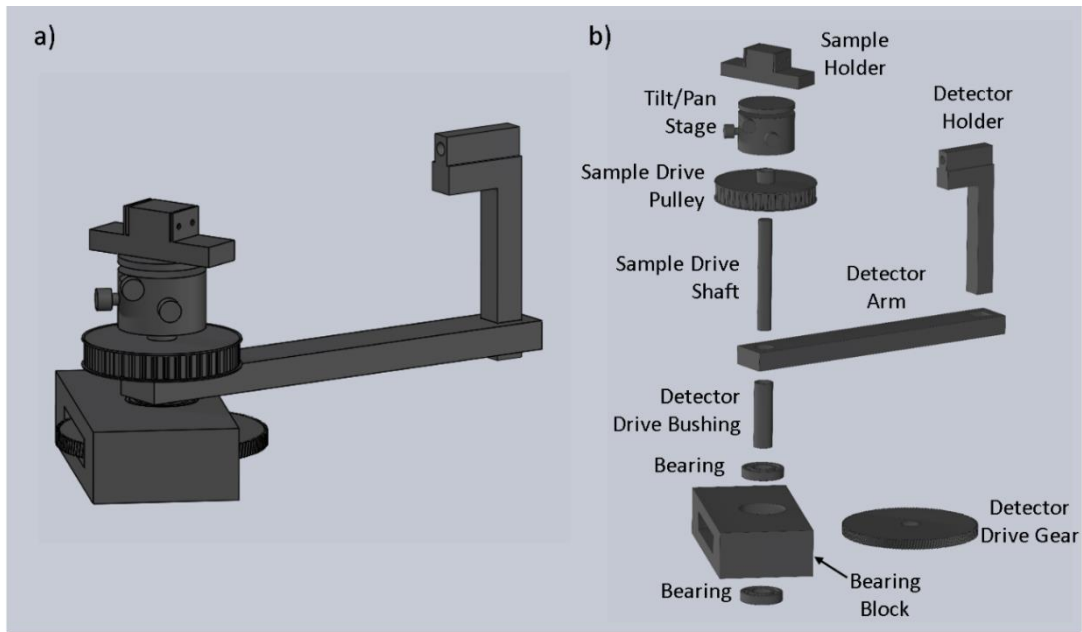


Figure 3.9: DSS mechanical components. (a) 3D model of the main SDS mechanism. (b) Expanded view of the same mechanism shown in (a). (c) Image of the motor, belt, and pulley for the sample drive mechanism. (d) Image of the motor, worm and gear for the detector drive mechanism.

The detector arm is made of two parts. A $\frac{1}{2}'' \times 9'' \times 1''$ black Delrin beam attaches to the Teflon tube and extends away from the center. At the end of this beam is a $\frac{1}{2}''$ square hole (with relief holes at the corners) that goes all the way through the beam. The beam also has a $\frac{1}{4}'' \times 7'' \times \frac{1}{2}''$ slot cut in the underside to reduce weight. The detector housing, is an L shaped black Delrin piece. The long end of the L is an undersized $\frac{1}{2}''$ square shaft that fits into the beam. The short end of the L forms a $\frac{1}{2}'' \times 1'' \times 1''$ block and extends towards the sample holder. At the top of this section a 0.23'' diameter hole is drilled facing back toward the sample holder. At the back end of this hole, a Si photodiode detector is mounted (Thorlabs FDS100) which has square active area with a corner to corner width of 0.2''. From the front detector housing to the face of the detector is 1.125''. This gives the detector housing an absolute maximum viewing angle of 10.8 degrees and the viewing angle at the center of the detector is 5.9 degrees. This small angle is meant to reduce the acceptance of stray light.

The sample holder is made of three pieces. The first is a tilt, pan, and rotation stage mounted on the end of the stainless steel drive rod. This allows the user to correct for non-perpendicular sample mounting by making fine-tuned adjustments to how their sample holder is tilted. The second is a brass

dove tail slide with a locking lever, which is attached to the tilt, pan, and rotation stage with its sliding axis passing through the center of the stage. This slide allows the user to move their sample about the center of the rotation axis, which is primarily used to account for differences in sample thickness. Lastly, a black Delrin block is attached to the top of the slide. The block has one slit in each end, which points up away from the table. The slits are designed to hold the samples and have different thicknesses to hold a variety of sample sizes. These slits can be pulled closed to grip the user's sample by tightening screws in the clip.

3.2.2. SDS electrical

The Scattering Distribution Station uses the same microcontroller board (with the same firmware) and stepper motor driver electronics as the MSS. See Figure 3.4 for the schematic. However, the control scheme is quite different which results in a few important changes in how this board is connected. First, the system uses only two motors so the last two motor ports are left disconnected. Second, the SDS uses no interrupts so these are all connected together with a header that is connected to ground in order to prevent any spurious interrupts.

The photodiode is connected by a BNC cable to a Keithley 2400 source meter. The source meter is remotely controlled by a computer running the LabVIEW frontend for this setup (described in the next section). The source meter is connected to the computer via RS-232 and is set to zero volts to minimize noise and is set to measure current.

3.2.3. LabVIEW frontend

Figure 3.10 shows the LabVIEW control screen used to drive the SDS. These controls allow the user to make scattering measurements by sweeping both the angle of the sample and of the detector (referenced to the laser beam). The user must first set up the communications for the Keithley source meter by choosing the correct serial port under the “VISA resource name” drop down menu and entering in the data under “Serial Configuration” to specify the communications protocol. Note that it is unlikely the “Serial Configuration” would ever need to be changed from the defaults, but it is possible if using an oddly configured Keithley 2400. The textbox menu item titled “port excluded from search for Microcontroller” should be filled with the index of the serial port selected for the Keithley. This setting prevents the microcontroller setup subroutine from sending an improperly formatted message to the Keithley. The user then inputs the angle start point, end point, and increment, which

must be >0 , for both the “Sample Angle” and “Detector Angle”. The start point should be set by the user as the current position of the sample stage and detector arm respectively. When the user starts the LabVIEW program, all of this setup data is read and commands are sent so that the detector arm moves an increment and a current measurement is made by the source meter. This step is repeated until the arm reaches the end point. The mechanism then returns the arm to the start point, rotates the sample, and repeats the detector sweep/measurement. This procedure continues until the sample reaches the end point angle. During the run, the graph shows a plot of the measured current vs. detector angle for the sweep in progress. At the end of the measurement run, LabVIEW prompts the user to provide a file name for saving the data.

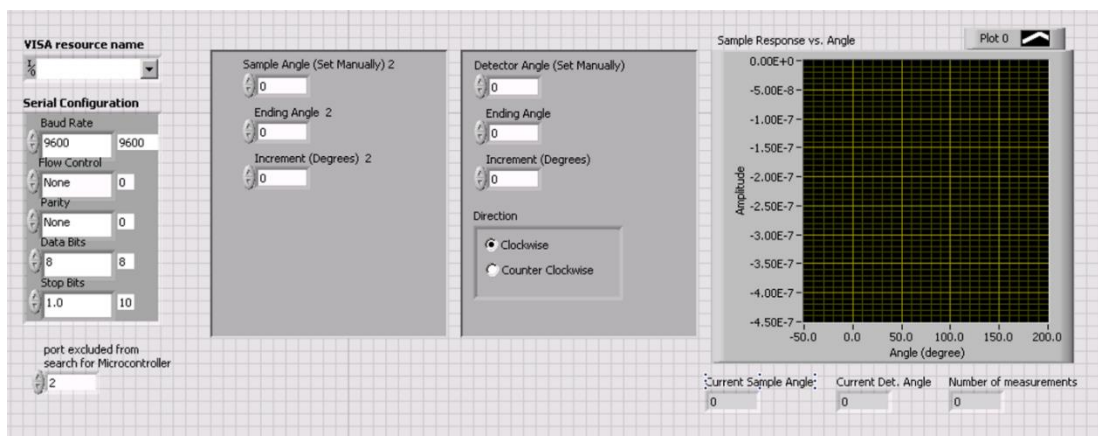


Figure 3.10: Image of the LabVIEW frontend used to control the SDS. This allows the user to set the measurement parameters and get the current readout of the measurement.

The behind the scenes functions of the program, are similar to the MSS and uses all of the same subroutines for communication with the microcontroller. Rotation of the sample and detector is achieved using the same methods employed in changing the wavelength of the MSS but with a different number of steps per effect (angle here instead of wavelength) for each motor. The other primary difference is the use of the Keithley rather than the SRS lock-in amplifier for measurement of current. The setup and measurement for the source meter are controlled with VI's written by the Keithley company.

The SDS program also has another variant that allows the user to change the wavelength of a Fianium Supercontinuum Laser. This LabVIEW program is a combination of the code described above and code produced by Dakang Ma based on VI's from Fianium. This has the same basic functionality but with a couple of additions and updates. The front end for this routine is shown in Figure 3.11. The first modification is the removal of the "Serial Configuration" options because, as previously mentioned, these virtually never need to be changed from the defaults. The second modification is the addition of the Fianium setup controls. The "AOTF Port" selects whether the laser will use the IR or visible range. The "Power (%)" option lets the user vary the output power of the laser (this is generally set to 100). The "Channel" option refers to

an internal setting on the Fianium and should be set to 0. The “Starting Wavelength”, “Ending Wavelength”, and “Wavelength Increment”, setup the wavelength sweep. Lastly, a “Save Options” is available to do automated saving of files. The user chooses a save folder and gives a filename suffix. This SDS program variant runs in the same manner as the base program. However, after each set of angle sweeps, rather than prompting the user for a save file, data is automatically saved, and the wavelength of the Fianium advances one increment (note that the user is still prompted for a save file if nothing is selected in “Save Options”). This process continues until the wavelength of the laser advances to the “Ending Wavelength”. The full source code for the SDS LabView program along with the program for this variant is available upon request.

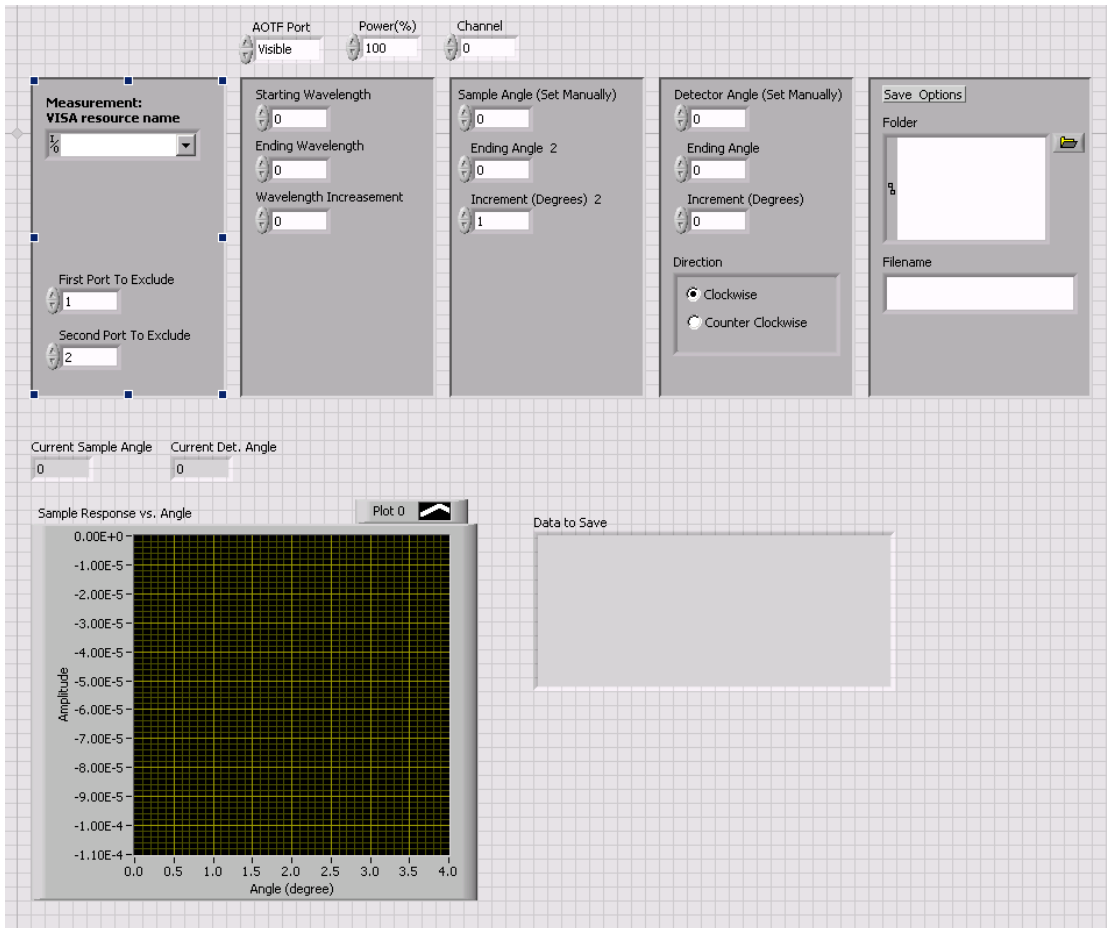


Figure 3.11: LabVIEW frontend for the SDS variant which also sweeps the wavelength of a Fianium Supercontinuum laser. This program functions the same as the base program, but the angle sweeps are run at different illumination wavelengths. After each angle sweep, a new file is saved containing the data for that sweep.

An overview of the SDS operating procedures will be given here. The setup of the system starts with laser alignment. A laser should be guided into the measurement chamber. The beam height should be appropriate for the sample when held in the sample holder. This beam should be parallel to the

table and should pass over the center axis of the sample holder. The former can be checked by measuring the beam height as it enters the chamber and as it hits the back wall to verify that they are equal. The latter can be addressed during sample/beam alignment.

The nature of the alignment is dependent on the type of sample being measured (either planar or hemispheric for this work). Figure 3.12 and Figure 3.13 give a visual guide to the basics of the alignment of planar and hemispheric samples respectively. For planar samples, pan and tilt can be set by ensuring that the laser beam is reflected at the same height at which the beam enters the chamber. This should be checked with the sample at $\sim 0^\circ$ and $\sim 45^\circ$ so that the alignment is fixed in space along both rotational axes. The radial position of the sample along sliding axis can be fixed by ensuring that the laser spot on the sample doesn't move as the sample drive shaft is rotated. If the pan, tilt, and radial position alignments cannot all be met simultaneously, it implies the beam is not passing over the central axis of the SDS. For hemispheric samples the process includes additional alignment. Pan, tilt and radial position can be fit as before but by using rear planar surface of the hemisphere (if the rear surface scatters light, the inner planar surface may instead be used). Note that the hemisphere produces two distinct reflections when the spherical side is facing the beam: one from the curved surface and

one from the planar surface. The reflection from the curved surface can be used to fix the hemisphere in the direction perpendicular to the sliding axis and in height above the sample holder. Correct alignment should result in the collinearity of the incident beam and both reflected beams at 0° and no change in the position of the curved surface reflection as the sample is rotated. Lastly, for either sample type the height from the detector housing should be adjusted to the desired height.

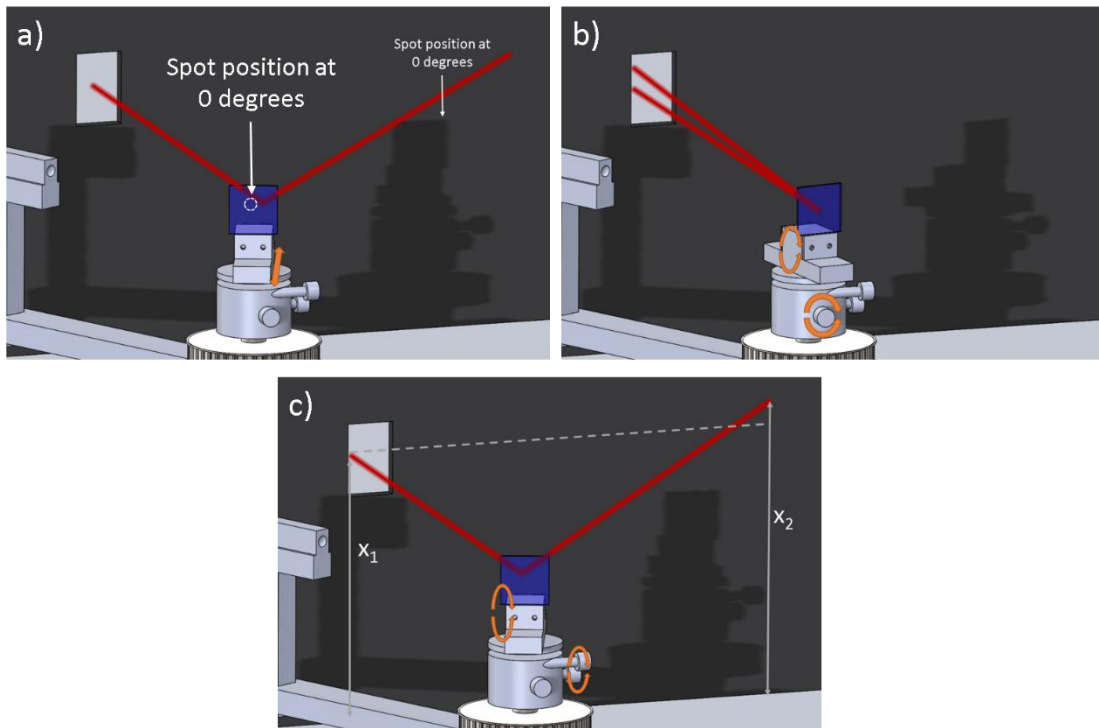


Figure 3.12: Basic alignment procedure for planar structures when using the SDS. (a) Adjusting the radial direction using the sample holder sliding mechanism. The laser spot on the slide should not move as the sample is rotated. (b) Adjusting the tilt using the pan/tilt stage. The beam should return along the incident path. (c) Adjusting the pan using the pan/tilt stage. The reflected beam should be at the same height as the incident beam ($x_1=x_2$) for all sample angles.

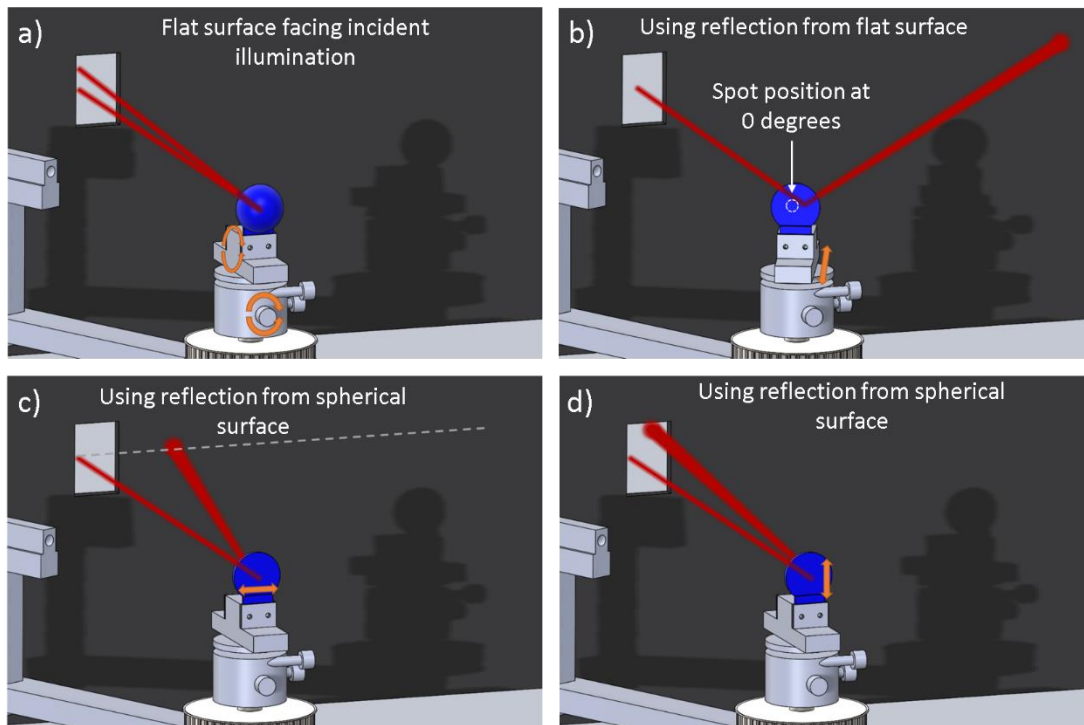


Figure 3.13: Basic alignment procedure for hemispherical structures when using the SDS . (a) Adjusting the pan/tilt (only tilt shown here). User should follow the procedure from Figure 3.12 above for both pan and tilt but using a reflection from a flat surface. (b) Adjusting the radial direction using the sample holder sliding mechanism. The laser spot should not move as the sample is rotated (same as above). (c) Adjusting the side-to-side position of the hemisphere in the sample holder. The beam reflected from the curved surface of the hemisphere should return along the incident path. (d) Adjusting height of the hemisphere in the sample holder. The reflected beam should be at the same height as the incident beam for all sample angles.

With alignment complete, the user should manually set the starting angles for the sample and the detector. The sample stage can be rotated by

hand, but the detector arm must be rotated using the computer (this is the nature of worm gears). A motor jog program is available to accomplish this task and the user should estimate the detector's starting angle and enter this into the LabVIEW program.

Once the program has run, the data can be analyzed. Because the starting angles are only estimated, the zero position of these angles must be assigned using the acquired data. At zero degrees, the detector housing blocks the incident light and thus can be used to determine the detector zero angle. The specular reflection from the sample, generally creates a strong peak in the scattering when the detector angle matches the sample angle zero and thus the sample angle can be found if the detector angle zero is already known.

3.3. High Voltage Square Wave Drive

As the name implies, the High Voltage Square Wave Drive produces a square wave with variable high voltage. The system creates bipolar voltages up to 200 V with fast slew rates and thus high peak currents from a single high voltage supply. The typical way to produce a bipolar drive from a single supply is with the use of a MOSFET H-bridge (see Figure 3.14a). While MOSFETs with very wide source to drain ranges (100's of volts) are commonly available, MOSFETs with high gate to source break-down voltages (>30-50

volts) are essentially non-existent. This is a non-issue for the low side N-MOS in a standard h-bridge but is fatal for the high side P-MOS when the supply voltage is high. To understand this, consider one side of the h-bridge: starting with both gates driven low, to turn on the N-MOS and to turn off the P-MOS, gate to source voltage of the P-MOS is set to the supply voltage which will destroy the P-MOS. To overcome this limitation, an N-MOS only driver can be used (see Figure 3.14b). However, turning on the top N-MOS would require a voltage that exceeds the supply voltage. The system uses a charge pump to overcome this limitation. This circuit charges a capacitor in series with a diode. Because the diode is connected to the voltage supply, charge flows into the capacitor when the lower N-MOS is turned on. If both ends of this diode-capacitor series circuit are then connected to the high voltage supply the capacitor cannot discharge and the voltage at the junction between the capacitor and diode is raised above the high voltage supply. The high side MOSFET can be turned on by connecting this capacitor junction to the gate of the top N-MOS. Fortunately, a single IC, the IRS2453, is available to control the N-MOS h-bridge, including the charge pump, internal frequency generator (nearly identical to the classic 555 CMOS timer), and timing control (to prevent top and bottom MOSFETs from being active concurrently). The circuit for this chip is taken directly from the datasheet with FQS4901 used for the N-MOS

transistors and the single timing resistor (connected pin 4) replaced by a pseudo logarithmic resistor network. By changing the potentiometer setting in this network, the switching rate can be changed from ~70-7000 Hz. The system has a switching time of approximately 100 ns. Figure 3.15 shows the physical implementation of this circuit and a circuit diagram.

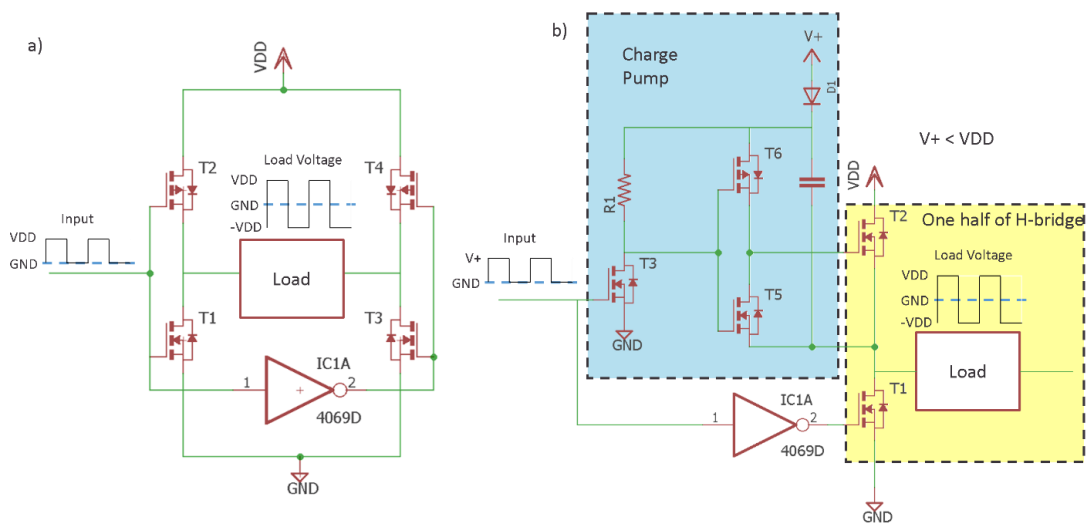


Figure 3.14: H-bridge configurations. (a) Schematic of standard H-bridge using P-MOS and N-MOS. A PWM signal at the input creates a bipolar voltage across the load. This circuit fails for high VDD (limited by the typically low gate to source voltage specification). (b) Schematic of one half of an N-MOS H-bridge with a high side charge pump. This circuit can handle very high VDD (limited by the typically high source to drain voltage specification).

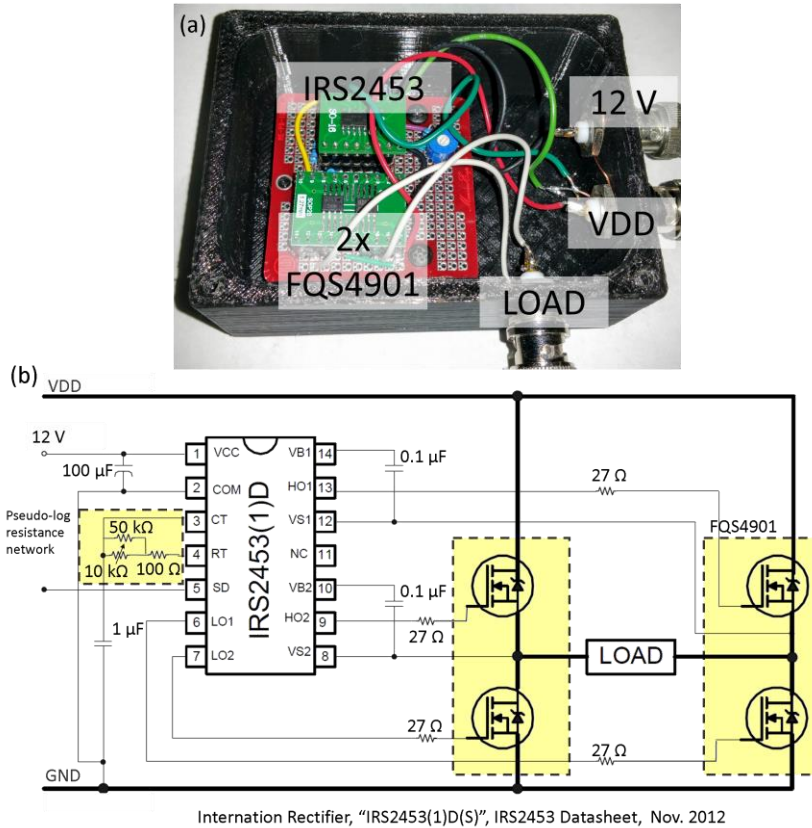


Figure 3.15: Implementation of the High Voltage Square Wave Drive. (a) Physical implementation of the High Voltage Square Wave Drive. Major components are marked. (b) Schematic of the High Voltage Square Wave Drive copied from the IRS2453 datasheet annotated with component values. Note that the resistor connected to pin 4 in the datasheet has been removed and replaced by a Pseudo logarithmic resistance network using the discrete components shown.

3.4. Instrumentation applications

As mentioned above, this equipment has been used in other work to which I have contributed but is not described elsewhere in this thesis. An

investigation of silver nanowire paper based electrodes [83] used the MSS for transmission measurements and the SDS for angularly resolved scattering. Work on paper based antireflection coatings for Si solar cells [82] used the MSS for transmission and absorption with angle dependent characterization. A study of radiation pressure on polymer dispersed liquid crystals [85] (these materials are discussed further in chapter 6) used the MSS for transmission and absorption measurements and the SDS to characterize total momentum transfer from visible radiation. The equipment has also been used for studies in which I was not directly involved. This includes work on high haze nanostructured paper [88], a paper based antireflection coating for GaAs [86], nano-imaging of solar cell open-circuit voltage [89], and dielectric nanospheres for solar cells [84].

Chapter 4: Experimental demonstration of internal light scattering

The angular distribution of light scattering from a textured surface in air can be determined using a standard gonioreflectometer. However, for light trapping, it is the scattering into the material under consideration that is important, rather than the scattering into air. This chapter describes the experimental technique we developed to determine this internal scattering, which enables us to evaluate the effectiveness of various light trapping structures.

4.1. Overview

Minimization of the device thickness is an important goal in photovoltaic designs as it generally lowers costs and reduces bulk recombination losses. The drawback of thinner devices is lowered absorption; however, by employing light trapping, this fundamental trade-off can be circumvented. An enormous variety of strategies have been experimentally and theoretically investigated. These approaches include texturing [71], plasmonic nanoparticles [23], [90], gratings [11], [41], [91], nanowires [44], [92], nanocones [52], [53], [93], dielectric particle arrays [41] etc. Many of these techniques require lithography, high temperature processing, or hazardous

chemicals and are hampered by high surface recombination [43]. A cost effective and simple alternative is the addition of random dielectric nano- or micro- scatterers. These may be easily applied as a back-side reflector/scatterer and have been shown to be effective for light trapping [94]–[97].

To properly design and optimize cells using these random dielectric nanoparticle reflectors, a detailed understanding of their scattering properties is required. There is a large body of literature on scattering in diffuse materials [98], [99]. Much of it is concerned with calculating the fractions of scattered and directly transmitted light in the diffuse medium rather than its angular distribution and it is usually assumed that the mean free path is much greater than the wavelength of light, which is not the case for densely packed wavelength-sized particles. Calculations have also been done outside of this low density regime using Monte Carlo simulations [100], N-flux radiative transfer method [101], a 1-D semi-coherent method [97] and more recently rigorous coupled wave analysis [102] in order to determine the fractions of scattered and direct light in diffuse media. However, often the scattering material is dense, randomization is assured and the internal scattering of the diffuse media is not the primary concern. In such cases two models are generally used to describe or compare the absorption due to these scatterers: either the material is taken to produce Lambertian scattering from the back side

of the absorber or it is assumed that within the scattering material the light is fully randomized but is limited by a critical angle as it enters the absorber [103]. Neither of these models accurately describes the actual scattering in the cell. One way to improve the modeling would be to measure the scattering distribution inside the absorber, but this measurement is not in general possible with planar structures due to a portion of the light experiencing total internal reflection.

In this chapter we present an improved characterization method that uses a hemispheric lens and reflectometry to extract information about the internal scattering distribution. With the scattering distribution known, we are able to reassess the scattering models. We use this method and improved modeling to demonstrate the importance of the interface between the scatterer and absorber in determining the resulting absorption. We find that the scattering distribution is best described by an ensemble of effective indices at the absorber/scatterer boundary. Finally, we demonstrate the accuracy of this technique by comparing its predictions to several experimental configurations. We find that our procedure allows for high accuracy predictions of absorption based on our measured scattering data.

4.2. Modeling of random dielectric scatterers

One of the simplest approaches to model scattering inside a slab or film is to assume perfect reflection off the back surface and complete randomization of the incident light (Fig. 1a). This model results in the well-known Lambertian scattering intensity distribution of $I_o \cos(\theta)$ in units of power per unit area per steradian, where θ is the angle from the surface normal. This expression is derived from simple geometric considerations assuming photons are equally likely to be reflected in any direction. If the sample has a back reflector and can support a large number of modes (approaching a continuum), the Lambertian distribution results in absorption given by [104]:

$$A = \frac{(1 - e^{-4\alpha h})T_{in}}{\left[1 - e^{-4\alpha h} \left(1 - \bar{T}_{esc}/n_{abs}^2\right)\right]} \quad (4.1)$$

where, α is the absorption coefficient, h is the thickness of the absorbing layer, n_{abs} is the index of refraction of the absorbing layer, and T_{in} is the incident transmitted fraction at the top interface. \bar{T}_{esc} is the weighted transmitted fraction of light exiting from the slab through the escape cone (defined as $\bar{T}_{esc} = 2n_{abs}^2 \int_0^{\sin^{-1}(1/n_{abs})} T_{esc} \cos \theta \sin \theta d\theta$ where T_{esc} is the transmission coefficient). For an ideal antireflection coating, we can also make the approximation $T_{in} = \bar{T}_{esc} \approx 1$ to further simplify Eq (4.1). For a thick material (*i.e.* $h \gg \lambda$) with weak

absorption ($\alpha h \ll 1$), e.g. in bulk silicon near the bandgap, the absorbed fraction reduces to the well-known $4n^2$ limit [105], [106]:

$$A = 4n_{abs}^2 \alpha h \quad (4.2)$$

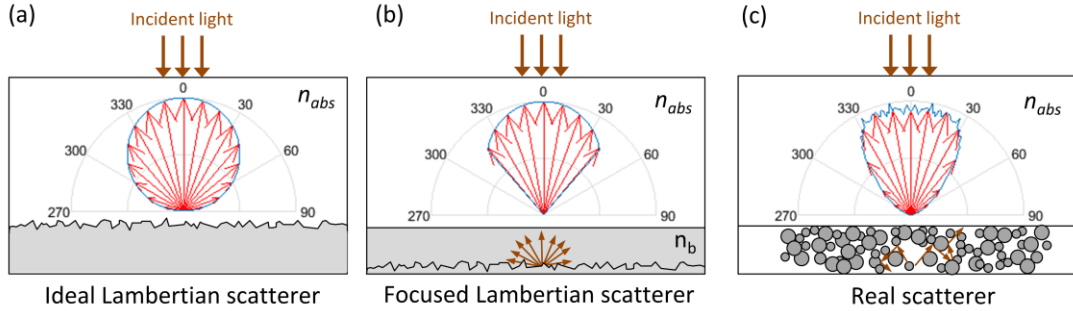


Figure 4.1: Scattering profiles within an absorbing slab of refractive index n_{abs} for (a) an ideal Lambertian scatterer, (b) a focused Lambertian scatterer, and (c) a real scatterer consisting of barium sulfate particles on the back of a GaP substrate.

The Lambertian model however is only a simple model for scattering and poorly describes real dielectric scatterers. New models are needed in order to determine the scattering properties, and hence the absorption, that result from real dielectric back scatterers. An improved model assumes that light inside the scattering material is fully randomized but can only emit into the absorber through a fraction of the full 2π steradians. This fraction is determined by the critical angle defined by the index contrast between the sample, n_{abs} , and the binder or filler of the dielectric scatterer, n_b [94], [103]. This

scattering distribution is sometimes referred to as a focused Lambertian distribution, and is given, again in units of power per unit area per steradian, by:

$$I(\theta) = I_0 \cos(\theta) \left(\frac{n_{abs}}{n_b} \right)^2 \quad \theta < \sin^{-1} \frac{n_b}{n_{abs}}, \quad (4.3)$$

$$I(\theta) = 0 \quad \theta > \sin^{-1} \frac{n_b}{n_{abs}}$$

This equation is derived from the assumptions above by mapping angles from inside the scatterer to inside the absorber using Snell's law. Note that this formula is only valid when $n_b < n_{abs}$. If this condition is not satisfied, further scattering into evanescent and surface modes may occur and further increase the absorption. For $n_b < n_{abs}$, this distribution results in absorption less than the $4n^2$ limit. Under the same assumptions used to derive the $4n^2$ limit, the absorption can be approximated as:

$$A \approx 2Khn_b^2 \quad (4.4)$$

where K is the effective absorption coefficient defined by:

$$K \equiv \frac{-\ln(1 - \bar{A})}{h} \quad (4.5a)$$

Where

$$\bar{A} \equiv 2 \left(\frac{n_{abs}}{n_b} \right)^2 \int_0^{\theta_c} \left[1 - \exp\left(-\alpha h / \cos \theta\right) \right] \cos \theta \sin \theta d\theta \quad (4.5b)$$

And

$$\theta_c = \sin^{-1} \frac{n_b}{n_{abs}} \quad (4.5c)$$

Here \bar{A} is a weighted average of the absorption due to different ray optic paths [103]. When the absorption cannot be calculated under these simplifying equations, a more complex system of equations must be solved. This calculation is typically performed using the so-called four flux method [101], [103]. In section 4.3, we present a modified version of this method.

While the focused Lambertian model described above offers improvements over the Lambertian scattering model, neither is able to reproduce the scattering profile of real dielectric scatterers (Fig. 4.1). The Lambertian distribution is often used because it leads to simple closed form solutions [104], [105] and serves as a common benchmark. Further, the scattering distribution of high quality dielectric scatterers can be very nearly Lambertian when light is incident on the coating from air [97], [107]. However, for real dielectric scatterers attached to the back of an absorbing slab, the scattering profile deviates from the Lambertian distribution because the scattering actually occurs partially outside of the absorbing slab. This situation also implies that there is a critical angle beyond which scattering cannot occur, which leads to the focused Lambertian model (Fig. 4.1b). This model assumes that the light is impinging on the absorbing slab from a material of refractive index n_b . In reality, a fraction of the light will be impinging on the absorbing

material directly from the scattering particles (see, for example, the inset in Fig. 4.2a), which have an index of refraction that is different from n_b . Although only a small fraction of the absorber's surface is touching the scattering particles, it can have a large impact on the total absorption because light incident on the absorber from the high index scatterer will have longer path lengths on average, which are more likely to lead to absorption [72]. Figure 4.2 compares the absorption resulting from both a Lambertian scattering model and a focused Lambertian scattering model to experimental results (absorption is directly measured with an integrating sphere; details in section 4.3) from a GaP slab with barium sulfate scattering particles attached to the backside to illustrate the importance of accounting for the scattering into these larger angles. Here the Lambertian distribution greatly overestimates the actual absorption while the focused Lambertian greatly underestimates the actual absorption. It should be noted that the focused Lambertian may be modified by using n_b as a fitting parameter to describe an effective index; however, our goal is to accurately predict the measured absorption a priori. Furthermore, if n_b is used as a fitting parameter, different values of n_b may be obtained for different absorber/substrate configurations, offering minimal physical insight into the scattering and absorption phenomena.

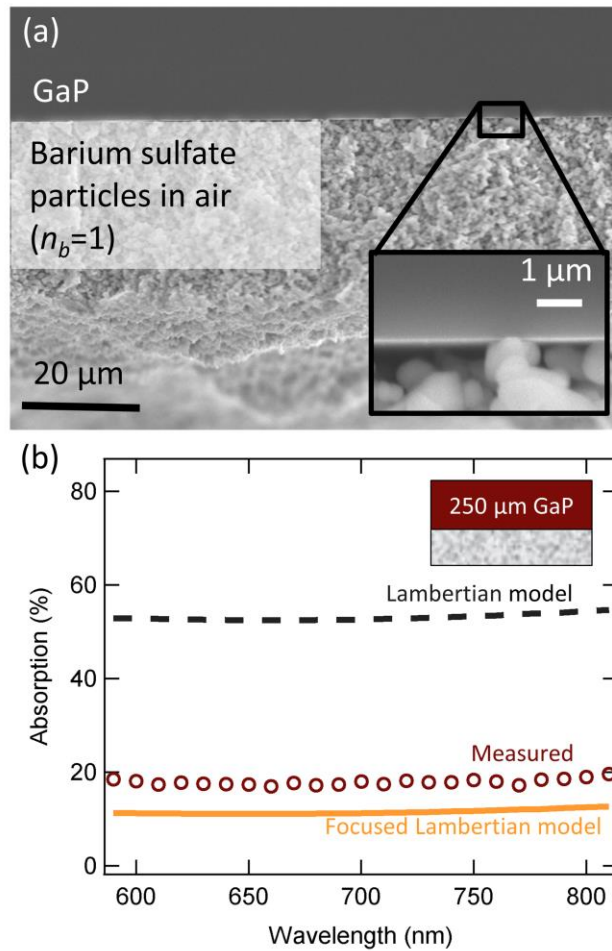


Figure 4.2: Absorption in a GaP slab with barium sulfate scattering particles. (a) SEM cross section of the GaP absorbing slab and a thin layer of barium sulfate scattering particles (actual samples have scattering layers with thickness on the order of a millimeter). Inset shows that a majority of the GaP surface is in contact with air, while a small fraction of the surface is in contact with the high index barium sulfate particles. (b) Calculated and measured absorption in a 250 μm slab of GaP with weak, but not insignificant, absorption beyond the bandgap (550 nm) for the sample shown in (a). The calculations are shown for either a Lambertian or a focused Lambertian (with $n_b = 1$) scattering distribution at the rear of the slab. Both models are in poor agreement with experimental data.

4.3. Measurement of the scattering profile within a material

There are several common approaches to measuring angularly resolved reflection from a scattering surface. The simplest method is to deposit the scattering material on a substrate and illuminate the air/scatterer interface. The scattering distribution is then obtained by measuring the scattered light as a function of angle. This measurement can accurately describe light reflected at the interface of the scattering surface and the air; however, it does not provide information about how light would scatter into an absorbing slab placed on top of the scattering surface. The scattering of light into an absorbing slab is different than the scattering into free-space. If the same technique were applied to an absorbing slab with a back scatterer, the measured scattering distribution would only detect the radiation modes (*i.e.* light that exits the slab through the critical angle, $\theta_c = \arcsin(1/n_{abs})$) and would neglect the trapped modes (*i.e.* modes that correspond to ray-optic paths that lay outside of the critical angle), as demonstrated in Fig. 4.3a. Because only light within the critical angle of the slab can escape, no information is obtained by the photo-detector about light that was scattered into larger angles. A simple solution is to replace the slab

with a hemisphere that allows for all scattered angles to exit the material and be collected by the detector (Fig. 4.3b). The two main limitations of this experimental method are that (i) a hemisphere with low absorption is required for the index of refraction and wavelength of interest, and (ii) the scattering layer should not generate significant surface waves, because they will not propagate to the far field and will thus not be detected.

To completely characterize the scattering distribution, detection of all scattered light is required. This can be accomplished with the use of a hemispheric lens (Fig. 4.3b). The minimum hemisphere radius required to ensure sampling of all scattering angles is:

$$R > rn \tag{4.6}$$

where R is the radius of the half sphere and r is the radius of the illuminated spot size [108]. However, in practice R should be significantly larger than the product rn to avoid lensing effects. In the ideal case, multiple scattering events would be eliminated with an appropriate anti-reflection coating.

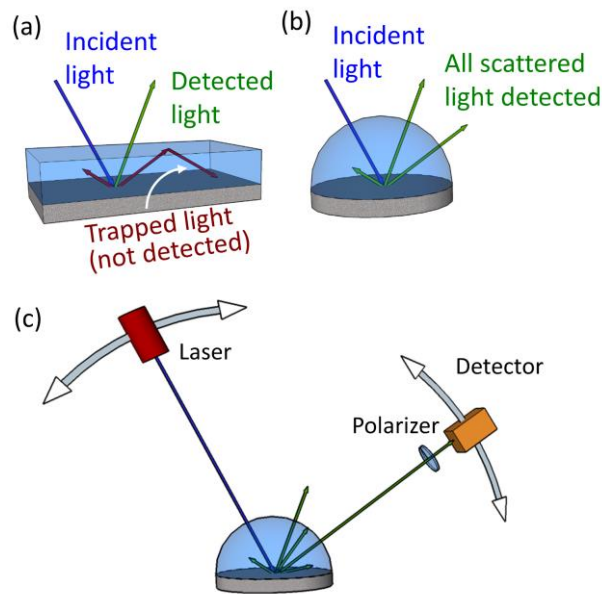


Figure 4.3: Schematic showing the collection of scattered light (a ray optics configuration is shown for simplicity). (a) A slab with a scattering medium adhered to the back. Some scattered rays are not detected as a result of light trapping. Similarly, the maximum angle of incidence on the rear reflector is limited to the critical angle. (b) A hemisphere with a scattering medium on the back surface. All incidence angles are accessible and all scattered angles can be detected. (c) Schematic of the gonioreflectometer measurement setup used in our experiments.

Scattering measurements are made using a custom gonioreflectometer with sample illumination by a HeNe laser (Fig. 3c). For a given laser beam polarization, the detector is rotated about the sample and the signal is measured by a silicon photodiode using a Keithley 2400 Sourcemeter. A polarizer is placed in front of the detector and is either aligned or anti-aligned

with the laser to separate diffuse and specular reflection/scattering. The polarizing filter, has an extinction ratio of $\sim 10,000$. When the specular intensity per unit solid angle is less than 10,000 times the diffuse intensity per unit solid angle, the specular portion is effectively removed by the polarizer. This condition holds true for most of the data of interest but is easily violated when very little scattering occurs such as when the angle of the incident light exceeds the critical angle between the glass/scatterer (see further discussion below). Measurements are made for both polarizations and are similar in all scattering measurements. Samples are prepared by depositing scattering materials onto BK7 ($n = 1.51$) or S-LAH79 ($n = 2.0$) glass hemispheres. The scattering coatings were prepared using a commercially available barium sulfate micro-particle solution (Avian B) per the manufacturer's instructions. These coatings were made ~ 1 mm thick to eliminate transmission. Particle size, determined by SEM (see Fig. 2a), was found to range from 100s of nanometers to a few microns.

Measurements of optical scattering by white paint (randomly packed barium sulfate particles) at the air/paint interface show equal scattering in all directions and is well described as a Lambertian scattering material (Fig. 4a). When this same diffuse reflector is applied to the back interface of a BK7 glass hemisphere, the measured angular distribution is significantly different. Specifically, less light is scattered at large angles, which results in insufficient

light trapping and hence reduced absorption compared to what would have been predicted based on a Lambertian scattering profile.

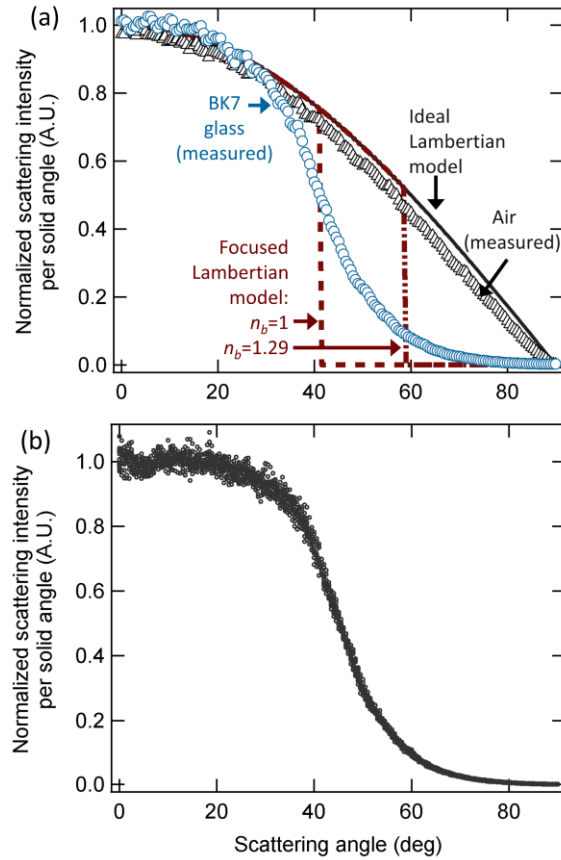


Figure 4.4: Internal scattering distributions. (a) Measured scattering intensity for illumination at 10° incidence at the interface of barium sulfate scatterers and air (triangles) or BK7 glass (circles) compared to the ideal Lambertian scattering model (solid line) and the focused Lambertian model (dashed lines), for laser illumination at $\lambda = 633$ nm (HeNe laser). Shown also are the calculated focused Lambertian distributions with an effective index of either 1 (air) or 1.29 (the effective index which produces the closest fit to the absorption data in Fig. 4.2b). (b) Overlapping measured scattering distributions for incident illumination from 5-35 degrees. The close overlap between these traces demonstrates full randomization in the scattering material.

In order to better understand the scattering produced by the white paint when the interface is not air, we measure and analyze the scattering distribution for two different glass hemispheres (BK7 and LAH79) as a function of incident illumination angle (Fig. 4.5a). Light is scattered efficiently up to an effective critical angle ($\sim 42^\circ$ in BK7 and $\sim 30^\circ$ in S-LAH79), beyond which a reduced amount of scattering extends to nearly 90° (Fig. 4.5b). Scattering into a high index hemisphere (S-LAH79 with $n = 2.0$) has many of the same general features demonstrated with the low index hemisphere (BK7 with $n = 1.51$), but there is a much smaller critical angle (~ 30 degrees) due to the increased refractive index contrast between the hemisphere and the scattering material. In addition, while the scattering in the BK7 hemispheres extends to nearly 90° , the scattering into the S-LAH79 glass approaches zero much more quickly. (Note that the scattering distribution appears to narrow in Fig. 5a beyond the critical angle mentioned above (~ 42 degrees). This apparent narrowing is simply due to the finite extinction ratio of the polarizer (the specular reflection becomes very large) and is not due to an increase in the diffuse scattering.)

A focused Lambertian model would predict the observance of a critical angle defined by the effective index of the scatterer and the glass hemisphere, but not the extended tail shown in Fig. 4.4a for any effective index. In fact if an

effective index is used to fit the data from Fig. 2b (found to be 1.29 for a best fit to the absorption data) the resultant focused Lambertian distribution (shown in Fig 4.4a) poorly matches the scattering data. A possible explanation for the observed scattering distribution is that the light entering the scatterer is not fully randomized. However, Fig. 4b, plots overlapping normalized scattering distributions for incident illumination angles from 5-35 degrees. If light were not randomized within the scattering layer, the resulting scattering profile would depend on the incident angle. Instead the scattering is nearly independent of incident angle, having a relative standard deviation of less 4% over this angular range. We thus posit that the measured data is best described by an ensemble or mixture of effective indices at the dielectric/scatterer interface. This interpretation is also suggested by the SEM images in Fig. 4.2. While much of the interface on the microscopic scale is occupied by interstitial air, some areas are contacted by the barium sulfate particles directly. This heterogeneity leads to variety of effective indices of the scattering material and each index allows for scattering into a subset of angles in the dielectric half sphere.

To test this hypothesis, we first calculate what this index ensemble would be in order to correctly describe the scattering into the BK7. Here we allow the effective index to be randomly chosen from a generating function

bounded by 1 (index of air) and 1.63 (index barium sulfate). The resultant scattering distribution given in units of intensity per unit solid angle is:

$$I(\theta) = I_0 \cos(\theta) \langle T(\theta, n_{eff}, n_{abs}) P(n_{eff}) \left(\frac{n_{abs}}{n_{eff}} \right)^2 \rangle_{n_{eff}} \quad (4.7)$$

where, θ refers to the angle from normal inside the dielectric, n_{eff} is the effective index ensemble of the scattering material, $T(\theta, n_{eff}, n_{abs})$ is the transmission coefficient into the dielectric, $P(n_{eff})$ is the probability of scattering from a given effective index and $\langle \rangle_{n_{eff}}$ indicates the average over the ensemble. The fit is determined by minimizing the root mean squared (RMS) error between the measured scattering data and $I(\theta)$. Note that the scattering intensity defined above is valid under the assumptions that the scattering layer completely randomizes the light, does not contribute significantly to the absorption, and the scatterer has a negligible imaginary part of the refractive index. Thus, the model is independent of the size (microscale or macroscale) of the individual index domains, so long as the light is randomized. The scattering may also be wavelength dependent due to particle size or dispersion in the refractive index of the materials; however, both of these effects are accounted for by a wavelength dependent transmission coefficient and scattering probability. For cases where the index contrast between the particles and the

surrounding medium is low or the particles are large, thicker films may be necessary to ensure randomization.

Once the index ensemble is determined from the measured scattering into the BK7 half sphere, as described above, the model is compared to the measured data obtained using a S-LAH79 hemisphere, which has a different index of refraction. Figure 4.5b compares the measured data to this model. The index ensemble model is in good agreement with the measured result correctly predicting the sharp roll-off at the air/glass critical angle (30 degrees), the extended tail, and the lack of scattering beyond the air/barium sulfate critical angle (~55 degrees). This agreement strongly suggests that the index ensemble interpretation can be used to accurately model the scattering. Further, the agreement of our model with measured data from a hemisphere with a different index of refraction supports the interpretation of the index ensemble model as a physically meaningful description of the scattering layer. To ensure the most accurate index ensemble model, the measured intensity data should be obtained using a hemisphere whose index of refraction is equal to or larger than the maximum index used in the model ($n = 1.63$ in our case). However, this requirement is often not necessary, as the model obtained from the BK7 ($n = 1.51$) hemisphere scattering profile was able to accurately describe the

scattering within the S-LAH79 material ($n = 2.0$). In the next section, this conclusion is tested further with a greater range of structures.

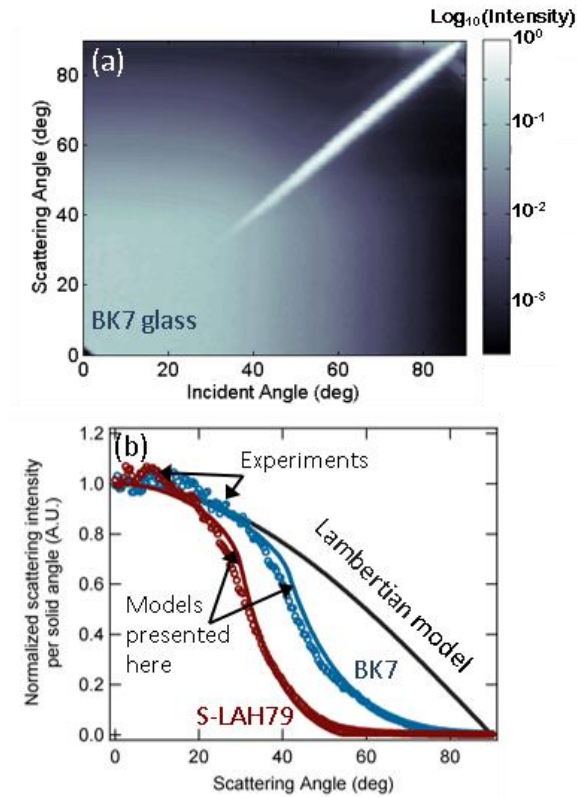


Figure 4.5: Normalized scattering intensity measurements (log scale) using a BK7 glass hemisphere. (b) The scattering intensity for an input angle of 10 degrees shows that our model agrees well with the experimental data for both BK7 and S-LAH79 samples. Here the model was fit for the BK7 sample and confirmed by the measurement using the S-LAH79 sample.

4.3. Measured and calculated absorption

To further validate this model and demonstrate its utility, we make absorption measurements for a variety of samples with random barium sulfate nanoparticle back reflectors. These measurements are made using an integrating sphere (Labsphere RTC-060) with incident illumination at 13 degrees from normal. Samples are placed in the center of the sphere and are directly illuminated. This technique allows for a direct measurement of absorption by simultaneously collecting all reflected and transmitted light (both direct and scattered) and subtracting it from the total incident light. Second order diffuse absorption in the sample (light reflected from the sample then absorbed after scattering from the wall of sphere) is corrected for by measuring diffuse absorption through a secondary port. ITO is used as a low index absorber, GaP as a high index absorber, and glass as a minimally absorbing substrate. Measurements of samples using a GaP substrate are made at wavelengths greater than the bandgap of GaP to avoid complete absorption in the GaP prior to scattering off the back reflector. Measurements for ITO on glass are made at shorter wavelengths to ensure sufficient absorption (ITO absorption typically peaks in the near UV). Film thicknesses are measured by AFM (Asylum Research, Cypher) and confirmed by ellipsometry (J.A. Woollam M-2000D). The refractive index of the films and substrates are

measured by ellipsometry. We note that ellipsometry cannot accurately determine the very small imaginary parts of the refractive index for glass and GaP samples. These small values ($10^{-6} - 10^{-8}$) are calculated based on separate absorption measurements of those materials alone (no back-scatterers) using the integrating sphere setup. The dielectric scatterers are applied to the absorbers in the same manner as in the scattering measurements. The absorption loss per reflection of the scattering layer is characterized by absorption measurements with illumination on the air/scattering interface. Note that the transmission through these scattering layers is found to be much less than 1% so that any reflection less than unity can be attributed to absorption in the scattering layer.

Absorption measurements for the full structures (scattering material on film/substrate) are compared to the calculated absorption based on the index ensemble model. Absorption is calculated by a modified version of the four flux method following Cotter [103]. Here, based on the measurements shown in Fig. 4b, we assume that all light entering the scattering material is completely randomized. Thus, in contrast to the typical implementation of the four-flux method, the fraction of light scattered (not specular reflection) at the absorber/scatterer interface is simply determined by Fresnel coefficients (using an index ensemble). All transmission and reflection coefficients are calculated

by the matrix transfer method including coherent (thin films) and incoherent (thick substrates) reflections/transmissions following Katsidis and Siapkas [109]. All such coefficients were found for light passing through the entire film/substrate stack. Thus, the multiple reflections inside of the film/substrate are automatically accounted for using this method. The total absorption is calculated as the fraction of light that does not escape from the front surface of the sample and is given by:

$$A = 1 - \langle P(n_{eff})R_{dir,in} \rangle_{neff,s/p} - \frac{\rho_{int} \langle P(n_{eff})T_{dir,in} \rangle_{neff,s/p} \langle P(n_{eff})T_{diff,out} \rangle_{neff,s/p}}{1 - \rho_{int} \langle P(n_{eff})R_{diff,out} \rangle_{neff,s/p}} \quad (4.8)$$

where, $\langle \rangle_{neff,s/p}$ denotes averaging over the index ensemble (as determined from the scattering data) and both polarizations (note: while we assume the polarization is randomized by the scattering, the transmission and reflection coefficients are still polarization dependent). ρ_{int} is the absorption loss per reflection of the scattering material itself. $R_{dir,in}$ ($T_{dir,in}$) is the reflection (transmission) coefficient of direct illumination passing through the sample to the scatterer. $R_{diff,out}$ ($T_{diff,out}$) is the total integrated diffuse reflection (transmission) coefficient for light traveling from the scatterer through the sample to air. These values can be calculated from the angularly dependent reflection (transmission) coefficient, $R_{out}(\theta)$ ($T_{out}(\theta)$), by:

$$R_{\text{diff,out}} = 2 \int_0^{\pi/2} R_{\text{out}}(\theta_{\text{scat}}) \cos(\theta_{\text{scat}}) \sin(\theta_{\text{scat}}) d\theta_{\text{scat}} \quad (4.9)$$

Here θ_{scat} is the angle from the normal in the scattering material (not the angle of the light escaping the surface). Note that determining the effective index ensemble is critical for our calculation in two ways. First, it allows for accurate modeling of the scattering profile. Second, it allows for calculation of the appropriate Fresnel coefficients. As a result, the increase in absorption due to light trapping can be fully modeled, even in thin-films.

Figure 4.6a-c shows that the measured absorption is well described by the ensemble model. For all of the measurements, the models have an RMS error of <1.5% (with 0.9%, 1.4% and 1.4% for the GaP (4.6a), the dual-layer GaP/ITO (4.6b) and the dual-layer Glass/ITO (4.6c) samples, respectively). We attribute the greater error in the ITO samples to the large variability in ITO index, resulting in less accurate fits to the ellipsometry data. In all cases the Lambertian model greatly overestimates the absorption and the focused Lambertian greatly underestimates the absorption. These results demonstrate the utility and versatility of the index ensemble model and further support our interpretation of the underlying physics.

These measurements also illustrate some important points about scattering and absorption in general. First note that there is significant absorption in the

GaP (6a) sample despite the miniscule intrinsic absorptivity of this material (in this wavelength range). This absorption is primarily due to the high refractive index of the GaP. The large index results in high reflection for light attempting to escape the GaP (increased path length) and in high reflection for light entering the GaP from the scatterer (high loss in the scatterer; $\sim 1/3$ the total loss in this case). Also note the relatively small difference in absorption measured for the GaP and GaP/ITO samples despite the addition of the much more absorptive ITO in the later. In this case, the ITO layer reduces the index contrast between the scattering layer and the GaP. This reduced index contrast results in only $\sim 1/6$ of the loss occurring in the scattering material. Continuing with the comparison between the GaP and GaP/ITO samples, notice the large difference in the predicted Lambertian absorption for the GaP and GaP/ITO. Lambertian scattering is defined by complete randomization in the material into which the scattering occurs; either GaP or ITO in these examples. For the GaP/ITO sample, light is scattered in a full 2π steradians in the low index ITO but this is reduced to a critical angle inside the GaP. This reduction in angle results in a much shorter average path length in the GaP and less trapped light. In contrast, for the sample with GaP alone, light is scattered in a full 2π steradians in the high index GaP resulting in a longer average path length and a greater fraction of trapped light. Lastly, note the large absorption in the

Glass/ITO sample compared to the GaP/ITO sample, despite a thicker ITO layer on the GaP/ITO sample. This effect is simply due to greater intrinsic absorptivity of the ITO at short wavelengths.

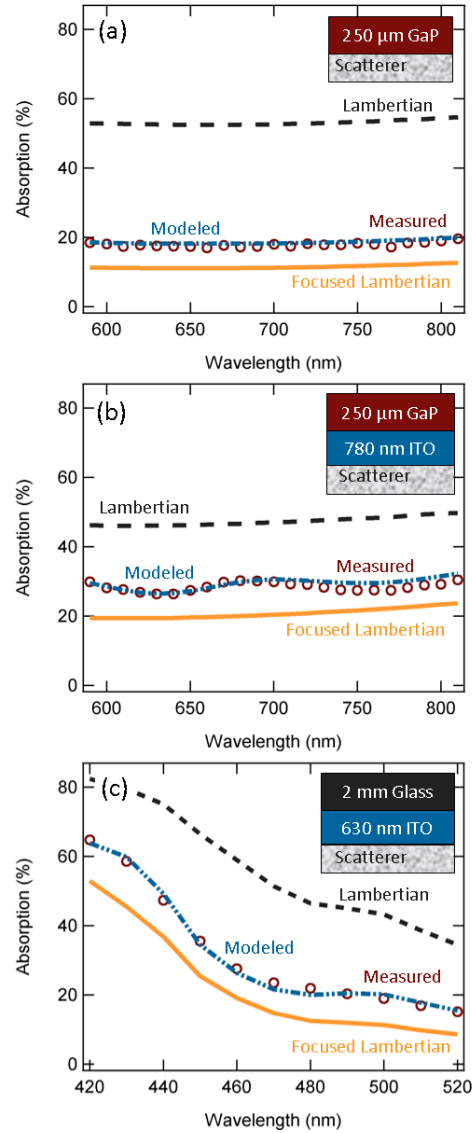


Figure 4.6: Comparison of modeled and measured absorption. (a) Same data as Fig. 4.2(b) including the scattering modeled using the index ensemble model. The RMS error between measurement and calculation is 0.9% (b) An interstitial ITO layer is added to manipulate the scattering rate and increase the absorption. Here the RMS error is 1.0%. Note the reduced absorption for the Lambertian model is due to the lower index ITO. The lower index material limits the scattering angles in the GaP. (c) The GaP substrate is replaced with glass so that the ITO is the main absorber. In this case, the RMS error is 1.4%. These results demonstrate the accuracy of this method over a wide range of absorption conditions.

4.4. Discussion

In this chapter we have demonstrated an accurate method for measuring scattering from random dielectric nanoparticles. This technique was required to evaluate the scattering into guided modes of planar structures, which would normally be inaccessible. This method was further motivated by large discrepancies between measured absorption and predictions based on typical light trapping theories for dielectric scatterers (*i.e.* the Lambertian and focused Lambertian models). We found that the measured scattering distribution could not be explained by the typical focused Lambertian distribution despite the fact that angle-integrated absorption data could be fit using this model. We instead proposed that the underlying cause of this distribution was the scattering from an ensemble of indices. We found that by using this model, we could accurately explain our new scattering data and precisely predict the measured absorption data.

This work has several broader implications. First, we note that this technique for the measurement of scattering distributions is not limited to dielectric scatterers. In fact, as long as near field scattering and surface modes do not play a major role, and as long as an appropriate weakly absorbing hemisphere is available for the wavelength and index range of interest, this technique can be implemented to fully characterize any scattering surface

including textured surfaces or gratings by applying these structures to a suitable hemisphere. Near field scattering (including evanescent fields from surface modes) will contribute to absorption but, by definition, cannot be detected directly in the far field, and thus this scattering is outside the reach of measurements using this method. While surface modes may still refract into free-space at the edge of the hemisphere, the experiment presented here is not designed to distinguish these rays. These techniques are completely agnostic to the nature of the scattering object (size, shape, origin) all that is required is that the hemisphere can support all the wave vectors (modes) available to the scatterer. Secondly, our model demonstrates the need for careful consideration of the interface between the scattering material and absorber. Even if the remainder of the scattering layer has a lower packing fraction, significant gains can be achieved by ensuring a high effective index profile near the surface.

Chapter 5: A generalized approach to modeling absorption with light scattering structures

Understanding where absorption takes place within an optoelectronic device (*e.g.* a solar cell or photodetector) is essential to evaluating its performance. Absorption in the active layers leads to carrier generation, while absorption outside of those regions represents energy loss. While the total absorption may be of interest, knowing the location of absorption allows researchers to properly evaluate trade-offs and optimize device efficiency. For simple, non-scattering stratified structures, this calculation is either performed directly by finding the electromagnetic field throughout the individual layers [110], [111] or by finding the total absorption and neglecting less absorptive layers. When scattering structures are introduced, these calculations can be more difficult. If these structures contain only coherent scatterers such as gratings or periodic arrays of particles, the absorption in each layer can be found by calculating the fields using rigorous coupled-mode theory [102], [112], finite element simulations [113], [114] or, in some cases, analytic expressions [115], [116]. However, when scattering occurs from non-periodic (random) configurations, these techniques are no longer applicable. In these

cases, calculating absorption in individual layers requires either aggregates of randomized sub-simulations [100] (*e.g.* Monte Carlo techniques), simplifying assumptions (*e.g.* no absorption in all other layers), or using analytic expressions for the limit of absorption assuming ideal randomization of the light and/or optimal mode coupling [10], [59], [61], [105], [116], [117].

In this chapter we present analytic expressions for absorption in individual layers of arbitrary stratified planar media (having any combination of thin coherent films and thick incoherent slabs) containing randomizing scattering structures. We focus our discussion on structures with planar scattering layers that completely randomize the light in that layer. The framework is most directly applicable to layers of dielectric scatterers, as we will use the effective refractive index ensemble model [118], and will be limited to weakly absorbing scattering layers (no such constraints are placed on other layers). However, the equations are completely agnostic toward the nature of the scattering (*i.e.* how the scattering is achieved) and only require that it can be described by parameters that can be determined experimentally. We then give examples of how to implement these models in several special cases. We show how this model can be used to describe a variety of interesting structures and compare two examples to experimental measurements.

5.1. Calculating total absorption

Total absorption, reflection, and transmission in the absence of scattering can be calculated by Fresnel coefficients using the matrix transfer method with coherent reflection/transmission (at thin-film interfaces) and incoherent reflection/transmission (at interfaces with thick layers such as a glass substrate or a bulk material) following Katsidis and Siapkas [109]. This well-known method calculates the coefficients in two steps. First, field transfer matrices are used to calculate the intensity of reflection/transmission between incoherent layers (or to outside the stack). Second, intensity transfer matrices are used to calculate the total reflection/transmission. Partial coherence may also be introduced by simple modifications to field transfer matrices [109], [119]. When a scattering layer is present, the total absorption, reflection, and transmission can similarly be determined depending on the nature of the scattering [97], [100], [102], [103], [118], [120], [121]. To account for planar structures with an arbitrary combination of layers, some knowledge of the scattering material is required in order to accurately model the fraction of light that enters or exits the scattering layer. When the light entering the scattering structure becomes completely randomized before returning to one of the two interfaces, only a few parameters are needed to describe the scattering layer (note that randomization does not mean that this layer creates a Lambertian

scattering distribution, but that light inside this layer has constant power per solid angle; see below and Ref [118] for further discussion). We previously showed that in this randomizing regime, the only parameters necessary to accurately describe light propagation in this layer are the experimentally measurable values of internal loss, transmission, and the ensemble of effective indices present at the interfaces of the scattering layer [118]. Here we use the effective index ensemble model because it physically describes many cases of interest, it gives insight into the nature of random scattering, and because its generality allows for modeling of a wide variety of scattering structures. This ensemble may be approximated by a single index, producing a Lambertian or focused Lambertian scattering distribution, but in general results in a scattered intensity per solid angle of:

$$I(\theta) = I_0 \cos(\theta) \langle T(\theta, n_{\text{eff}}, n) P(n_{\text{eff}}) \left(\frac{n}{n_{\text{eff}}} \right)^2 \rangle_{n_{\text{eff}}} \quad (5.1)$$

where n is the index of refraction for the material into which the scattering occurs, θ is the angle from surface normal inside the material into which the scattering occurs, n_{eff} is the effective index of the scattering layer, $T(\theta, n_{\text{eff}}, n)$ is the transmission coefficient for light exiting the scattering layer, $P(n_{\text{eff}})$ is the

probability of scattering from a given effective index (note that this function is what defines the ensemble and is, in general, a continuous function), and $\langle \rangle_{n_{\text{eff}}}$ indicates the average over the ensemble of indices. Eq. 5.1 follows directly from our definition of random (constant power at each solid angle). Note that when $Im\{n_{\text{eff}}\}$ is non-negligible, *i.e.* when the condition $Im\{n_{\text{eff}}\}/Re\{n_{\text{eff}}\} \ll 1$ fails, angles become complex and lose the simple meaning they had in our definition of random and in Eq. 5.1. In this case, randomization must be understood in the more general sense of equally filling all modes. Our discussion is limited to weakly absorbing scattering layers (other layers are not restricted in this way), which covers most cases of interest. However, Tables 5.1 and 5.2 show special case, including the addition of absorbing scatterers.

With scattering specified as above, we can calculate the total reflection, transmission, and absorption for the general scattering structure shown in Fig. 5.1. A scattering layer (s') is sandwiched between an arbitrary set of incoherent layers (denoted by primed letters ranging from a' to b') and coherent layers (unprimed letters from a to b). This structure contains incoherent layers interlaced with arbitrary sets of coherent layers. In general, t and r refer to field transmission and reflection coefficients and T and R refer to intensity coefficients. Subscripts will denote the origin and endpoint layers for light in

the calculation of a given coefficient with no propagation beyond the origin and endpoint. For example, $T_{a' b'}$ is be the transmitted intensity for light originating just inside layer a' at the interface nearest layer b' and ending just inside layer b' at the interface nearest layer a' . Note that in the presence of absorbing layers some typical identities for these coefficients no longer apply (e.g., $R_{a' b'} \neq R_{b' a'}$) so subscript ordering should be carefully noted. Under this scheme, the general scattering distribution described above results in total structure reflection, transmission, and absorption given by:

$$R_{a' b'} = \langle R_{a' s'} \rangle + \frac{\langle T_{a' s'} \rangle \langle T_{\text{diff}, s' a'} \rangle \langle R_{\text{scat}} \rangle}{1 - \langle R_{\text{diff}, s' a'} \rangle \langle R_{\text{scat}} \rangle}, \quad (5.2a)$$

$$T_{a' b'} = \frac{\langle T_{a' s'} \rangle \langle T_{\text{scat}} \rangle}{1 - \langle R_{\text{diff}, s' a'} \rangle \langle R_{\text{scat}} \rangle}, \quad (5.2b)$$

and

$$A_{a' b'} = 1 - R_{a' b'} - T_{a' b'}, \quad (5.2c)$$

respectively, where

$$\langle R_{\text{scat}} \rangle = (1 - \tau_{\text{int}}) \rho_{\text{int}} + \frac{(\tau_{\text{int}} \rho_{\text{int}})^2 \langle R_{\text{diff}, s' b'} \rangle}{1 - (1 - \tau_{\text{int}}) \rho_{\text{int}} \langle R_{\text{diff}, s' b'} \rangle}, \quad (5.2d)$$

and

$$\langle T_{\text{scat}} \rangle = \frac{\tau_{\text{int}} \rho_{\text{int}} \langle T_{\text{diff},s' b'} \rangle}{1 - (1 - \tau_{\text{int}}) \rho_{\text{int}} \langle R_{\text{diff},s' b'} \rangle}, \quad (5.2e)$$

and $\langle \ \rangle$ denotes averaging over the effective index ensemble and over both polarizations (note that while we assume the polarization is lost inside the scattering layer, Fresnel coefficients are still polarization dependent). ρ_{int} and τ_{int} are two parameters that characterize the scattering layer and can be determined experimentally. ρ_{int} is the sum of the reflected light and transmitted light intensities ($\rho_{\text{int}} = R + T$), and τ_{int} is the ratio of the transmitted intensity to ρ_{int} , *i.e.* $\tau_{\text{int}} = \frac{T}{\rho_{\text{int}}} = \frac{T}{R+T}$. Thus $\rho_{\text{int}} \tau_{\text{int}}$ is the fraction of light transmitted from one side of the scatterer to the other and $\rho_{\text{int}}(1 - \tau_{\text{int}})$ is the fraction reflected back. $R_{a's'}$ and $T_{a's'}$ are the fractions of direct illumination reflection and transmission, respectively, corresponding to light passing through all layers a' to s' . $R_{\text{diff},s'a'}$ and $T_{\text{diff},s'a'}$ ($R_{\text{diff},s'b'}$ and $T_{\text{diff},s'b'}$) are the total integrated diffuse reflection and transmission for light traveling from the scatterer to outside the front (back) surface. These values can be calculated from the angularly dependent reflection and transmission. For instance, the diffuse reflection for light leaving the scattering layer and travelling out through the front of the structure is given by:

$$R_{\text{diff},s'a'} = 2 \int_0^{\pi/2} R_{s'a'}(\theta_{s'}) \cos(\theta_{s'}) \sin(\theta_{s'}) d\theta_{s'} \quad (5.3a)$$

$\theta_{s'}$ is the angle from the normal in the scattering layer (not the angle of the light escaping the surface). Lastly, direct illumination is not a requirement of the model and diffuse illumination can be implemented by changing $R_{a's'}$ and $T_{a's'}$ in Eq.'s 5.2a and 5.2b to their diffuse counterparts, $R_{\text{diff},a's'}$, and $T_{\text{diff},a's'}$. As an example (in direct analogy to Eq. 5.3a), the diffuse reflection resulting from diffuse illumination is:

$$R_{\text{diff},a's'} = 2 \int_0^{\pi/2} R_{a's'}(\theta_{a'}) \cos(\theta_{a'}) \sin(\theta_{a'}) d\theta_{a'} \quad (5.3b)$$

where $\theta_{a'}$ is the incident angle in the front semi-infinite space (Fig. 5.1).

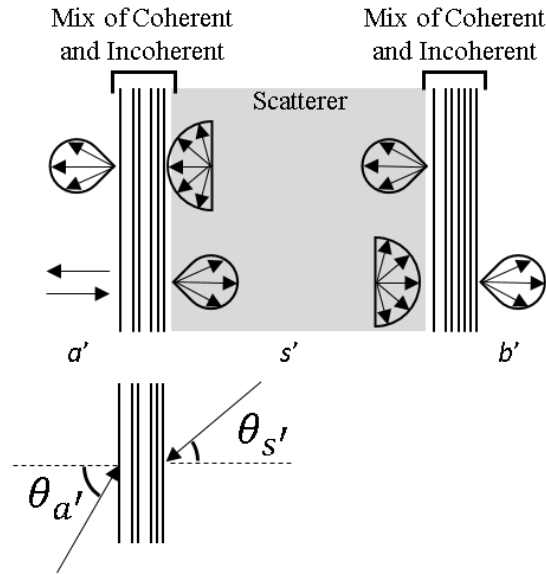


Figure 5.1: Schematic of structure containing a scattering layer. It consists of a scattering layer surrounded by arbitrary combinations of coherent and incoherent layers. Incoherent layers

are enumerated a' to b' . The scattering layer is denoted as the s' th layer. Light that enters the scattering layer is fully randomized before returning to either interface of this layer.

5.2. Calculating absorption in individual layers

In this section we demonstrate how to calculate the absorption in individual layers of stratified media containing scattering layers by working through levels of abstraction up to the full scattering structure shown in Fig. 5.1. We first consider a stack of coherent layers and determine the absorption in individual layers. Second, we consider how this absorption is modified when this stack of coherent layers is part of a larger structure containing both coherent and incoherent layers and determine the absorption in a single incoherent layer for this case. Finally, we use our result to calculate the absorption in an each layer (coherent or incoherent) of the full structure (containing coherent, incoherent, and scattering layers) shown in Fig. 5.1.

Before proceeding to the calculation, some additional discussion on notation is needed. In general, a single subscript denotes the layer corresponding to that parameter (*e.g.*, n_j is the refractive index of the j^{th} layer). Absorption coefficients that use one subscript denote single pass absorption within that incoherent layer (starting just inside the layer on one side to just inside the same layer at the opposite surface). Three subscripts will be used for

absorption in multilayers - indicating the layer in which the light originates, the layer in which absorption is calculated, and the endpoint layer, respectively. Furthermore, the propagation direction will be specified by a relative parallel (to the surface) k -vector, $q = k_{\parallel}/k_0$ where $k_{\parallel} = nk_0 \sin \theta$ (note that this value, q , is constant in all layers in the absence of scattering). If there is no absorption, θ has its usual meaning, the angle from normal in a material of refractive index n . However, within dispersive structures θ is in general complex. Also note that, as done above, we eschew the typical matrix notation and instead opt for explicit equations because the former does not reduce notation or increase clarity due to the large number of unique named variables (see Table 5.3 for a complete list of variables and constants).

Figure 5.2 shows a schematic of the electric field components propagating forward (+) and backward (-) in a stack of coherent layers, enumerated from a to b . The inset of this figure shows the field components in the j^{th} layer. The absorption in a given coherent layer (defined as the intensity loss in that layer as light travels through the entire coherent stack), for a given propagation direction, is calculated following Pettersson *et al.* [110] and Centurioni [111]. To find the absorption in a given layer, we calculate the energy density in that layer, which is proportional to absorption. Absorption in the j^{th} layer of a single stack of coherent layers due to light originating just

outside of the stack (*i.e.* in the i' th layer) and passing through the entire stack (*i.e.* to the $(i'+1)$ th layer) is given by:

$$\tilde{A}_{i'j(i'+1)}(q) = \int_0^{d_j} \frac{1}{2} \frac{c \varepsilon_0 \alpha_j \text{Re}\{n_j\} \left[|E_{\perp,j}(x, q)|^2 + |E_{\parallel,j}(x, q)|^2 \right] dx}{\text{Re} \left\{ \sqrt{1 - (q/n_{i'})^2} \right\} \text{Re}\{n_{i'}\}}, \quad (5.4a)$$

where the tilde is used to distinguish the absorption in j for a single coherent stack from general case, including incoherent layers, defined below. The fields for TM polarization are given by:

$$E_{\perp,j}(x, q) = [E_j^+(x, q) - E_j^-(x, q)] \frac{q}{n_j} \quad (5.4b)$$

$$= t_{i'j(i'+1)}^+ [e^{iqx} - r_{j(i'+1)} e^{iq(2d_j-x)}] \frac{q}{n_j} \quad (5.4c)$$

and

$$E_{\parallel,j}(x, q) = [E_j^+(x, q) + E_j^-(x, q)] \sqrt{1 - \left(\frac{q}{n_j}\right)^2} \quad (5.4d)$$

$$= t_{i'j(i'+1)}^+ [e^{iqx} + r_{j(i'+1)} e^{iq(2d_j-x)}] \sqrt{1 - \left(\frac{q}{n_j}\right)^2} \quad (5.4e)$$

and for polarization TE:

$$E_{\perp,j}(x, q) = 0 \quad (5.4f)$$

$$E_{\parallel,j}(x, q) = t_{i'j(i'+1)}^+ [e^{iqx} + r_{j(i'+1)} e^{iq(2d_j-x)}] \quad (5.4g)$$

where

$$t_{i'j(i'+1)}^+ = \frac{t_{i'j}}{1 - r_{ji'} r_{j(i'+1)} e^{i2qd_j}} \quad (5.4h)$$

(with assumed polarization and q dependence of Fresnel equations). As shown in Fig. 5.2, E is the normalized electric field with \parallel or \perp denoting the components of the field either perpendicular or parallel to the surface, and + and - superscripts refer to the forward and backward travelling waves, respectively. α_j is the absorption coefficient of the j^{th} layer. d_j is the thickness of the j^{th} layer. $r_{j(i'+1)}$ is the reflection coefficient from the rear of the j^{th} layer through all the layers up to the $(i' + 1)^{\text{th}}$ layer, and $r_{ji'}$ is the reflection coefficient from the j^{th} layer to the i'^{th} layer. $t_{i'j}$ is the transmission coefficient from the i'^{th} layer to the j^{th} layer.

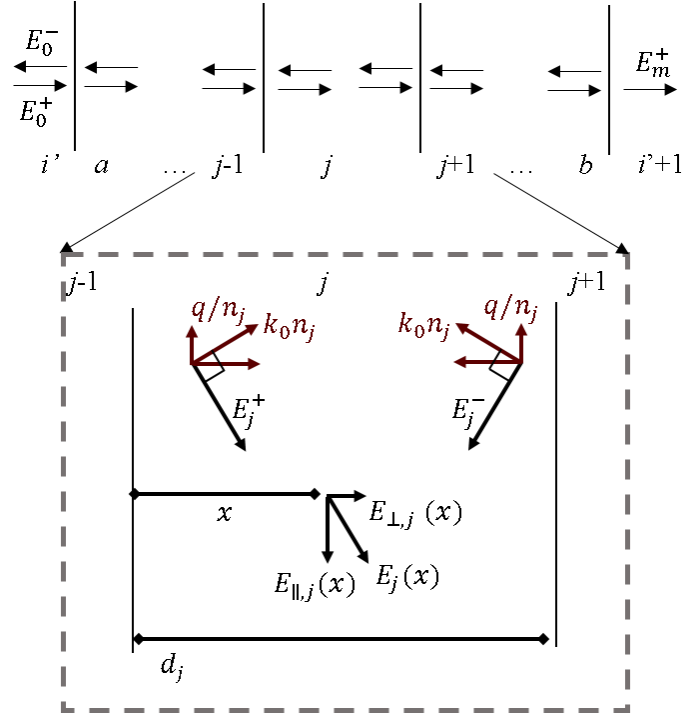


Figure 5.2: Schematic of the electric field components in each layer with numbering notation used to describe stacks of coherent layers. Coherent layers are enumerated a through b , with light originating and ending in semi-infinite spaces labeled i' and $i'+1$. In general, j will be used to denote the coherent layer of interest. The arrows between the layers represent the direction of forward and backward traveling waves. Zoom-in on layer j shows the naming conventions for the fields and k -vectors. The total field consists of forward and backward travelling waves denoted with plus and minus superscripts, respectively. The total field can be decomposed into parallel and perpendicular components (marked by \parallel and \perp subscripts, respectively). x is the distance from the light incidence side (*i.e.*, $\mathbf{x} = \mathbf{0}$ at the boundary of layers $j-1$ and j in this figure).

For a non-scattering structure containing both coherent and incoherent layers, the total absorption in a coherent layer j can be calculated by considering how many times the light passes through the coherent layer stack

containing the j^{th} coherent layer and with what intensity. Here, as depicted in Fig.'s 5.2 and 5.3, we denote the last incoherent layer before the coherent layer stack (containing j) as the i'^{th} layer and the first incoherent layer after the stack as the $(i'+1)^{\text{th}}$ layer. When no scattering is present, the absorption in layer j due to light originating in an incoherent layer, a' , and traveling to an incoherent layer, b' , is given by:

$$A_{a'j b'}(q) = \frac{\mathcal{A}_{i'j b'}(q)T_{a'i'}(1 - A_{i'})}{1 - R_{i'a'}R_{i'b'}(1 - A_{i'})^2}, \quad (5.5a)$$

where

$$\begin{aligned} \mathcal{A}_{i'j b'}(q) = & \tilde{A}_{i'j(i'+1)}(q) \\ & + \frac{\tilde{A}_{(i'+1)j i'}(q)T_{i'(i'+1)}R_{(i'+1)b'}(1 - A_{(i'+1)})^2}{1 - R_{(i'+1)i'}R_{(i'+1)b'}(1 - A_{(i'+1)})^2}, \end{aligned} \quad (5.5b)$$

and $A_{i'}$ and $A_{(i'+1)}$ are the absorption for a single pass through the i'^{th} or $(i' + 1)^{\text{th}}$ layer, respectively (defined in the usual way as $1 - |\exp(i d k_0 \sqrt{n^2 - q^2})|^2$). Again, polarization and q dependence are assumed in all reflection and transmission coefficients. Note that when the a'^{th} layer is also the i'^{th} layer, $T_{a'i'} = 1$, $R_{i'a'} = 0$, and $A_{i'} = 0$. Similarly, when the $(i' + 1)^{\text{th}}$ layer is also the b'^{th} layer, $R_{(i'+1)b'} = 0$, and $A_{(i'+1)} = 0$. Absorption in an incoherent layer is given by similar equations. For example, the absorption in

an arbitrary incoherent layer i' due to light originating in the a' th layer and ending in the b' th layer is given by:

$$A_{a'i'b'}(q) = [1 + (1 - A_{i'})R_{i'b'}] \frac{T_{a'i'}A_{i'}}{1 - R_{i'a'}R_{i'b'}(1 - A_{i'})^2} \quad (5.5c)$$

Finally, we are able to calculate our main result, the absorption in any layer of a planar structure in the presence of a scattering layer. The absorption in the z th layer (here z is used as a dummy variable representing any layer, coherent or otherwise) due to light impinging on the front (a' th layer) of our scattering structure with scattering occurring in the s' th layer can be calculated.

When layer z is before the scattering layer, the absorption in layer z is:

$$A_{a'zb'}^{\text{tot}} = \langle A_{s'za'}(q) \rangle + \frac{\langle T_{a's'} \rangle \langle A_{\text{diff},s'za'} \rangle \langle R_{\text{scat}} \rangle}{1 - \langle R_{\text{diff},s'a'} \rangle \langle R_{\text{scat}} \rangle} \quad (5.6a)$$

where,

$$\langle R_{\text{scat}} \rangle = (1 - \tau_{\text{int}})\rho_{\text{int}} + \frac{(\tau_{\text{int}}\rho_{\text{int}})^2 \langle R_{\text{diff},s'b'} \rangle}{1 - (1 - \tau_{\text{int}})\rho_{\text{int}} \langle R_{\text{diff},s'b'} \rangle} \quad (5.6b)$$

and when layer z is after the scattering layer, the absorption in this layer is:

$$A_{a'zb'}^{\text{tot}} = \frac{\langle A_{\text{diff},s'zb'} \rangle \langle T_{\text{scat}} \rangle}{1 - \langle R_{\text{diff},s'b'} \rangle \langle R_{\text{scat}} \rangle} \quad (5.6c)$$

where,

$$\langle R_{\text{scat}} \rangle = (1 - \tau_{\text{int}})\rho_{\text{int}} + \frac{(\tau_{\text{int}}\rho_{\text{int}})^2 \langle R_{\text{diff},s'a'} \rangle}{1 - (1 - \tau_{\text{int}})\rho_{\text{int}} \langle R_{\text{diff},s'a'} \rangle} \quad (5.6d)$$

and

$$\langle T_{\text{scat}} \rangle = \frac{\tau_{\text{int}}\rho_{\text{int}} \langle T_{a's'} \rangle}{1 - (1 - \tau_{\text{int}})\rho_{\text{int}} \langle R_{\text{diff},s'a'} \rangle} \quad (5.6e)$$

where $A_{\text{diff},s'za'}$ is defined as:

$$A_{\text{diff},s'za'} = 2 \int_0^{\pi/2} A_{s'za'}(n_{s'} \sin(\theta_{s'})) \cos(\theta_{s'}) \sin(\theta_{s'}) d\theta_{s'} \quad (5.6f)$$

with a similar expression for $A_{\text{diff},s'zb'}$.

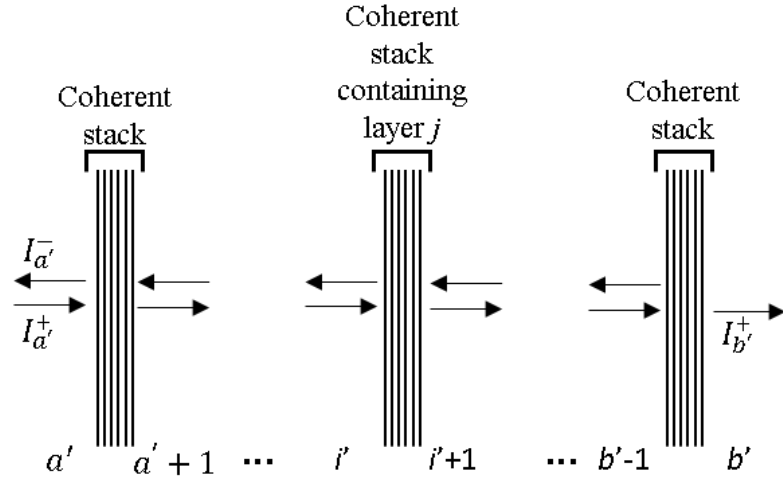


Figure 5.3: Numbering scheme for a generic stack of coherent and incoherent layers. This structure has $b'-1$ incoherent layers between two semi-infinite layers all enumerated as layers a' to b' . Between the incoherent layers are a total of b coherent layers (numbered 1 to b). The stack of coherent layers containing the j^{th} coherent layer is immediately preceded by the i^{th} incoherent layer. In direct analogy to Fig. 5.2, the arrows represent exchange of intensity between the layers. Note that this figure is in no way meant to denote any specific structure or layer ordering.

In the calculations above we have made a few important assumptions. We summarize these assumptions here for clarity. First, we assume, that light passing through the scattering layer becomes completely randomized, so that the scattering does not depend on incident angle (beyond Fresnel coefficients for transmission/reflection into and out of the scattering layer). This condition is required to create analytic algebraic expressions and is met for many scattering structures. If the light is not fully randomized, other methods are required, *e.g.* a Monte Carlo approach [114]. Second, we assumed that the scatterer is weakly absorbing. This condition is required to define random scattering in the usual way as producing equal power per solid angle. When this condition isn't met, random can only be properly defined as filling all optical modes. In Table 5.2 we also consider the use of strongly absorbing scatterers where the scatterers are well separated from the next material interface. Third, we assumed that the interfaces are planar and parallel to a good approximation. Large deviations from this approximation result in additional scattering. However, small deviations from planar and parallel are permitted (in fact, this deviation is one of the sources of incoherence in thick layers). In Table 5.2, we also consider rough surfaces (which act as a type of

scatterer) but under some simplifying assumptions that allow all calculations to be performed as if the structure contained only planar surface.

5.3. Special cases

When scattering structures are discussed there are several special cases that are typically examined which involve ideal layers and interfaces. Table 5.1 shows how various ideal front and back scatterers can be modeled. The first column lists the ideal condition under consideration, the second gives details of this idealization, and the third column gives a schematic view of that situation. The penultimate column describes how to set the parameters of the model to create that aspect, and the final column notes limitations of the described modeling. In this section we consider, ideal front and back scattering layers with additional special cases of potential interest described in Table 5.2.

An ideal back reflector implies that the back reflector is perfectly reflective and/or the back reflector is perfectly scattering (Lambertian). Perfect reflectivity is achieved when there is no transmission ($\rho_{\text{int}}\tau_{\text{int}} = 0$) and no loss within the scatterer ($\rho_{\text{int}} = 1$). Perfect scattering is typically defined as producing a Lambertian intensity distribution:

$$I(\theta) = I_0 \cos(\theta), \quad \text{for } \theta \leq \frac{\pi}{2}. \quad (5.7)$$

In the presence of resonant structures (coherent films) or absorption, this Lambertian scattering becomes poorly defined; however, the effect can be approximated by taking the scattering layer to have the same refractive index as the layer into which it is scattering (having index n):

$$P(n_{\text{eff}}) = \begin{cases} 1 & \text{for } n_{\text{eff}} = \text{Re}\{n\} \\ 0 & \text{else} \end{cases} \quad (5.8)$$

The real part is taken here to maintain our assumption of negligible absorption in the scattering layer. Note that when $\text{Im}\{n\}$ becomes large, the reflection at an interface between two materials with different indices, $\text{Re}\{n\}$ and n respectively, becomes non-zero and is no longer angle independent. In that case, Eq. 5.8 results in a poor approximation. For example, GaAs has an index of $n = 2.72 + 4.26i$ at a wavelength of 250 nm (near an absorption resonance), [122] which would produce a 38% TE reflection at a $\text{Re}\{n\}/n$ interface for normal incidence and 41% for 90° incidence. However, at a wavelength of 550 nm, GaAs has an index of $n = 4.06 + 0.27i$, [122] which would produce a 0.11% reflection at a $\text{Re}\{n\}/n$ interface for normal incidence and 0.12% for 90 degrees incidence.

This same process can be used to model ideal intermediate or top scatterers. To produce Lambertian scattering from any given interface into a medium with index, n , the scatterer must have an effective index given by $\text{Re}\{n\}$. Note that because we describe the internal structure of the scattering layer with only phenomenological constants, τ_{int} and ρ_{int} there is no requirement that the effective index of the scattering at the front and the back sides of the scattering layer be the same. Physically, this may correspond to an index grading from one side to the other or scatterers placed at an interface between dissimilar materials (this case is explored further in Table 5.2). As an example, to produce Lambertian scattering at both sides of the scattering layer, we have the following.

For $R_{\text{diff},s'a'}$, $R_{a's'}$ and $A_{\text{diff},s'z a'}$:

$$(5.9a)$$

$$P(n_{\text{eff}}) = \begin{cases} 1 & \text{for } n_{\text{eff}} = \text{Re}\{n_l\} \\ 0 & \text{else} \end{cases}$$

and for $R_{\text{diff},s'b'}$, $A_{\text{diff},s'z b'}$:

$$(5.9b)$$

$$P(n_{\text{eff}}) = \begin{cases} 1 & \text{for } n_{\text{eff}} = \text{Re}\{n_f\} \\ 0 & \text{else} \end{cases}$$

where n_l is the last layer before the scattering layer, n_f is the index of the first layer after the scattering layer and z is the layer (coherent or incoherent) where the absorption is to be calculated.

Lastly, we consider an ideal antireflection coating on the top scatterer. This situation can be modeled by setting the top interface of the scatterer to be a perfect scatterer, but without allowing any reflection or absorption as light passes through scattering layer (setting $\tau_{\text{int}} = 1$ and $\rho_{\text{int}} = 1$). Note that the top perfect scattering requirement prevents reflection from this surface at all incident angles and all wavelengths (as long as $\text{Im}\{n_{\text{last}}\}$ is small, per the above discussion).

Other special cases are outlined in Table 5.2 found in section 5.5, including absorbing scatterers and textured surfaces.

Table 5.1: Absorption modelling of special cases

<i>Conditions</i>	<i>Details</i>	<i>Schematic</i>	<i>Parameter settings</i>	<i>Limitations/ Comments</i>
Ideal back scatterer	Perfect (100%) reflection		$\tau_{\text{int}} = 0,$ $\rho_{\text{int}} = 1$	May Still have specular reflection
	Perfect scatterer		$P(n_{\text{eff}}) = \begin{cases} 1 & \text{for } n_{\text{eff}} = \text{Re}\{n\} \\ 0 & \text{else} \end{cases}$	May not be Lambertian in other layers. Large $\text{Im}\{n\}$ will cause deviation from Lambertian
Ideal intermediate or top scatterer	Perfect scattering into first layer above scatterer		$P(n_{\text{eff}}) = \begin{cases} 1 & \text{for } n_{\text{eff}} = \text{Re}\{n_l\} \\ 0 & \text{else} \end{cases}$	May not be Lambertian in other layers. Large $\text{Im}\{n_l\}$ will cause deviation from Lambertian
	Perfect scattering into first layer after scatterer		$P(n_{\text{eff}}) = \begin{cases} 1 & \text{for } n_{\text{eff}} = \text{Re}\{n_f\} \\ 0 & \text{else} \end{cases}$	See above.
	Perfect scattering both directions		When calculating $R_{a's'}$, $R_{\text{diff},s'a'}$, and $A_{\text{diff},s'za'}$: $P(n_{\text{eff}}) = \begin{cases} 1 & \text{for } n_{\text{eff}} = \text{Re}\{n_l\} \\ 0 & \text{else} \end{cases}$ When calculate $R_{\text{diff},s'b'}$, $A_{s'zb',\text{diff}}$: $P(n_{\text{eff}}) = \begin{cases} 1 & \text{for } n_{\text{eff}} = \text{Re}\{n_f\} \\ 0 & \text{else} \end{cases}$	See above.
	Perfect antireflection		$P(n_{\text{eff}}) = 1$ if $n_{\text{eff}} = \text{Re}\{n_l\}$ $P(n_{\text{eff}}) = 0$ else $\tau_{\text{int}} = 1,$ $\rho_{\text{int}} = 1$	Light leaving front after reflections from deeper layers will have Lambertian scattering.

5.3. Numerical demonstrations

Figure 5.4 shows four examples of multilayer structures with scattering layers interspersed to illustrate some of the potentially useful designs that can be calculated using the above-outlined method. For a thin-film photovoltaic device, it is desirable to place a scattering object either on the top surface, the back surface, or in the middle of the device to increase the optical path length [23], [41], [123]. However, it is not always obvious where the most appropriate placement should be *a priori*. Figures 5.2(a)-(c) shows three examples of a thin a-Si layer with a scattering layer placed at different positions within the structure. The layer stack consists of two coherent layers, a 70 nm SiN layer (often used as an anti-reflection coating or a spacer layer between the scatterer and the active material) and a 30 nm absorptive a-Si layer, and a scattering layer. The scattering layer, which is characterized by τ_{int} and ρ_{int} both equal to 0.95 (chosen for demonstrative purposes but are similar to experimental values used below), has an effective index of 1.5 (index of many optical materials, such as glass). In addition to the wavelength-dependent absorption, the predicted short-circuit current for an ideal solar cell can be calculated. Taking the a-Si as the photovoltaic layer, and assuming that each absorbed photon generates an electron-hole pair that is subsequently collected, the short-circuit current density is:

$$J_{sc} = e \int_0^{\infty} S(\lambda) * A_{a'z b'}^{\text{tot}}(\lambda) * \left(\frac{\lambda}{hc}\right) d\lambda, \quad (5.10)$$

where λ is the incident wavelength, $S(\lambda)$ is the spectral power density (taken to be AM1.5G illumination) and e , h and c are electron charge, Planck's constant and the speed of light, respectively. Note that this calculation can only accurately be performed when the per-layer absorption ($A_{a'z b'}^{\text{tot}}(\lambda)$) is known. Using the above equations, we are able to accurately determine that, for these structures (Fig. 5.4a-c), the scattering layer should be placed on the top for best performance, *i.e.* maximized absorption in the a-Si layer.

Figure 5.4(d) shows the absorption within each layer of a structure with a large number of absorbing layers. The colors in the shaded regions correspond to the layers shown in the inset of this figure. This structure uses the same scattering layer parameters used in Fig. 5.4(a)-(c) and has two non-absorbing layers (depicted as white in the inset): a 100 nm SiO₂ layer on the top and an 80 nm SiN layer in the lower half. The bottom bulk Ge layer (yellow) is an incoherent layer. This structure is meant to roughly correspond to a more complex device where absorption can occur in specific, isolated layers (*e.g.* a multi-junction solar cell) where a scattering layer has been placed between the two absorbing layers (note: this is not meant to be a suggestion of an actual device; the materials were chosen to give an example of the method only).

Again, this method allows for accurate determination of absorption in each layer individually.

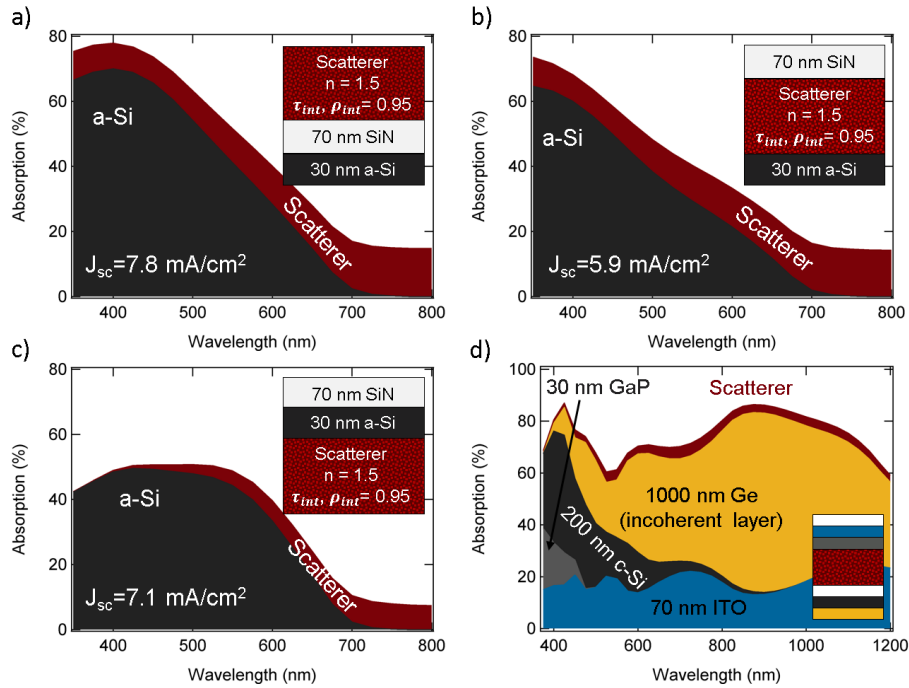


Figure 5.4: Examples of absorption calculated in individual layers using the method described above. (a)-(c) Plots show the separately determined absorption in an a-Si layer and a scattering layer when the scattering layer is (a) on the top, (b) in the middle, or (c) on the bottom of the multilayer stack. In all cases, the structure contains a SiN thin-film above the a-Si layer, and the scatterer has an effective refractive index of 1.5 and an internal absorptivity and transmissivity of 5% and 95%, respectively. Each plot is also labeled with a predicted short-circuit current density corresponding to an ideal device under AM 1,5G illumination. This value could not have been accurately calculated without first determining the absorption in each layer. (d) Shows the absorption in each layer of a more complicated multilayer structure. The layers are color coded by material and placement within the stack (see inset). The white layers are 100 nm of SiO₂ on the top and 80 nm of SiN in the lower half. The scattering layer has the same parameters as used in (a)-(c). Note that in all cases the absorption of the scatterer is calculated as the difference between the total absorption and that of all other structures. Illumination is from the top.

In addition to the computational examples provided above, two experiments are conducted and our method is used to separately determine the absorption in each of the individual layers. In both examples, the scattering characteristics are determined experimentally using a custom gonioreflectometer, as described in Ref [118]. The values of τ_{int} and ρ_{int} are fit for each of the scattering layers using transmission and absorption measurements on independent structures. The indices and thicknesses of the layers are determined using ellipsometry and confirmed by step height measurements from an atomic force microscope. Absorption and transmissions measurements are performed using the integrating sphere setup described in our previous work [118].

Figure 5.5(a) shows the measured total absorption (circles) for a structure consisting of two layers of ITO (indium tin oxide) on glass separated by a scattering layer (a polymer dispersed liquid crystal (PDLC [124])) and the calculated absorption in each of the individual layers. Similarly, Fig. 5.5(b) shows the measured and calculated absorption for an ITO coated glass slide with a scattering layer on the back (barium sulfate nanoparticle paint) [118]. In both cases, the total calculated absorption closely matches the measured total absorption. These simple examples are presented merely to demonstrate the experimental utility of the theoretical framework outlined above and its applicability to a variety of samples.

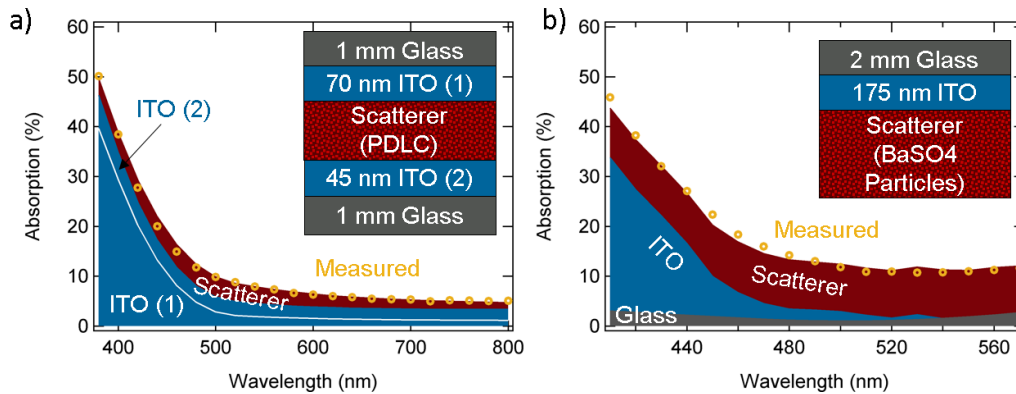


Figure 5.5: Experimentally determined total absorption (open circles) agrees with the total absorption calculated from our model by adding up the absorption in the individual layers. The model enables the determination of how much light was absorbed in each layer, which was not possible through the absorption measurement alone. (a) A scattering structure containing two (different) absorbing ITO layers and a scattering layer composed of a polymer dispersed liquid crystal (PDLC) suspension. Note that the absorptivity of the glass used in this device is found to be immeasurably small and is not shown here. (b) Absorption in a scattering structure composed of barium sulfate nanoparticles applied to an ITO coated glass slide.

5.4. Conclusions

In this chapter we presented an analytical description of absorption in individual layers of stratified medium containing a scattering layer that randomizes the light. We showed how this calculation can be carried out in the presence of an arbitrary set of layers containing both coherent and incoherent layers. We considered some important special cases. Finally, we

offered several theoretical and experimental examples to demonstrate some of the potential applications of this approach. The generality of these equations should be of particular interest with perhaps the most severe restriction being internal randomization of light within the scattering layer. However, with this criterion met, the theory requires only that the scattering layers be described by two experimentally measurable parameters [118]. Thus, the equations presented here are completely agnostic toward the actual nature of the scatterer and enable the calculation of absorption within each layer individually, which should aid in the development and screening of many potential optoelectronic devices designs, *e.g.* thin-film photovoltaics, photodetectors, etc.

5.5. Summary of special cases and variables

The following tables are provided as a reference guide to several additional cases of particular interest and as a summary of the variables used in this chapter.

Table 5.2: Table of additional special cases

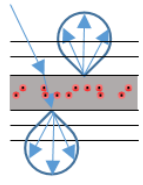
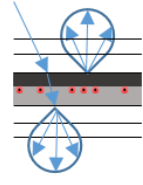
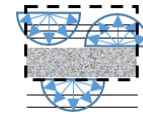
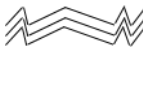
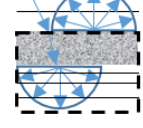
<i>Conditions</i>	<i>Details</i>	<i>Schematic</i>	<i>Parameter settings</i>	<i>Limitations/Comments</i>
Embedded scatterers including strongly absorbing particles	In non-absorbing layer		Treat embedding layer as the scattering layer $P(n_{\text{eff}}) = \begin{cases} 1 & \text{for } n_{\text{eff}} = n_{\text{min}} \\ 0 & \text{else} \end{cases}$ where n_{min} is smaller $Re\{n\}$ of either the particles or embedding material	The physical situation described is only accurately modeled if the strongly absorbing particles are far from interfaces
Scatterers at interface including strongly absorbing particles	In non-absorbing layers		Treat two surrounding layers as a single scattering layer Upper half: $P(n_{\text{eff}}) = \begin{cases} 1 & \text{for } n_{\text{eff}} = n_{\text{min}} \\ 0 & \text{else} \end{cases}$ where n_{min} is smaller $Re\{n\}$ of the particles or upper material. Lower half: $P(n_{\text{eff}}) = \begin{cases} 1 & \text{for } n_{\text{eff}} = n_{\text{min}} \\ 0 & \text{else} \end{cases}$ where n_{min} is smaller $Re\{n\}$ of the particles or lower material.	The physical situation described is only accurately modeled if the strongly absorbing particles are far from interfaces
Texturing	Perfectly random surface on top	Actual:  Modeled: 	Model with diffuse illumination: Change $\langle T_{a's'} \rangle$ and $\langle R_{a's'} \rangle$ to $\langle T_{\text{diff},a's'} \rangle$ and $\langle R_{\text{diff},a's'} \rangle$ And model with a scattering layer just below last textured surface with: $P(n_{\text{eff}}) = \begin{cases} 1 & \text{for } n_{\text{eff}} = Re\{n_f\} \\ 0 & \text{else} \end{cases}$ And $\tau_{\text{int}} = 1$, and $\rho_{\text{int}} = 1$	Ignores multiple reflections at textured surface
	Perfectly random back reflector	Actual:  Modeled: 	Model with scattering layer inserted in last layer before textured layers. Set scattering layer as "Ideal Lambertian both directions" from Table 5.1.	

Table 5.3: Table of variables for absorption modelling

Variable	Description	Equations
I	Scattered intensity per solid angle	5.1
I_0	Arbitrary normalization constant	5.1
θ	Angle between surface normal and propagation direction	5.1
T	Transmitted intensity	5.1
n_{eff}	Effective index of scattering layer	5.1
n	Index of a non-scattering layer	5.1
$P(n_{\text{eff}})$	Probability of scattering from a given effective index	5.1
$R_{a'b'}$	Reflected intensity of light travelling from the a' th to b' th incoherent layer	5.2a,c, 5.3a,b, 5.5a-c
$T_{a'b'}$	Transmitted intensity of light travelling from the a' th to b' th incoherent layer	5.2a-c, 5.5a-c
$A_{a'b'}$	Total absorption for light travelling from the a' th to b' th incoherent layer	5.2c
$R_{\text{diff},s'a'}$	Total integrated diffuse reflection for light traveling from the scatterer to incoherent layer a'	5.2a,b,d, 5.3a,b, 5.6a-e
$T_{\text{diff},s'a'}$	Total integrated diffuse transmission for light traveling from the scatterer to incoherent layer a'	5.2a,e
R_{scat}	Total reflection for light starting just inside the scattering layer and propagating to the back half-space.	5.2a,b,d, 5.6a-d
T_{scat}	Total transmission for light starting just inside the scattering layer and propagating to the back half-space.	5.2a,b,e, 5.6c,e
τ_{int}	Ratio of the transmitted intensity to ρ_{int} from the scatterer	5.2d,e, 5.6b,d,e,
ρ_{int}	Sum of the reflected light and transmitted light intensities from the scatterer	5.2d,e, 5.6b,d,e,
$\theta_{s'}$	Angle between surface normal and propagation direction inside scattering material for a given n_{eff}	5.3a, 5.6f
q	Relative parallel component of k -vector	5.4a-h, 5.5a-c, 5.6a
k_{\parallel}	Parallel component of k -vector	Inline only
k_0	Magnitude of k -vector in freespace	Inline only
\tilde{A}_{ajb}	The absorption in the j th layer for light passing through the coherent stack starting from layer a and going to layer m	5.4a, 5.5b

c	Speed of light in vacuum	5.4a
ϵ_0	Permittivity of freespace	5.4a
α_j	Absorption coefficient in j^{th} layer	5.4a
n_j	Refractive index in j^{th} layer	5.4a-e
$E_{\perp,j}$	Perpendicular component of electric field in j^{th} layer	5.4b,c,f
$E_{\parallel,j}$	Perpendicular component of electric field in j^{th} layer	5.4d,e,g
x	Distance from front of j^{th} layer	5.4a-e,g
d_j	Thickness of j^{th} layer	5.4c,e,g,h
$r_{ja'}$	Field reflection coefficient for all layers from layer j to the next incoherent layer a'	5.4c,e,g,h
$t_{ja'}$	Field transmission coefficient for all layers from layer j to the next incoherent layer a'	5.4h
$t_{a'jb'}^+$	Total field transmission coefficient from the a'^{th} layer to the j^{th} layer, including cavity field enhancement due to layers j through b' .	5.4c,e,g,h
$A_{a'jb'}$	The absorption, in the j^{th} layer (thin film) that is between any two incoherent layers, a' and b' , with light originating in the a'^{th} layer and ending in the b'^{th} layer	5.5a, 6a,f
$\mathcal{A}_{a'jb'}(q)$	Absorption in j^{th} layer (thin film) between two incoherent layers a' and b' where the a'^{th} layer is the last incoherent layer before layer j	5.5a,b
$A_{a'}$	Absorption for a single pass through the a'^{th} (incoherent) layer	5.5a-c
$A_{s'z a'}^{\text{tot}}$	Absorption in z^{th} layer for light leaving scattering layer s' and ending in incoherent layer a'	5.6a,c,f, 5.9a,b
J_{sc}	Short circuit current density	5.10
λ	Wavelength of light in freespace	5.10
$S_{AM1.5G}(\lambda)$	Spectral power density for AM1.5G illumination	5.10
h	Plank's constant	5.10

Chapter 6: Electrically controllable light trapping

In order to absorb a significant fraction of the incident solar irradiation, thin-film photovoltaic devices require light trapping and scattering [11], [23], [41], [61], [69], [72], [125]. However, for some applications, such as building-integrated photovoltaics (BIPV) [126]–[140], partial absorption is preferred to enable operation as a semi-transparent window. The basic trade-off between power generation and window transparency must be decided *a priori*. An alternative technology, switchable smart windows, have recently gained considerable interest for both privacy and climate control [141], which have been designed to modulate their optical transmission using a wide range of mechanisms including: electrochromism [133], [141]–[145], thermochromism [138], [146]–[148] and liquid crystal alignment [132], [141], [145], [149]–[152]. These devices often target control of sunlight to reduce heating and cooling loads or to enhance user comfort by modifying the intensity/spectrum of solar irradiance entering the building [141], [143], [153]. Some smart windows have demonstrated mechanical self-powering or automatic response to changing conditions [142], [144], [152], [154], [155] using photovoltaics or chemical process that responds to light or heat. However, they work by modifying the absorptivity of the switching material, which results in wasted energy from the incident light. In this chapter, we describe the development of an electrically

switchable light trapping layer and its application to a smart, switchable solar window design.

6.1. Self-powered switchable solar windows

Here we present a self-powered switchable smart window concept that enables variable transmissivity, diffusivity, and power generation on-demand that can be adjusted throughout the day. The design consists of a thin absorbing layer (a-Si) and an actively tunable scattering material (polymer dispersed liquid crystal) that allows the device to switch between a low power-generating transparent state (1.9 mW/cm^2) and a high power-generating diffuse state (3.2 mW/cm^2) for a 28 nm a-Si film. The power required to operate the device is $<0.8 \text{ mW/cm}^2$, showing that under typical solar illumination, it is self-powering.

To switch between a transparent and diffuse state, the device incorporates a polymer dispersed liquid crystal (PDLC) layer (Fig. 6.1), which is comprised of microdroplets of a liquid crystal (LC) material dispersed in a polymer matrix. As expected, in its OFF state (no applied voltage), PDLCs strongly scatter light, appearing hazy or opaque due to light scattering from the random orientation of the liquid crystals resulting in refractive index variation throughout the material. When enough voltage is applied across the film, the liquid crystal alignment reduces the refractive index contrast for light

travelling parallel to the alignment direction, and the material becomes highly transparent owing to the suppressed scattering [124]. Since its original discovery [156], researchers have extensively explored the potential applications of PDLCs in the areas of flat panel displays [157], [158], smart windows [145], [159], and microlens [160]. Nematic liquid crystals are the most common type employed in PDLC devices. The droplets are optically birefringent with ordinary refractive index n_o along two optical axes and extraordinary refractive index n_e along the third axis. The polymer is optically isotropic with refractive index n_p . In the absence of an applied electric field (OFF state), the optical axes of individual droplets align approximately randomly, resulting in spatial variations of refractive index across the film, which cause strong light scattering. In the presence of an electric field (ON state), molecules in a liquid crystal material with positive dielectric anisotropy align their long axes parallel to the applied electric field. In this case, light incident normal to the plane of the film experiences a refractive index of n_o in the liquid crystal droplets. When n_o and n_p are matched, the film is transparent in this state [161, p. 2000]. Smart windows incorporating PDLCs can use the dynamic opacity variation for privacy, glare reduction, and to minimize the cost of indoor climate control; [132], [141], [145] however, to remain in a transparent state, power must be continuously supplied to the window.

To create a self-powered switchable smart window, we combine a PDLC cell with an a-Si absorbing layer. In the ON state of the PDLC, the cell is highly transparent, and in the OFF state the absorption in the a-Si is enhanced by the scattering from the PDLC. We use the techniques discussed in Chapters 2-4 to accurately determine the absorption in the a-Si layer [118], [162] and demonstrate that a complete photovoltaic device would achieve self-powering even in the weakly absorbing ON state. In contrast to other switchable smart window devices that modulate transmission by increasing absorption, these PDLC-based devices modulate transmission via scattering. The reflective scattering while in the OFF state captures this otherwise wasted energy and significantly increases photovoltaic performance without changing its color. Further we show that these devices have several favorable characteristics for privacy and temperature control, such as switchability of haze, opacity, and overall transmission.

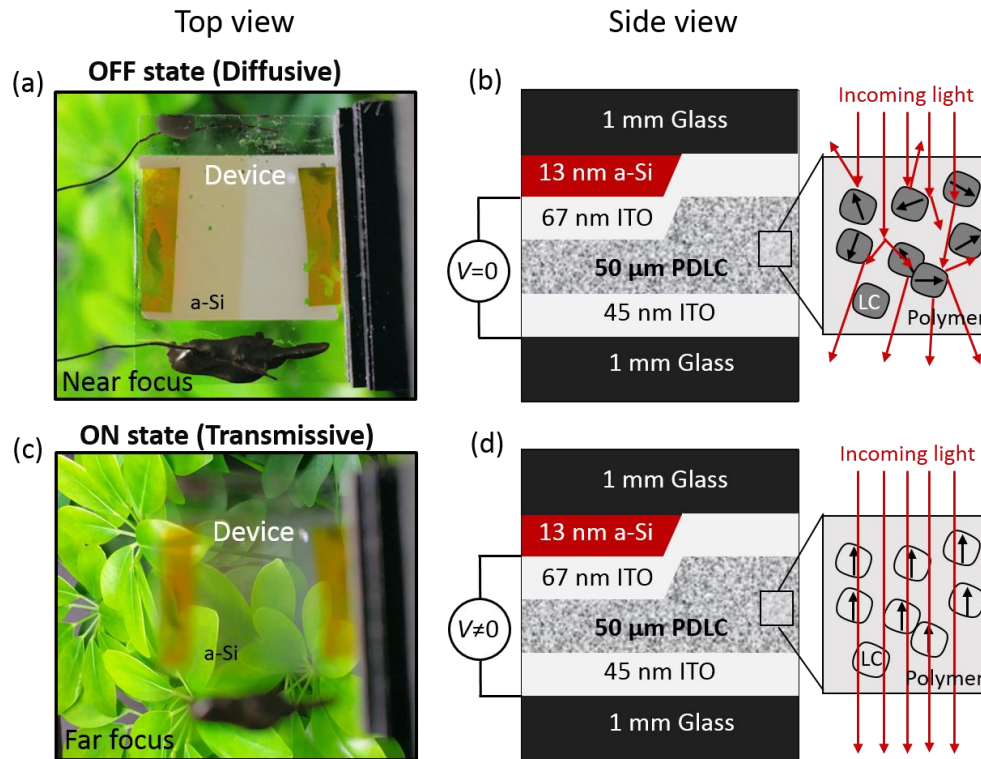


Figure 6.1. Switchable solar cell image and schematic. (a) Photograph and (b) schematic of a representative device in the OFF (*i.e.* diffusive) state with no applied bias. The structure is 2.00 cm x 1.57 cm, and the plant in the background is held at a distance of 35 cm. The amber-colored side of the device (left) incorporates a 13 nm a-Si layer, while the right side has no additional absorbing layer for comparison. In the OFF state, the liquid crystal microdroplets are randomly oriented. The refractive index variation causes significant light scattering, which results in diffuse transmission, and hence can be used as a privacy window. (c) Photograph and (d) schematic of the same device in the ON (*i.e.* transmissive) state with an applied voltage of 150 V (square wave). The liquid crystal alignment in the ON state results in a uniform refractive index for normally incident light and, thus, high transmission.

Figure 6.1 shows the device operation and a schematic of both the transparent and opaque states. The structures consist of E7 liquid crystal

suspended in NOA65 optical adhesive sandwiched between ITO coated glass slides. Each device contains a 13 nm thick layer of a-Si, which covers half the structure (Fig. 6.1b). Here we chose a-Si because it is a common thin-film solar cell material for which we can easily control the deposition thickness (see Section 6.2.1 for details about sample preparation). For the OFF state of the device, no voltage is applied between the top and bottom indium tin oxide (ITO) layers. In the ON state, a 200 Hz square wave is applied between the leads (note: DC operation for extended amounts of time can damage PDLC layers due to ion migration [163]). While the devices are capable of continuous variation of opacity, for simplicity and clarity, we chose binary operation at either 0 V (OFF, diffusive) or 150 V (ON, transmissive).

Devices were fabricated and tested with different a-Si layer thicknesses (13 and 28 nm) to determine the optical properties in both the ON and OFF states. Figure 6.2a-d shows the total absorption both measured (circles) and calculated (solid lines), as well as the absorption in individual layers (represented by the colored areas). Note that the data for both ITO layers (top and bottom) are combined in this plot. The absorption in the individual layers is calculated by determining the total electric field power density in each layer (adding reflections/transmissions from thin films coherently) and using the absorption coefficient for each material (see Section 6.2.2). In the OFF (*i.e.*

diffusive) state, the data is calculated following Ref [162] under the assumption that light entering the PDLC becomes fully randomized, which is supported by internal scattering measurements [118] (see Section 6.2.5). ON state calculations assume no scattering. The total measured and calculated data are in close agreement with RMS errors of 1.65%, 0.73%, 0.47%, and 2.56% (absolute) for the data in Figs. 6.2a-d, respectively.

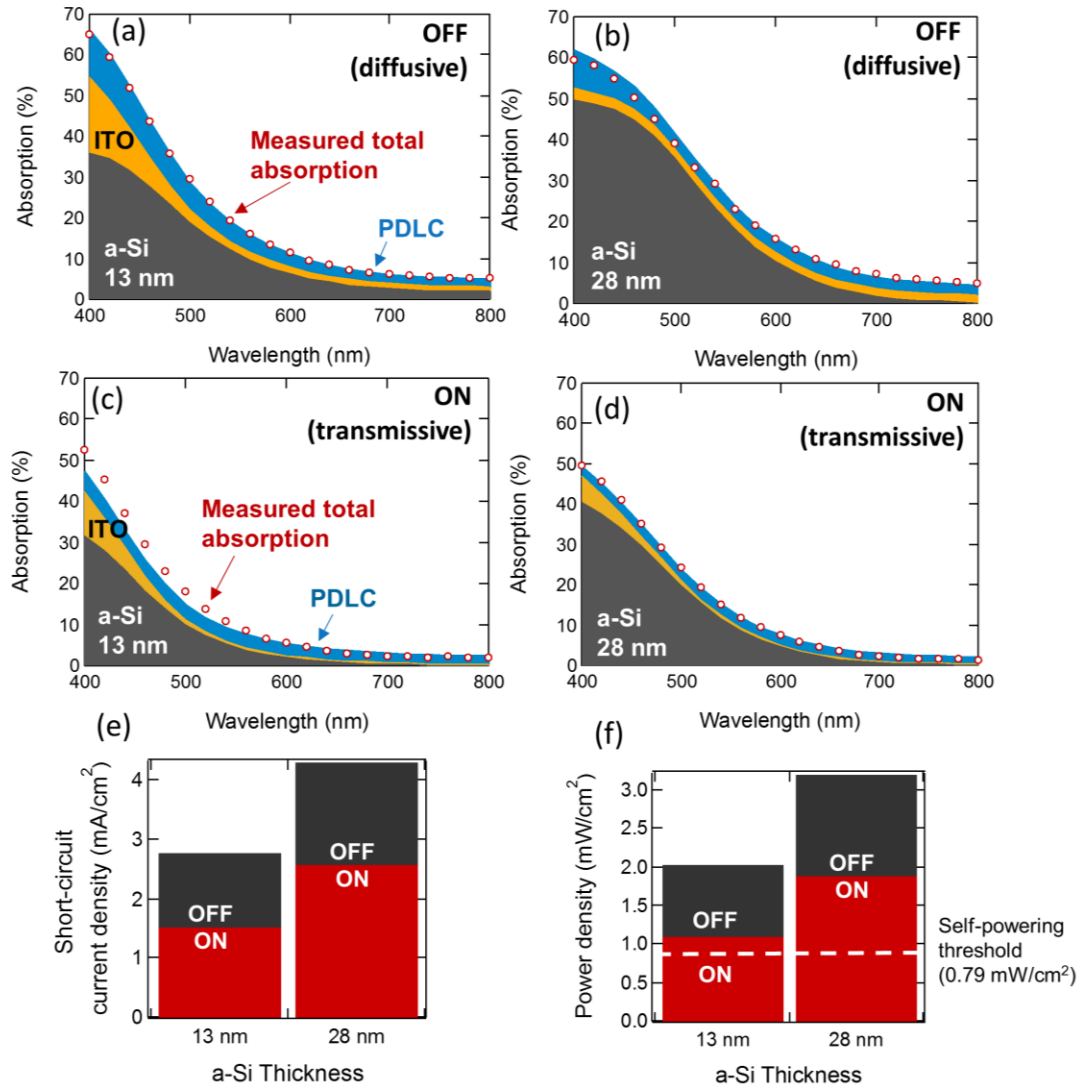


Figure 6.2. Absorption and power generation of switchable solar windows. (a-d) Measured (circles) and calculated (shaded areas) absorption for devices with two a-Si thicknesses (13 nm (a,c) and 28 nm (b,d)) in the OFF state (a,b) and the ON state (c,d). The absorption is calculated in each material, and the total absorption is measured. Calculated (e) short-circuit current density and (f) power generation density are shown with the self-powering threshold marked as a dashed line.

After determining the total absorption within the a-Si layer, we calculate the expected power generation from a complete photovoltaic cell incorporated into the switchable solar window and determine the potential for self-powering. While developing a high-performance a-Si solar cell is beyond the scope of this work, we calculate short-circuit current density based on the measured absorption within the a-Si layer of the PDLC device (Figs. 6.2a-d), weighted by the AM1.5G solar spectrum. The short-circuit current density is used to determine the generated power density (Fig. 6.2f) using a single diode model, where the reverse saturation current is obtained by extrapolation from experimental data of a high quality a-Si solar cell [164], [165] (see Section 6.2). The dotted line in Fig. 6.2f indicates the threshold for self-powering, given by the power consumption of the PDLC device in the ON state divided by the area of the cell (3.14 cm^2), as described below.

The measured power consumption within the PDLC layer is determined in two steps because of the large dynamic range required for the measurement (~6 orders of magnitude), see Fig. 6.3. First, the power is measured during the charging and discharging of the PDLC (driven by a square wave at 200 Hz) due to its capacitance. Second, the power is measured during steady state current operation, which is found to be $3.5 \text{ }\mu\text{A}$, corresponding to a shunt resistance of $42 \text{ M}\Omega$. Figure 6.3a shows the voltage applied across the device

as a function of time, and Fig. 6.3b,c shows a zoom in of the voltage, current, and power used during a polarity switching event (shaded region in Fig. 6.3a). Here, the negative power corresponds to the energy recovered by discharging the PDLC cell. The total average power density needed to operate the device is $<0.8 \text{ mW/cm}^2$, comparable to commercially available ones [141]. In all cases considered here, this power requirement can be met by the solar energy potentially converted by the a-Si absorbing layer. Further, the OFF state of the device with the 28 nm a-Si layer generates nearly 4 times the needed power, and the OFF state of the 13 nm a-Si layer device creates more than 2.5 times the required power.

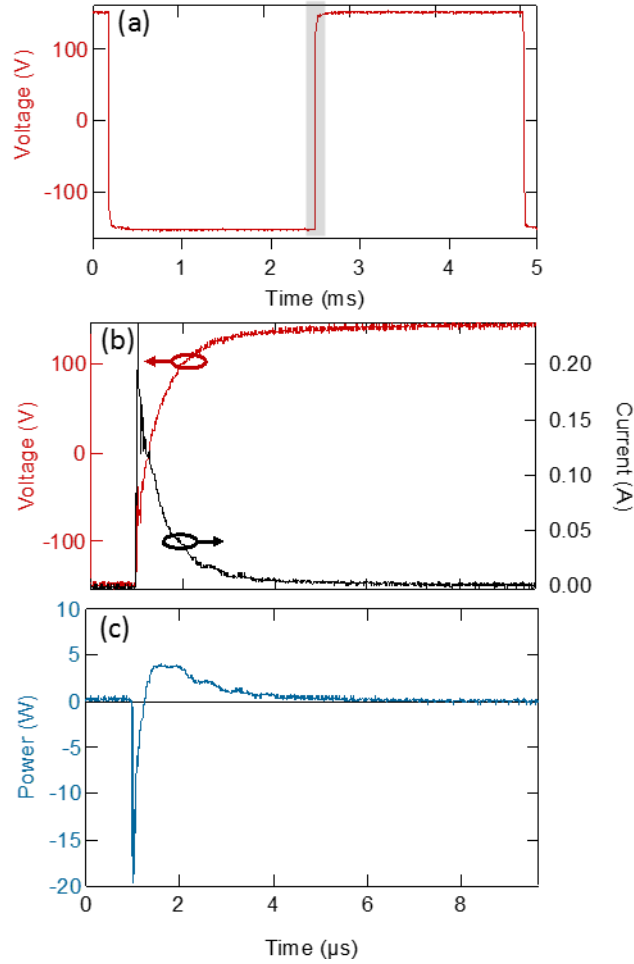


Figure 6.3. Electrical characteristics of the PDLC switchable self-powered solar window. (a) Voltage across the device as a function of time during operation in the ON state (applied square wave function with voltage of 150 V). The grey region near 2.5 ms is expanded in (b,c) for clarity. Measured (b) voltage, current, and (c) power consumed by the device during a polarity switching event. Negative power usage regions correspond to the recovery of energy stored via the capacitive nature of the device. The total power density needed for device operation is $< 0.8 \text{ mW/cm}^2$.

The generated power can be increased using a thicker absorbing a-Si layer; however, there is a decrease in transmission, as shown in Fig. 6.4a. The structure with no a-Si (corresponding to maximum transmission but no power generation) has a nearly flat, colorless transmission spectrum with a 13% change between 460 nm to 650 nm (the range over which the photopic sensitivity of the human eye is >10% of the max sensitivity [166]). For the device with a 13 nm a-Si layer, we observe a similar flatness for $\lambda \geq 500$ nm, resulting in a slight amber or brown tint (Fig. 6.1a,c). For the device with a 28 nm a-Si layer, we observe the same trend but with a slightly darker tint. While not completely colorless, they do demonstrate the generally accepted light brown color for tinted glass. The transmission in the OFF state shows the same trends but at a lower mean value (Fig. 6.4a) due to the increased reflection and scattering, which benefits the power generation (Fig. 6.2). In the wavelength range shown, the AM1.5G weighted transmission can be reduced by more than a third by switching between the ON and OFF states. In contrast to many other smart window designs, this reduction is primarily due to reflection rather than absorption, which can have a very significant impact on cooling costs by limiting optical heating of the windowed room [141], [143], [153].

In addition to the nearly flat transmission spectrum, the device scatters light uniformly in all directions when operating in the OFF state,

demonstrating its effectiveness as a privacy window. Figure 6.4b shows a polar plot of the scattered transmission and reflection as a function of wavelength for a typical PDLC device with no a-Si in the OFF state (normalized to the near-normal incidence reflection data). Note that this data is obtained from a more complete scattering characterization that includes internal scattering within the device (see Supporting Information), where a nearly-Lambertian scattering profile is found for all wavelengths.

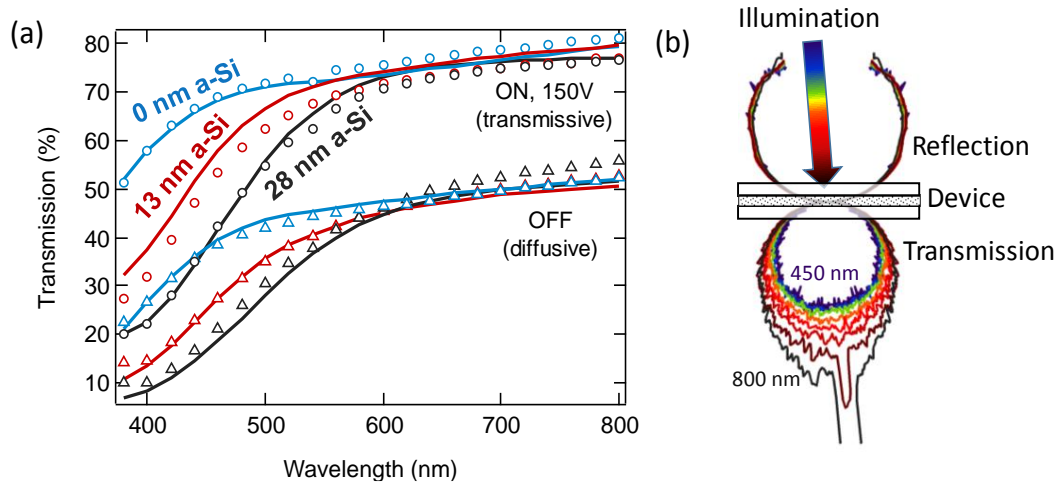


Figure 6.4. (a) Transmission spectra for the PDLC switchable solar windows in the ON (circles) and OFF (triangles) states. The solid lines refer to the modeled transmission. (b) Polar plot of the scattered transmission and reflection as a function of wavelength for the device in the OFF state.

For window applications, device performance at oblique incidence is important. Figure 6.5 shows the measured absorption in both the ON and OFF

states for the structure with 13 nm thick a-Si at both near-normal incidence and 45-degree illumination. The absorption in the OFF state is very weakly affected by the change in angle. However, the measured absorption in the ON state is markedly different at 45 degrees, and it is significantly greater than the calculated value. This difference is explained by the inset of Fig. 6.5, which shows the scattered intensity as a function of both incident and scattered angles. At near-normal incidence, almost no scattering occurs. As the incident angle increases to 45 degrees, scattering increases with most light scattered at large angles. This behavior is due to the random position of the liquid crystal micro-droplets. Though the applied field in the ON state orients the optical axis of the microdroplets, light entering at non-normal incidence has a component traveling along the extraordinary axis of the liquid crystal, which is scattered by the index contrast. This effect can have a large influence on absorption because light is preferentially scattered at larger angles as a result of the higher index seen by light propagating in that direction. Note that the scattering in the ON state is still weaker than in the OFF state (see Section 6.2 for details of OFF state scattering and internal scattering distributions). The measured absorption in the OFF state for 45-degree illumination would yield 1.3 mW/cm² of power generation, which is greater than the self-powering threshold, thus demonstrating that these devices would be self-powering. For the ON state at

45-degree illumination, the absorption within the a-Si is expected to be at least as high as in the near-normal case, based on the higher measured absorption compared to the model. Thus a minimum power generation of $>0.8 \text{ mW/cm}^2$ is expected, again enabling self-powering.

In order to evaluate overall performance, we also calculate mean power with the sun at 0 to 90 degrees from normal. Following the same procedure as above, we find a mean power generation of 0.7 mW/cm^2 and 1.2 mW/cm^2 for 13 nm of a-Si in the on and off states respectively, with 1.2 mW/cm^2 and 2.0 mW/cm^2 mean power generation for 28 nm of a-Si in the on and off states respectively. The lower power generation is due to higher reflection and lower cross section of the cell at larger incident angles. As stated above, the on state calculation, which assumes no scattering, becomes a poor approximation at shallower angles and the actual absorption in this case should approach the off state absorption. Thus the average power generation is still expected to exceed the self-powering level.

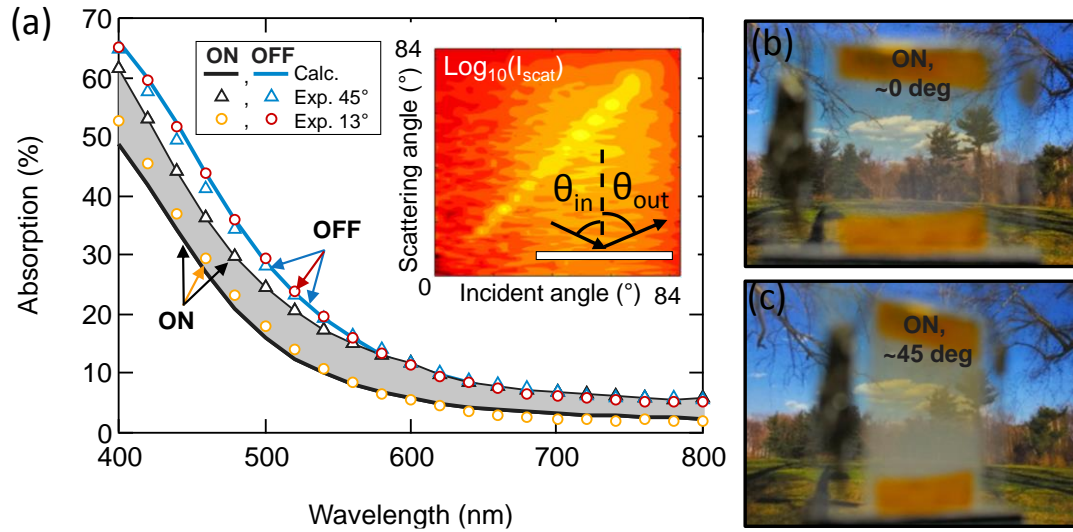


Figure 6.5. Switchable smart solar window at 45 degree illumination. (a) Measured (open symbols) and calculated (solid lines) absorption for the PDLC device with 13 nm of a-Si. Here, the absorption at a 45° incident angle is compared to the near-normal absorption from Fig. 6.2. The shaded region denotes the difference between the measured ON state absorption at 45° illumination and the calculated ON state absorption at 45° illumination assuming no scattering. The inset shows a log map of scattered light intensity as a function of both incident (θ_{in}) and reflected scattering (θ_{out}) angles. Optical image through the device in the ON state at (b) normal incidence and (c) 45° from normal.

6.2. Fabrication methods and experimental details

This section contains additional details concerning the sample preparation, material and device characterization, and relevant calculations to determine the expected and measured properties of the switchable solar smart windows.

6.2.1. Sample preparation

The bottom ITO coated glass was obtained from a commercial manufacturer (SPI Part # 6466-AB). The a-Si layer was deposited by RF sputtering in Argon onto glass coverslips. Samples were mechanically shadowed, covering only half of the glass with absorbing a-Si (Fig. 6.1). This shadowing procedure allowed for later direct measurement of the PDLC cell on the same device without a-Si. The absorbing layer was then coated with ITO by sputtering from a single ITO target in 7% oxygen, 93% Argon. During each sputtering step, additional samples were included for later characterization (see below). The PDLC mixture consisted of liquid crystal E7 and photocurable polymer NOA65 (Norland Products) with 50:50 weight ratio. It was then filled into an empty cell made with the top and bottom coated glass slides, separated by a Kapton spacer layer approximately 50 μm thick. The cell was then cured at room temperature for 1 min with a UV lamp [167].

6.2.2. Material characterization

The materials were characterized using ellipsometry, atomic force microscopy (AFM), and absorption and transmission measurements. The refractive indices of the films were measured by ellipsometry. Film thicknesses and roughnesses (found to be negligible at $<5 \text{ \AA}$ RMS for the a-Si films and 7 \AA

RMS for the ITO film) were measured by AFM and confirmed with ellipsometry (see below). The imaginary part of the index of refraction were further refined (ellipsometry was relatively insensitive to very small amounts of absorption) by adjusting the ellipsometric fit to jointly agree with the independent absorption measurements. Absorption and transmission was measured in a 6" integrating sphere (Labsphere RTC-060). This sphere uses a center mounting holder for direct measurement of absorption (from the total combined reflection and transmission). Absorption was measured at 13° incidence for near-normal measurements, while transmission was measured at 7° incidence (difference due to geometric requirements of the system). The integrating sphere light intensity was monitored by a Si photodiode, and this signal was used by a lockin amplifier. The light source was a Xe lamp followed by a monochromator (SPEX 500M). Incident power was monitored to account for variations in the incident intensity, and second order diffuse absorption in the sample (light reflected or transmitted from the sample and absorbed after scattering from the integrating sphere) was accounted for by illuminating the sphere through a secondary port for calibration.

The optical parameters were jointly fit using ellipsometry, AFM measurements, and integrating sphere measurements (absorption and transmission). Figure 6.6 shows the comparison between measured (open

circles) and modeled (solid line) absorption, using joint fits for the four films used in this work. All fits have less than 1% root mean squared (RMS) error between measurement and modeling results. Similarly, Fig. 6.7 shows measured (open circles) and modeled (solid line) absorption and transmission used in characterizing the PDLC layers (note that this is for the side of the device without the a-Si layer). The characterization methodology is described in Ref [162]. Figure 6.8 shows the AFM measurements used to determine film thickness and roughness. The step heights were produced by partially covering samples during film deposition.

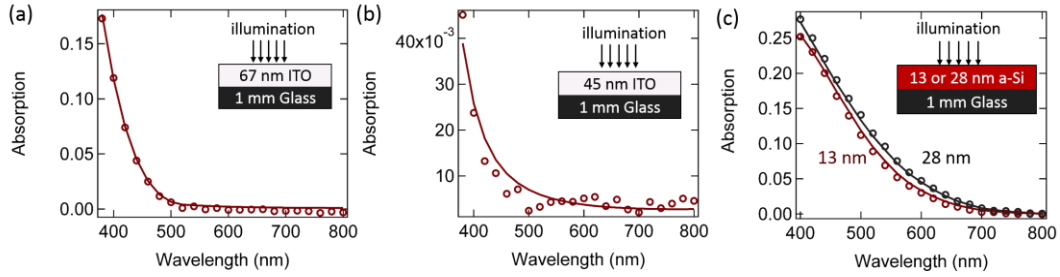


Figure 6.6. Thin-film absorption measurements and modeling. Measured (open circles) and calculated (solid lines) absorption for (a) the top ITO, (b) the bottom ITO, and (c) the a-Si layers (top and bottom refer to schematic in Figure 6.1). The modeled data are the result of a joint fit of ellipsometric data, AFM, and absorption data.

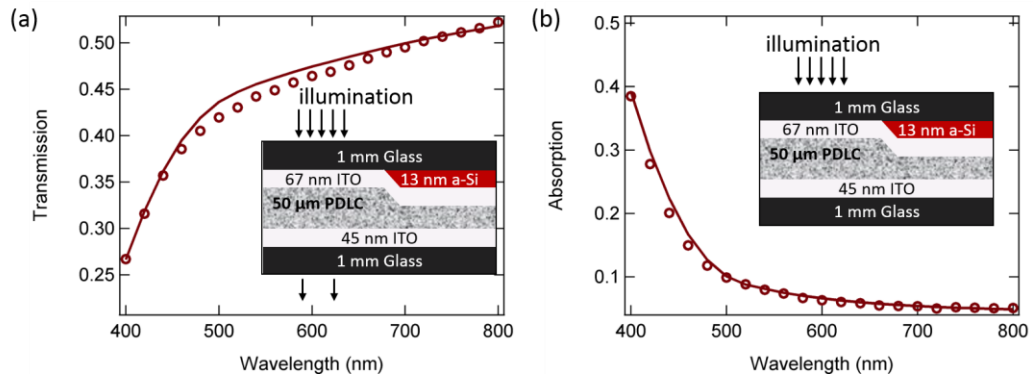


Figure 6.7. PDLC characterization. Measured (open circles) and the calculated (solid lines) absorption in the PDLC cell (side without a-Si). This measurement allows for fitting of the PDLC parameters that are necessary for accurate optical modeling of the scattering, as outlined in Ref [162].

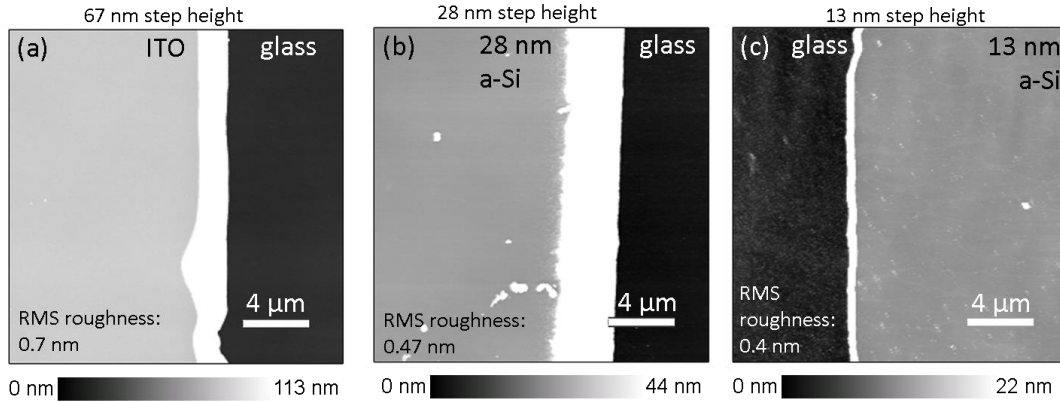


Figure 6.8 AFM step height measurements used to determine thickness of (a) the top ITO layer, (b) the 28 nm a-Si layer, and (c) the 13 nm a-Si. RMS surface roughnesses are 0.7 nm, 0.47 nm, and 0.4 nm, respectively. Step heights were produced by partially covering the samples during deposition. Bottom ITO was not manufactured in house and so no step height was available.

6.2.3. Calculating absorption

Absorption and transmission in the ON state were calculated by Fresnel coefficients using the matrix transfer method including coherent reflection/transmission (for thin-films) and incoherent reflection/transmission (for thick layers such as the glass and PDLC layer) following Katsidis and Siapakas [109]. This method uses field transfer matrices to calculate the intensity of reflection/transmission between incoherent layers (or to outside the structure) and then intensity transfer matrices to calculate the total reflection/transmission. Total absorption and transmission in the OFF state were calculated using the effective index ensemble method [118] and the per layer absorption was calculated using the model developed in Ref [162].

6.2.4. Calculating power generation

Power generation was calculated using a single diode model with current density, $J(V)$, calculated as a function of voltage, V , by:

$$J(V) = J_o \left(1 - \exp \left(V/V_{th} \right) \right) + J_{sc,calc} , \quad (6.1)$$

where V_{th} is the thermal voltage (25.9 mV at 300 K), J_o is the reverse saturation current density (see below), and $J_{sc,calc}$ is the predicted short circuit current density based on the calculated absorption, which is given by:

$$J_{sc,calc} = q \int_0^{\infty} S_{AM1.5G}(\lambda) * A_{calc}(\lambda) * \left(\lambda/hc \right) d\lambda , \quad (6.2)$$

where λ is the wavelength, h is Planck's constant, q is the electron charge, c is the speed of light in vacuum, $S_{AM1.5G}(\lambda)$ is the spectral power density for Air Mass 1.5 Global illumination, and $A_{calc}(\lambda)$ is the calculated absorption in the a-Si layer using the methods described above. J_o is extrapolated from a high quality a-Si solar cell, [164] based on the measured open-circuit voltage, $V_{oc,cell}$, and the short-circuit current, $J_{sc,cell}$, using:

$$J_o = \frac{J_{sc,cell}}{\exp(V_{oc,cell}/V_{th})}. \quad (6.3)$$

The power generation, P , is:

$$P = \max(J(V) * V). \quad (6.4)$$

Note that our goal here is to create a simple but reasonable model for the power generation of a state of the art cell incorporated into our device using experimentally determined values of the cell parameters. Figure 6.9 shows the behavior of two such devices based on our designed switchable solar windows.

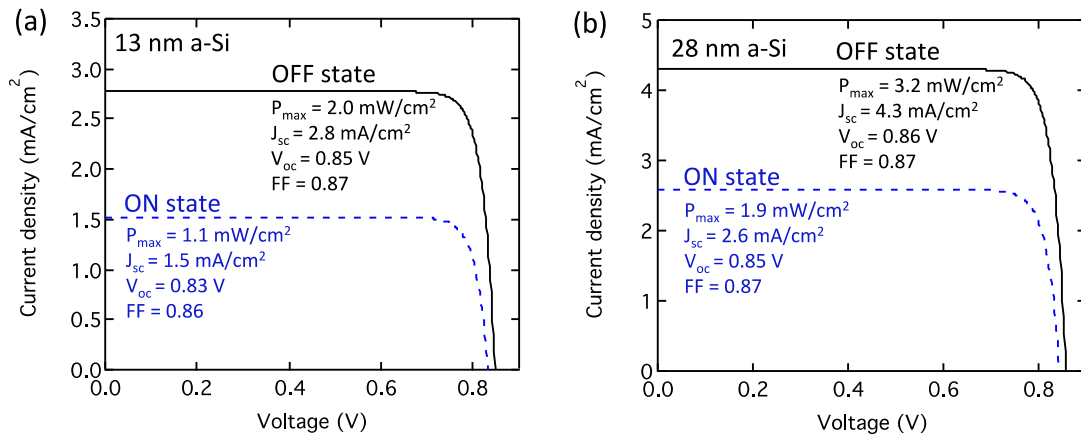


Figure 6.9: Modeled performance of solar cells comprised of (a) 13 nm and (b) 28 nm of a-Si.

Current density as a function of voltage is shown and relevant parameters are given in the insets for both the ON and OFF states.

6.2.5. Characterizing scattering

The internal scattering distribution (angularly resolved scattering inside the sample layers) was determined for accurate absorption calculations using a gonioreflectometer and by replacing the glass slide on one side with a glass hemisphere, as described in Ref [118] and Chapter 4. The OFF state per pass absorption and transmission were characterized by measurements on the part of the sample without a-Si. We used a glass hemisphere and the technique described in Ref [118] to determine the internal scattering characteristics. The hemispherical technique allows for determination of all scattering from the PDLC layer. Figure 6.10a shows a schematic depiction of the technique. An important assumption of the absorption calculations is that light is fully randomized in the PDLC layer, and the validity of this assumption is demonstrated in Fig. 6.10b. This plot shows the normalized scattering angle versus reflected angle with overlapping traces for incident angles between 5° and 30° (at higher angles specular reflection becomes too strong to be completely removed with the crossed polarizers). If light were not fully randomized in the PDLC layer, the scattering would depend on incident angle. However, no dependence is observed with relative RMS variations about the mean of only 3%.

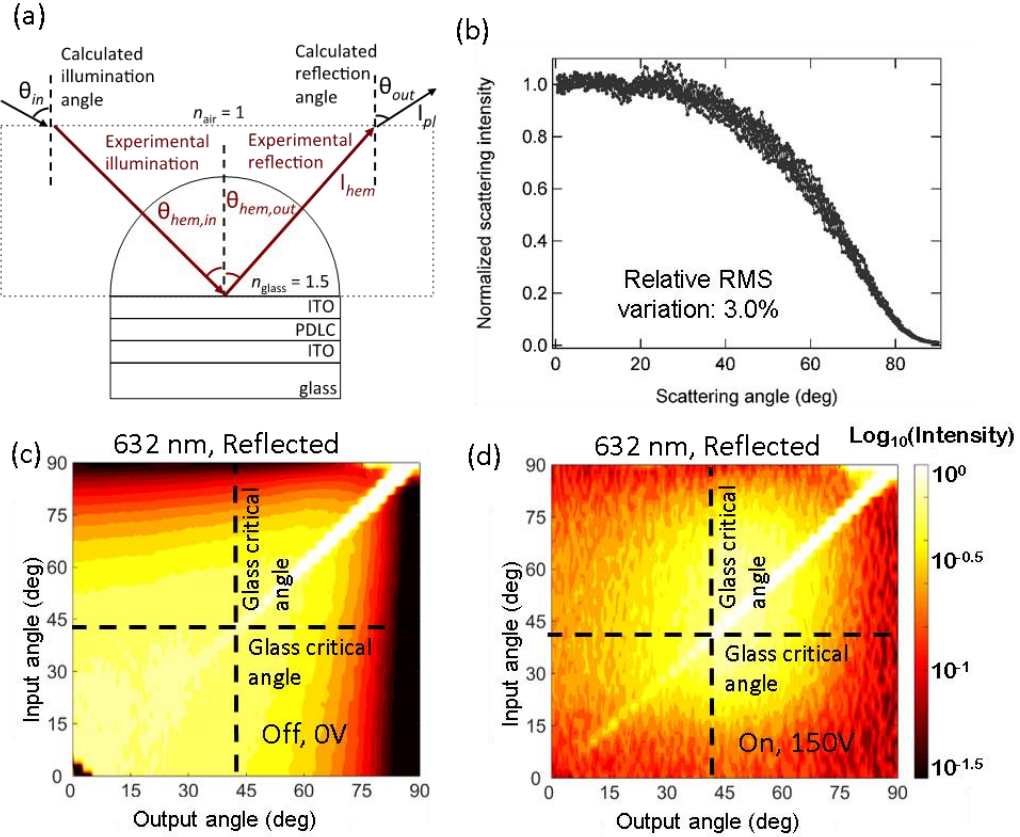


Figure 6.10: Determination of the scattering within a PDLC device. (a) A glass hemisphere allows for illumination and observation of all internal reflected scattering [118], for the purposes of modeling and extrapolating to other device configurations. Reflected scattered intensity as a function of input (illumination) angle and output (observation) angle with the device in the (c) OFF and (d) ON states. Note that only the bottom left corner of these graphs represent observable angles for a purely planar device (*i.e.* the hemisphere enables the determination of the scattering intensities in the other three quadrants).

Figure 6.10c,d shows the reflected scattering intensity as a function of incident illumination for the (c) OFF and (d) ON states. The use of the BK7 hemisphere enables complete characterization of the optical scattering within the device; however, only the data from the lower left quadrant is used to

obtain the data in the inset of Fig. 6.5. The scattering angles ($\theta_{hem,out}$) and illumination angles ($\theta_{hem,in}$) shown in Fig. 6.10, were mapped to the scattering and illumination angles (θ_{out} and θ_{in} , respectively) shown in the inset of Fig. 6.5 for a planar device by Snell's law, using the glass index of 1.5:

$$\theta_{out} = \sin^{-1}(1.5 \sin(\theta_{hem,out})) \quad (6.5a)$$

and

$$\theta_{in} = \sin^{-1}(1.5 \sin(\theta_{hem,in})). \quad (6.5b)$$

The scattering intensity is also transformed to account for the differing geometry between the hemisphere and the planar slab. First, the change in intensity due to the above change in propagation angle is accounted for by multiplying by the ratio of cosines ($\cos(\theta_{out})/\cos(\theta_{hem,out})$) to account for the increase in the solid angle for light exiting the planar slab. Second, with the hemisphere, all illumination and scattering angles experience the same transmission at the air/glass interface (*i.e.* the light is always normal to the surface), but the planar surface results in angle dependent transmission. Considering both effects, we have that the resulting intensity exiting the planar surface is:

$$I_{pl}(\theta_{in}, \theta_{out}) = T(\theta_{in})T(\theta_{out}) \frac{\cos(\theta_{out})}{\cos(\theta_{hem,out})} I_{hem}(\theta_{hem,in}, \theta_{hem,out}) \quad (6.6a)$$

$$= T(\theta_{in})T(\theta_{out}) \frac{\cos(\theta_{out}) I_{hem}(\theta_{hem,in}, \theta_{hem,out})}{\sqrt{1 - \left(\frac{\sin(\theta_{out})}{1.5}\right)^2}} \quad (6.6b)$$

where T is the transmission coefficient, I_{pl} is the calculated scattering intensity for the planar geometry (shown in Figure 6.5), and I_{hem} is the measured intensity for the hemisphere (shown in Figure 6.10).

To determine the power dissipated within the device, the current was measured by the voltage drop across a 1.2 k Ω current sensing resistor, and the voltage across the device was measured directly. These time dependent measurements were made using an oscilloscope.

6.3. Discussion

In conclusion, we have presented smart, switchable solar window devices based on an a-Si absorber and a PLDC transmission modulator. We demonstrated that these devices have the potential to self-power even in the low absorption state with as little as 13 nm of a-Si and have excellent smart window properties: high transparency and clarity (ON state) and high diffusivity (OFF state) for enhanced privacy and reduced solar heating. Their

performance is further improved for non-normal incident illumination, which is typical for real-world deployment in building integrated PV applications. These characteristics demonstrate the great potential of these switchable solar window devices with actively controllable power generation and transparency.

Chapter 7: Conclusions and outlook

This thesis provided details of our recent work on light trapping and scattering experiments, both the general theory and its applications. Our measurement technique supported the development of the index ensemble model for light scattering. The index ensemble model has proven effective for physically describing light scattering from a scattering media at a planar interface, as well as useful and accurate for predicting absorption in structures containing these scattering layers. Our index ensemble model laid the groundwork for a more general model to predict absorption in individual layers of arbitrary stratified media containing scattering layers. Finally, we combined a thin optically absorbing layer with a switchable scattering layer to create a switchable solar window with variable light trapping that has the potential for self-powering. Ultimately, this work opens up new avenues for researchers to understand and design multilayer scattering structures, which are applicable to a wide-range of optoelectronic devices including solar cells and photodetectors. In this section, we describe future directions for advanced light trapping experiments and possible technologies enabled by the work presented in this thesis.

7.1. Enhancements to PDLC switchable solar windows

Future research on switchable solar cells based on polymer dispersed liquid crystals (PDLC) should focus on the production of a power generating device and its optimization. The optimization is problematic because no single metric or figure-of-merit completely describes the device (*i.e.* the tradeoff between transparency, clarity, and power generation varies by preferred application and/or user). Production of a full working device necessitates decisions regarding several different cell design components, including choice of photovoltaic material. As presented in Chapter 6, we used a-Si for our demonstration as it is simple to deposit, has easily controllable thickness, and good long-term stability that allowed for the extensive characterization described in Chapter 6. A drawback to a-Si, however, is that it absorbs strongly in the UV and blue range, leading to amber tinting of the device. It also presents a large index contrast to light coming from the scattering layer, which reduces the amount of light entering the absorber. When designing a device for research purposes, ease of fabrication and stability can be sacrificed for improvements in performance. The two most common categories of photovoltaic materials for future window devices are perovskites and polymers [134], [136], [137], [140], [168], [169]. These materials can be made to

absorb relatively uniformly over a broad wavelength range (no tinting) and have a significantly lower index of refraction ($n = 1.5$ to $n = 2.5-4$) than a-Si.

A second design consideration in creating a full device is choice of contacts. The typical configuration of ITO as a top contact and a thin-film or grid of metal as a back contact is one possibility. Figure 7.1 shows an example of a structure using a photovoltaic device similar to Ref [134] and the resultant transmission and total absorption in the OFF and ON states. Note that no attempt has been made to optimize this example structure.

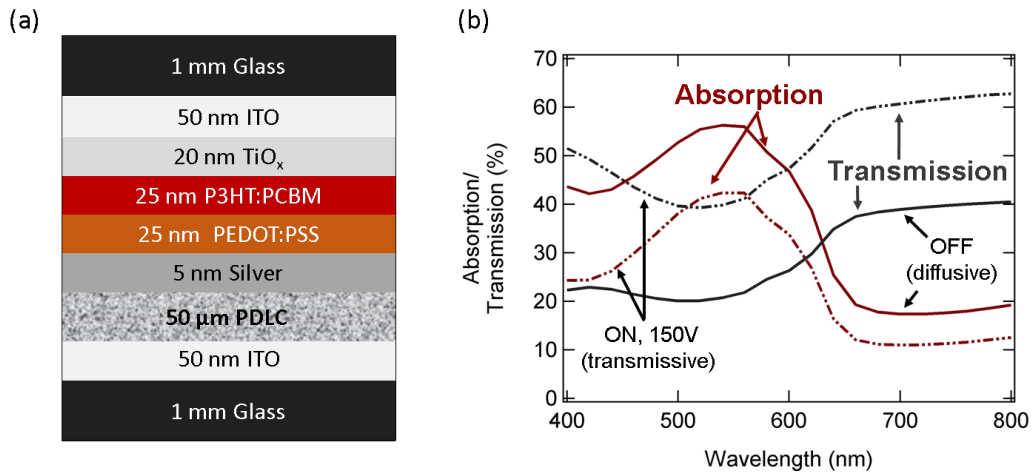


Figure 7.1: Potential design for a fully functional PDLC/solar cell device. (a) Schematic view.

(b) Total absorption and transmission for the device shown in (a).

Trade-offs exist between power consumption, transmission, OFF-state and ON-state scattering, and power generation, which leads to a second important avenue of further research: optimization. The models we present in

Chapter 5 can be used for this purpose with a few caveats. The models we created allow us to vary the properties of the individual layers in order to find the best configuration, but variation of the phenomenological values (ρ_{int} and τ_{int}) used to describe the scattering layer should be considered with caution. While ρ_{int} and τ_{int} can be modified to find optimal values, they do not directly represent design variables such as PDLC thickness. Furthermore, the model assumes that light is fully randomized in the scattering layer. In Chapter 6, we noted that this assumption begins to fail at long wavelengths; similar problems arise as the thickness is decreased. Our model easily captures optical effects resulting from changing the thickness of the conducting layers; however, effects on electrical performance have not been considered.

The first issue (*i.e.* that ρ_{int} and τ_{int} are phenomenological variables) can be resolved with specific modeling of the scattering layer itself [98], [120], [121]. Addressing the second issue (*i.e.* the deviation from complete randomization) necessitates use of a different model than the one we outlined in Chapter 5. Nevertheless, the model we presented can still give a rough estimation of the absorption in cases where the PDLC does not completely randomize the light, *e.g.* when the layer is very thin. The last issue with the electrical performance would require some further modeling and has not been investigated at this time.

Given these caveats, the model developed in Chapter 5 can be used to address optimization and to investigate trade-offs for these devices. Perhaps the simplest way to improve both transmission (for window operation) and active layer absorption (for photovoltaic operation) is to add a single or double layer anti-reflection coating as described in Chapter 1. One downside of these coatings is that they create angle and/or wavelength selectivity that can degrade transmission color flatness or solar cell effectiveness throughout the day. Another strategy that can be used conjointly is to vary the thickness of the conducting layers to affect the light intensity in the photoactive layer and potentially increase absorption in this layer. This option has the same potential consequences as the antireflection coating. In addition to those issues, if the conductors are made thinner, this may also have a detrimental impact on PDLC or solar cell operation due to increased series resistance. Changing PDLC thickness may have some interesting advantages as it should affect the reflectivity of the layer and vary the wavelength range over which this layer can fully randomize the incoming light. These aspects can be improved with thicker PDLC layers but eventually total transmission, transmission flatness and ON state clarity will suffer. Figure 7.2 summarizes these tradeoffs and presents several additional considerations.

Change Aspect	Thicker PDLC	Thicker absorber	AR coating	Thicker contacts
Power generation	Positive effect	Positive effect	Positive effect	Positive effect
Transmission	Negative effect	Negative effect	Positive effect	Negative effect
Transmission color flatness	Negative effect	Negative effect	No effect or unknown	Negative effect
ON/OFF trans. Contrast	Mixed effect	Negative effect	No effect or unknown	Negative effect
Privacy	Positive effect	Positive effect	No effect or unknown	Positive effect
ON state clarity	Negative effect	No effect or unknown	No effect or unknown	No effect or unknown
Angle selectivity	No effect or unknown	Mixed effect	Negative effect	Mixed effect
ON state voltage	Negative effect	No effect or unknown	No effect or unknown	Positive effect

Figure 7.2: Potential avenues for optimization of the switchable solar cell device based on PDLC scatterer described in Chapter 6.

7.2. Improvement of model for absorption with scattering layers

Improving the scattering model presented in Chapter 5 is another potential avenue for future research. One weakness of the model presented in Chapter 5 is that it is not fully general in that the model considers only a single scattering layer. Additional layers could be incorporated with a matrix transfer method. In this formulation, just as sets of coherent layers were treated as effective interfaces when calculating optical coefficients for structures containing incoherent layers, stacks of mixed coherent and incoherent layers would be treated as effective interfaces between scattering layers. Calculation of these matrix elements would require additional computation. When light is

scattered from a scattering layer, s'_1 , with effective index ensemble described by $P_{s'_1}(n_{eff})$ into a second scattering layer, s'_2 , with effective index ensemble $P_{s'_2}(n_{eff})$, a joint average must be taken over both ensembles when calculating reflection transmission or absorption. For instance, the reflection between these two scattering layers would be given as:

$$\begin{aligned} & \langle R_{diff,s'_1s'_2} \rangle_{neff} \\ &= \int_0^\infty \int_0^\infty P_{s'_1}(n_{eff,s'_1}) P_{s'_2}(n_{eff,s'_2}) R_{diff,s'_1s'_2}(n_{eff,s'_1}, n_{eff,s'_2}) dn_{eff,s'_1} dn_{eff,s'_2} \end{aligned} \quad (7.1a)$$

$$\begin{aligned} & \times R_{diff,s'_1s'_2}(n_{eff,s'_1}, n_{eff,s'_2}) \\ &= \int_0^{\pi/2} R_{s'_1s'_2}(\theta_{s'_1}, n_{eff,s'_1}, n_{eff,s'_2}) \cos(\theta_{s'_1}) \sin(\theta_{s'_1}) d\theta_{s'_1}. \end{aligned} \quad (7.1b)$$

The rest of the calculations proceed in direct analogy to the matrix transfer method used for incoherent layers.

7.3. Integrating sphere measurement with liquid immersion

Going forward, the experimental setups described in Chapter 3 could also be used to generate a novel integrating sphere measurement that uses isotropic illumination of the integrating sphere and a transparent spherical liquid immersion vessel to create ideal light coupling conditions. This technique would enable new measurements of absorbing structures to allow researchers to separate the absorbing structure from any specific light trapping

structure, which is typically needed to couple light into the modes of the absorber. We refer to this measurement as diffuse absorptivity under liquid immersion.

Figure 7.3 shows a schematic view of the diffuse absorptivity liquid immersion experiment. Light entering the sphere gets fully randomized by the Lambertian surface coating the inside of the sphere. The light then diffusely illuminates the sample. As shown, the sample is rotated such that its surface is normal to the illumination spot on the integrating sphere sidewall. This prevents light from preferentially coming from one direction, which would cause the assumption of uniform illumination to be broken. It should be noted that this configuration also differs from absorption measurements discussed in Chapter 3 in that it requires only one open port in the sphere. Because the diffuse intensity in the integrating sphere is non-linear with the area of the integrating sphere openings, a significantly higher signal is produced in comparison to the typical absorption measurement. A photograph of the immersion sphere is shown in the inset of Figure 7.3. The hollow glass sphere is screwed on to a post that attaches to the top of the sphere. The holder is made completely of Teflon, a highly reflective (>95%) material used in commercial integrating spheres that approximates Lambertian reflectance.

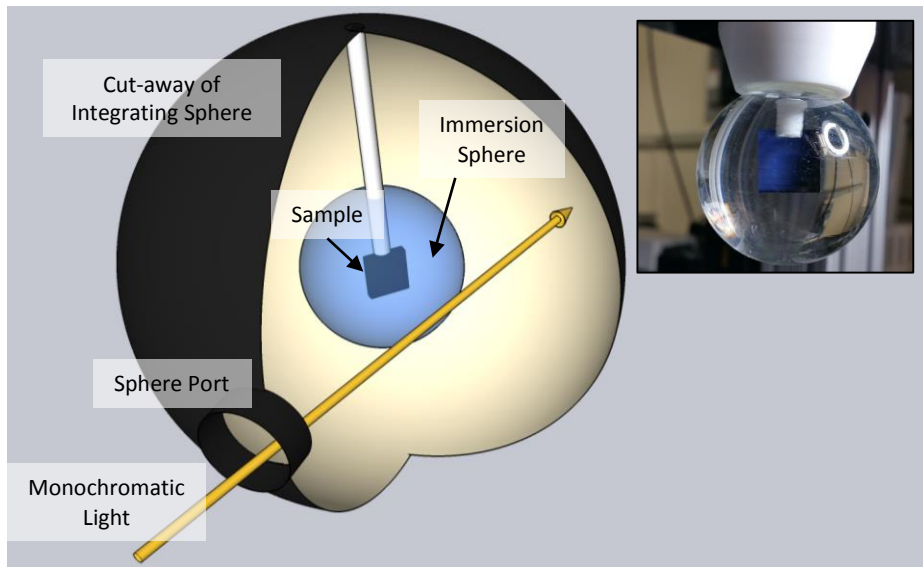


Figure 7.3: Schematic view of the diffuse absorptivity liquid immersion experiment. The integrating sphere is partially cut away to reveal the inside. Monochromatic light enters the sphere through a small opening (port). The beam avoids the immersion sphere in the center of the larger integrating sphere and strikes the back wall, scattering in all directions. The sample is held in the center of the immersion sphere with its surface parallel to the illumination spot on the integrating sphere sidewall, thus avoiding direct illumination of the sample. The inset shows an image of the actual sample holder.

Because the sample is diffusely illuminated, the actual absorption signal is dependent both on the intrinsic absorptivity of the sample and the area of the sample. Because the effect on absorption of changing the area can be predicted and measured, this area dependence can be used to improve measurement accuracy allowing for regression analysis of absorption with area to uncover the underlying absorptivity. A single measurement of diffuse

absorptivity is performed in three stages. First, the optical intensity in the integrating sphere is measured with no sample in order to normalize the later signals. Intensity in the integrating sphere is then measured for a set of samples of varying area and known absorptivity. In these experiments, silicon may be used because it has very well characterized optical properties. The diffuse absorptivity of a silicon wafer in the visible spectrum can be calculated as:

$$\alpha_{ref} = 2 \int_0^{\pi/2} T(\theta) \sin(\theta) \cos(\theta) d\theta , \quad (7.2)$$

where T is the transmission into the sample based on Fresnel equations (visible light will be completely absorbed), θ is the incident angle from normal and the cosine factor arises from the assumption of complete randomization. Using Eq. 7.2, the diffuse absorptivity of an unknown material can be found by measuring the intensity in the integrating sphere while varying the sample area. The actual absorptivity then comes from comparing the normalized, measured signals with the reference sample to the normalized, measured signals with the material of unknown absorptivity.

The actual calculation relies on a detail balance between the photons entering and exiting (note: exiting includes absorption) the integrating sphere.

That is:

$$P_0 = P_0 \alpha'_w + B(\alpha_w A_w + \alpha_p A_p + \alpha_m A_m) , \quad (7.3)$$

where P_0 is the initial power entering the system, α'_w is the fractional power loss at the first reflection from the integrating sphere wall (note prime used here to denote initial specular illumination), B is the diffuse intensity inside the sphere (power per unit area per unit solid angle integrated over all angles), α_i is the diffuse absorptivity of the side walls ($i = w$), ports (p), and measured material (m), which is either a reference sample, an unknown sample or air (*i.e.* no sample and $\alpha_m = 0$), respectively, and A_i is the corresponding area. Here the relative value of B is the actual quantity measured by a detector (the absolute value of B is given by the diffuse responsivity of the detector). Defining B_i as the diffuse intensity with either nothing, the reference material, or an unknown sample respectively, and realizing that all terms in Eq. 7.3 are constants for all samples except for α_m and A_m , a relationship between B and A_m can be found as:

$$\begin{aligned}
 & P_0\alpha'_w + B_0(\alpha_w A_w + \alpha_p A_p) \\
 & = P_0\alpha'_w + B_{ref,sam}(\alpha_w A_w + \alpha_p A_p + \alpha_{ref,sam}A_{ref,sam}),
 \end{aligned} \tag{7.4a}$$

and with some rearranging of terms:

$$\frac{B_0}{B_{ref,sam}} = \frac{\alpha_{ref,sam}A_{ref,sam}}{\alpha_w A_w + \alpha_p A_p} + 1. \tag{7.4b}$$

The derivative of $\frac{B_0}{B_{ref,sam}}$ with respect to $A_{ref,sam}$ gives the relative diffuse absorptivity of the reference or the sample respectively. With the diffuse

absorptivity of the reference known, the diffuse absorptivity of the sample can be calculated as:

$$\alpha_{sam} = \frac{\frac{d}{dA_{sam}} \left(\frac{B_0}{B_{sam}} \right)}{\frac{d}{dA_{ref}} \left(\frac{B_0}{B_{ref}} \right)} \alpha_{ref} . \quad (7.5)$$

Appendices

APPENDIX A: Chopper driver source code

Main.c

```
/* Device header file */
#if defined(__XC16__)
#include <xc.h>
#elif defined(__C30__)
#if defined(__PIC24E__)
#include <p24Exxxx.h>
#elif defined (__PIC24F__) || defined (__PIC24FK__)
#include <p24Fxxx.h>
#elif defined(__PIC24H__)
#include <p24Hxxx.h>
#endif
#endif
#endif

#include <stdint.h> /* Includes uint16_t definition */
#include <stdbool.h> /* Includes true/false definition */

#include "system.h" /* System funct/params, like osc/peripheral config */
#include "user.h" /* User funct/params, such as InitApp */
#include "SPI.h"
#include "WS2812.h"
#include "PinDefs.h"
#include "WS2812_Lookup.h"
#include "QuadEncoder.h"
#include "PWM.h"
extern int TMR1Flag = 0;

const unsigned int RedVal[6] = {0, 85, 0, 168, 255, 200};
const unsigned int GreenVal[6] = {0, 85, 128, 84, 0, 160};
const unsigned int BlueVal[6] = {255, 85, 0, 0, 0, 0};

/*****/
/* Global Variable Declaration */
/*****/
void Binary2BCD(char BCD[4], unsigned int num);

/*****/
/* Main Program */
/*****/
```

```

int16_t main(void) {
    /* Configure the oscillator for the device */
    ConfigureOscillator();

    /* Initialize IO ports and peripherals */
    InitApp();
    _T1IF = 0;
    _T1IE = 1;
    TMR1 = 0;
    PR1 = 0x7A12;
    T1CONbits.TCKPS = 1; //prescaler 2=64
    T1CONbits.TON = 1;

    _TRISA0 = 0;
    _LATA0 = 1;

    unsigned int count = 2;

    unsigned int toggle = 1;
    int PMWcount = 0x03FF;
    unsigned int PMWrange = 0b001000;
    unsigned int DownCount = 0;
    unsigned int PauseCount = 0;
    char thisone[4];
    Binary2BCD(thisone, 1111);
    Setup_WS2812_Lookup(125);
    while (1) {
        if (TMR1Flag) {
            TMR1Flag = 0;
            int go = ParseQuadEncoder();
            if (!_Button1) {
                // if (PauseCount == 10) {
                PauseCount = 0;
                switch (PMWrange) {
                    case 0b001000:
                        PMWcount++;
                        break;
                    case 0b010000:
                        PMWcount += 3;
                        break;
                    case 0b100000:
                        PMWcount += 15;
                        break;
                    case 0b000100:
                        PMWcount--;
                        break;
                    case 0b000010:

```

```

        PMWcount -= 3;
        break;
    case 0b000001:
        PMWcount -= 15;
    }

    DownCount++;
    if (0b111000 & PMWrange) {
        switch (DownCount) {
            case 20:
                PMWrange <<= 1;
                break;
            case 40:
                PMWrange <<= 1;
                break;
        }
    } else if (0b111 & PMWrange) {
        switch (DownCount) {
            case 20:
                PMWrange >>= 1;
                break;
            case 40:
                PMWrange >>= 1;
                break;
        }
    }
    if (0x0FFF < PMWcount) {
        PMWcount = 0x0FFF;
    } else if (0 >= PMWcount) {
        PMWcount = 1;
    }
    ChangePWM('1', 0x0FFF, PMWcount);
} else {
    DownCount = 0;
    PauseCount = 0;
}
if (go > 0) {
    if (_LATA0) {
        _LATA0 = 0;
        if (count == 5) {
            count = 0;
        } else {
            count++;
        }
        Write_WS2812_Lookup(toggle, RedVal[count], GreenVal[count],
BlueVal[count]);
    }
}

```

```

    } else {
        _LATA0 = 1;
    }
    PMWrange = 0b001000;
    PMWcount = PMWcount + 3;
    ChangePWM('1', 0x0FFF, PMWcount);
} else if (go < 0) {
    if (_LATA0) {
        _LATA0 = 0;
        if (count == 0) {
            count = 5;
        } else {
            count--;
        }
        Write_WS2812_Lookup(toggle,          RedVal[count],          GreenVal[count],
BlueVal[count]);

    } else {
        _LATA0 = 1;
    }

    PMWrange = 0b000100;
    PMWcount = PMWcount - 3;
    ChangePWM('1', 0x0FFF, PMWcount);
}
}
}
}

void Binary2BCD(char BCD[4], unsigned int num) {
    unsigned int temp = 0;

    temp = num % 10;
    BCD[0] = temp;
    num -= temp;
    temp = (num % 100);
    BCD[1] = temp / 10;
    num -= temp;
    temp = (num % 1000);
    BCD[2] = temp / 100;
    num -= temp;
    temp = (num % 10000);
    BCD[3] = temp / 1000;

}

```

Configuration_bits.c

```

/*****
/* Files to Include
/*****

/* Device header file */
#if defined(__XC16__)
    #include <xc.h>
#elif defined(__C30__)
    #if defined(__PIC24E__)
        #include <p24Exxxx.h>
    #elif defined (__PIC24F__) || defined (__PIC24FK__)
        #include <p24Fxxx.h>
    #elif defined(__PIC24H__)
        #include <p24Hxxx.h>
    #endif
#endif

/*****
/* Configuration Bits
/*
/* This is not all available configuration bits for all PIC24 devices.
/* Refer to the PIC24 device specific .h file in the compiler
/* support \PIC24x\h (x=F,H,E) directory for complete options specific to the
/* selected device. For additional information about what the hardware
/* configurations mean in terms of device operation, refer to the device
/* datasheet 'Special Features' chapter.
/*
/* A feature of MPLAB X is the 'Generate Source Code to Output' utility in
/* the Configuration Bits window. Under Window > PIC Memory Views >
/* Configuration Bits, a user controllable configuration bits window is
/* available to Generate Configuration Bits source code which the user can
/* paste into this project.
/*****

// PIC24FJ64GB002 Configuration Bit Settings

// 'C' source line config statements

#include <xc.h>

// CONFIG4
#pragma config DSWDTPS = DSWDTPSF // DSWDT Postscale Select (1:2,147,483,648
(25.7 days))

```

```

#pragma config DSWDTOSC = LPRC // Deep Sleep Watchdog Timer Oscillator Select
(DSWDT uses Low Power RC Oscillator (LPRC))
#pragma config RTCOSC = LPRC // RTCC Reference Oscillator Select (RTCC uses
Low Power RC Oscillator (LPRC))
#pragma config DSBOREN = ON // Deep Sleep BOR Enable bit (BOR enabled in
Deep Sleep)
#pragma config DSWDTEN = OFF // Deep Sleep Watchdog Timer (DSWDT
disabled)

// CONFIG3
#pragma config WFPF = WFPF0 // Write Protection Flash Page Segment Boundary
(Page 0 (0x0))
#pragma config SOSSEL = IO // Secondary Oscillator Pin Mode Select (SOSC pins
have digital I/O functions (RA4, RB4))
#pragma config WUTSEL = LEG // Voltage Regulator Wake-up Time Select (Default
regulator start-up time used)
#pragma config WPDIS = WPEN // Segment Write Protection Disable (Segmented
code protection enabled)
#pragma config WPCFG = WPCFGDIS // Write Protect Configuration Page Select (Last
page and Flash Configuration words are unprotected)
#pragma config WPEND = WPENDMEM // Segment Write Protection End Page Select
(Write Protect from WFPF to the last page of memory)

// CONFIG2
#pragma config POSCMOD = NONE // Primary Oscillator Select (Primary Oscillator
disabled)
#pragma config I2C1SEL = PRI // I2C1 Pin Select bit (Use default SCL1/SDA1 pins for
I2C1 )
#pragma config IOL1WAY = ON // IOLOCK One-Way Set Enable (Once set, the
IOLOCK bit cannot be cleared)
#pragma config OSCIOFNC = ON // OSCO Pin Configuration (OSCO pin functions
as port I/O (RA3))
#pragma config FCKSM = CSDCMD // Clock Switching and Fail-Safe Clock Monitor
(Sw Disabled, Mon Disabled)
#pragma config FNOSC = FRCPLL // Initial Oscillator Select (Fast RC Oscillator with
Postscaler and PLL module (FRCPLL))
#pragma config PLL96MHZ = ON // 96MHz PLL Startup Select (96 MHz PLL
Startup is enabled automatically on start-up)
#pragma config PLLDIV = NODIV // USB 96 MHz PLL Prescaler Select (Oscillator
input used directly (4 MHz input))
#pragma config IESO = ON // Internal External Switchover (IESO mode (Two-
Speed Start-up) enabled)

// CONFIG1
#pragma config WDTPS = PS32768 // Watchdog Timer Postscaler (1:32,768)
#pragma config FWPSA = PR128 // WDT Prescaler (Prescaler ratio of 1:128)

```

```

#pragma config WINDIS = OFF      // Windowed WDT (Standard Watchdog Timer
enabled,(Windowed-mode is disabled))
#pragma config FWDTEN = OFF      // Watchdog Timer (Watchdog Timer is disabled)
#pragma config ICS = PGx1       // Emulator Pin Placement Select bits (Emulator
functions are shared with PGEC1/PGED1)
#pragma config GWRP = OFF       // General Segment Write Protect (Writes to program
memory are allowed)
#pragma config GCP = OFF        // General Segment Code Protect (Code protection is
disabled)
#pragma config JTAGEN = OFF     // JTAG Port Enable (JTAG port is disabled)

```

interrupts.c

```

/*****
/* Files to Include
*****/

/* Device header file */
#if defined(__XC16__)
#include <xc.h>
#elif defined(__C30__)
#if defined(__PIC24E__)
#include <p24Exxxx.h>
#elif defined (__PIC24F__) || defined (__PIC24FK__)
#include <p24Fxxx.h>
#elif defined(__PIC24H__)
#include <p24Hxxx.h>
#endif
#endif

#include <stdint.h>    /* Includes uint16_t definition */
#include <stdbool.h>   /* Includes true/false definition */

extern int TMR1Flag;

void __attribute__((interrupt, no_auto_psv)) _T1Interrupt(void) {
    // _LATA0 ^= 1;
    if (TMR1Flag) {
        //TMR1Flag=0;

```

```

    } else {
        TMR1Flag = 1;

    }

    _T1IF = 0;
}

```

IOPorts.h

```

#ifndef IOPORTS_H
#define IOPORTS_H

#ifdef __cplusplus
extern "C" {
#endif

#include <xc.h>
extern int FirstRun;
int IOPort_Init(char PortLetter, int OutPortFlags, int InPortFlags );

void SetRPOut(int PinNum, int SetNum);

#ifdef __cplusplus
}
#endif

#endif /* IOPORTS_H */

```

IOPorts.c

```

#include <stdint.h>
#include "IOPorts.h"
#include <xc.h>
extern int FirstRun=0;

int IOPort_Init(char PortLetter, int OutPortFlags, int InPortFlags) {
    if (FirstRun == 0) {
#ifdef PORTA
        TRISA = 0; //All Output
#endif
#ifdef PORTB

```

```

    TRISB = 0; //All Output
#endif
#ifdef PORTC
    TRISC = 0; //All Output
#endif
#ifdef PORTD
    TRISD = 0; //All Output
#endif
    FirstRun = 1;
}

#ifdef PORTA
    if ((PortLetter == 'A') || (PortLetter == 'a')) {
        TRISA &= (!OutPortFlags);
        TRISA |= (InPortFlags);
        return 1;
    }
#endif
#ifdef PORTB
    if ((PortLetter == 'B') || (PortLetter == 'b')) {
        TRISB &= (!OutPortFlags);
        TRISB |= (InPortFlags);
        return 1;
    }
#endif
#ifdef PORTC
    if ((PortLetter == 'C') || (PortLetter == 'c')) {
        TRISC &= (!OutPortFlags);
        TRISC |= (InPortFlags);
        return 1;
    }
#endif
#ifdef PORTD
    if ((PortLetter == 'D') || (PortLetter == 'd')) {
        TRISD &= (!OutPortFlags);
        TRISD |= (InPortFlags);
        return 1;
    }
#endif
    return 0;
}

void SetRPOut(int PinNum, int SetNum) {
    if (8 <= PinNum) { //>=8
        if (12 <= PinNum) { //>=12

```

```

if (14<= PinNum) {/=14
    if (0b11111111 & PinNum) {/=16
        _RP15R = SetNum;
    } else {
        _RP14R = SetNum;
    }
} else {/=14>x>=12
    if (13 == PinNum) {/=13
        _RP13R = SetNum;
    } else {/=12
        //no 12
    }
}
} else {/=12>x>=8
    if (10<= PinNum) {/=10
        if (11== PinNum) {/=11
            _RP11R = SetNum;
        } else {/=10
            _RP10R = SetNum;
        }
    } else {/=10>x>=8
        if (9 == PinNum) {/=9
            _RP9R = SetNum;
        } else {/=8
            _RP8R = SetNum;
        }
    }
}
} else {/=8
    if (4<= PinNum) {/=8>x>=4
        if (6<= PinNum) {/=8>=x>6
            if (7 == PinNum) {/=7
                _RP7R = SetNum;
            } else {
                _RP6R = SetNum;
            }
        } else {/=6>x>=4
            if (5 == PinNum) {/=5
                _RP5R = SetNum;
            } else {/=4
                _RP4R = SetNum;
            }
        }
    }
} else {/=4>x
    if (2<= PinNum) {/=4>x>=2
        if (3== PinNum) {/=3
            _RP3R = SetNum;

```



```

* 22 RB11/RP11 = SCK1
* 23 Vusb    = x
* 24 RB13/RP13 = CS1
* 25 RB14/RP14 =
* 26 RB15/RP15 =
* 27 Vss     = x
* 28 Vdd     = x
*/

#define _LED      _LATA0
#define _LED_TRIS _TRISA0

#define _PMW1_RP  6

#define _QE1A     _RA2
#define _QE1A_TRIS _TRISA2

#define _QE1B     _RA3
#define _QE1B_TRIS _TRISA3

#define _Button1  _RA4
#define _Button1_TRIS _TRISA4

#define _SDI1_RP   8

#define _SSEN_RPPort 9

#define _SDO1_RPPort 10

#define _SCK1OUT_RPPort 11

#define __CS1      _LATB13
#define __CS1_TRIS _TRISB13

#define U1RX_RP    2

#define U1TX_RP    RPOR1bits.RP3R
#define U1TX_RPval 3

#define U2RX_RP    14

#define U2TX_RP    RPOR7bits.RP15R
#define U2TX_RPval 5

```

```

#ifdef __cplusplus
}
#endif

#endif /* PINDEFS_H */

```

PWM.h

```

#ifndef PWM_H
#define PWM_H

#ifdef __cplusplus
extern "C" {
#endif

extern void InitPWM(char PWMnum, unsigned char PinNum, unsigned int Period,
unsigned int Ontime);

extern void ChangePWM(char PWMnum, unsigned int Period, unsigned int Ontime);

#ifdef __cplusplus
}
#endif

#endif /* PWM_H */

```

PWM.c

```

#include "PWM.h"
#include <stdint.h>
#include <xc.h>

extern void InitPWM(char PWMnum, unsigned char PinNum, unsigned int Period,
unsigned int Ontime) {
    T4CON = 0x00;
    _T4IF = 0;

    TMR4 = 0x0000;
    PR4 = 0x5525;
    T4CONbits.TCKPS = 0;
    T4CONbits.TON = 1;
}

```

```

switch (PWMnum)
{
    case '1':
        SetRPOut(PinNum, 18);
        OC1CON1 = 0x0000;
        OC1CON2 = 0x0000;
        OC1CON1bits.OCTSEL = 0b111; //Sets timer source to system clock

        OC1R = Ontime;
        OC1RS = Period;
//     OC1CON2bits.OCTRIG = 0; //Required for PWM. Sets sync
        OC1CON2bits.SYNCSEL = 0x1F; //Required for PWM. Set sync source to self
        OC1CON1bits.OCM = 0b110;
//     OC1CON1bits.TRIGMODE=0;
        _TRISB4=0;
        break;
    case '2':
        SetRPOut(PinNum, 19);
        OC2CON1 = 0x0000;
        OC2CON2 = 0x0000;
        OC2CON1bits.OCTSEL = 0b111; //Sets timer source to system clock

        OC2R = Ontime;
        OC2RS = Period;
//     OC1CON2bits.OCTRIG = 0; //Required for PWM. Sets sync
        OC2CON2bits.SYNCSEL = 0x1F; //Required for PWM. Set sync source to self
        OC2CON1bits.OCM = 0b110;
//     OC1CON1bits.TRIGMODE=0;
        _TRISB7=0;
        break;
}
}

extern void ChangePWM(char PWMnum, unsigned int Period, unsigned int Ontime)
{
    switch (PWMnum)
    {
        case '1':
            OC1R = Ontime;
            OC1RS = Period;
            break;
        case '2':
            OC2R = Ontime;
            OC2RS = Period;
            break;
    }
}

```

```

}
}

void __attribute__((__interrupt__, __shadow__)) _OC1Interrupt(void)
{
/* Interrupt Service Routine code goes here */
_OC1IF = 0; //Reset Timer1 interrupt flag and Return from ISR
}

```

QuadEncoder.h

```

#ifndef QUADENCODER_H
#define QUADENCODER_H

#ifdef __cplusplus
extern "C" {
#endif

typedef struct{
    unsigned int A    :2;
    unsigned int B    :2;
    unsigned int DataReady :1;
}QuadEncoder_struct;

void SetupQuadEncoder();
int ParseQuadEncoder();

#ifdef __cplusplus
}
#endif

#endif /* QUADENCODER_H */

```

QuadEncoder.c

```

#include <stdint.h>
#include "QuadEncoder.h"
#include "PinDefs.h"
#include <xc.h>
#include "uart2.h"

```

```

#define _REPORT_UART

QuadEncoder_struct QuadEncoder = {0, 0, 0};
unsigned int LastButton;
unsigned int ButtonReady=0;

void SetupQuadEncoder() {
    _QE1A_TRIS = 1;
    _QE1B_TRIS = 1;

    //CNEN2bits.CN29IE = 1;
    CNPU2bits.CN29PUE = 1;
    CNEN2bits.CN30IE = 1;
    CNPU2bits.CN30PUE = 1;

    IFS1bits.CNIF = 0;

    IPC4bits.CNIP = 1;

    IEC1bits.CNIE = 1;

    QuadEncoder.A = _QE1A;
    QuadEncoder.B = _QE1B;

    QuadEncoder.DataReady = 0;
}

void SetupButton() {
    _Button1_TRIS = 1;
    LastButton = _Button1;

    //CNEN2bits.CN29IE = 1;
    _CN0PUE = 1;
    _CNIF = 0;
    _CN0IE = 1;
    _CNIP = 1;
}

void __attribute__((interrupt, no_auto_psv)) _CNInterrupt(void) {
    if (LastButton != _Button1)
    {
        LastButton=_Button1;
        ButtonReady=1;
    }
}

```

```

}
else if (_QE1A != (QuadEncoder.A & 0x01)) {
    QuadEncoder.A = (QuadEncoder.A << 1) | _QE1A;
    QuadEncoder.B = (QuadEncoder.B << 1) | _QE1B;
    QuadEncoder.DataReady = 1;
}

IFS1bits.CNIF = 0;
}

int ParseButton()
{
    if(ButtonReady&!LastButton)
    {
        return 1;
        ButtonReady=0;
    }
    return 0;
}

int ParseQuadEncoder() {
    int out = 0;
    if (QuadEncoder.DataReady) {

        unsigned char QuadCombined = 0;
        QuadCombined |= (QuadEncoder.A);
        QuadCombined |= (QuadEncoder.B << 2);

        switch (QuadCombined) {
            case 0:
#ifdef _REPORT_UART
                TXPutStr("E0\n", 3, 1);
#endif
                out = 0;
                break;
            case 1:
#ifdef _REPORT_UART
                TXPutStr("1\n", 2, 1);
#endif
                out = 1;
                break;
            case 2:
#ifdef _REPORT_UART

```

```

        TXPutStr("2\n", 2, 1);
#endif
        out = 0;
        break;
    case 3:
#ifdef _REPORT_UART
        TXPutStr("E3\n", 3, 1);
#endif
        out = -1;
        break;
    case 4:
#ifdef _REPORT_UART
        TXPutStr("E4\n", 3, 1);
#endif
        out = 0;
        break;
    case 5:
#ifdef _REPORT_UART
        TXPutStr("5\n", 2, 1);
#endif
        out = -1;
        break;
    case 6:
#ifdef _REPORT_UART
        TXPutStr("6\n", 2, 1);
#endif
        out = 0;
        break;
    case 7:
#ifdef _REPORT_UART
        TXPutStr("E7\n", 3, 1);
#endif
        out = 0;
        break;
    case 8:
#ifdef _REPORT_UART
        TXPutStr("E8\n", 3, 1);
#endif
        out = 0;
        break;
    case 9:
#ifdef _REPORT_UART
        TXPutStr("9\n", 2, 1);
#endif
        out = 0;
        break;
    case 10:

```

```

#ifdef _REPORT_UART
    TXPutStr("10\n", 3, 1);
#endif
    out = 0;
    break;
case 11:
#ifdef _REPORT_UART
    TXPutStr("E11\n", 4, 1);
#endif
    out = 0;
    break;
case 12:
#ifdef _REPORT_UART
    TXPutStr("E12\n", 4, 1);
#endif
    out = 0;
    break;
case 13:
#ifdef _REPORT_UART
    TXPutStr("13\n", 3, 1);
#endif
    out = -1;
    break;
case 14:
#ifdef _REPORT_UART
    TXPutStr("14\n", 3, 1);
#endif
    out = 0;
    break;
case 15:
#ifdef _REPORT_UART
    TXPutStr("E15\n", 4, 1);
#endif
    out = 0;
    break;
default:
    out = -3;
    break;
}
QuadEncoder.DataReady = 0;
}
return out;
}

```

SPI.h

```
#ifndef SPI_H
```

```

#define SPI_H

#ifdef __cplusplus
extern "C" {
#endif

    void InitSPI1_Mast(int DataInPort, int DataOutPort, int SelectPort, int ClockOutPort);

    void WriteSPI1(unsigned int word);

#ifdef __cplusplus
}
#endif

#endif /* SPI_H */

```

SPI.c

```

#include <stdint.h>
#include "SPI.h"
#include "IOPorts.h"
#include <xc.h>

unsigned int SwipeNum = 0;
unsigned int Num = 0;

void InitSPI1_Mast(int DataInPort, int DataOutPort, int SelectPort, int ClockOutPort) {
    IFS0bits.SPF1IF = 0;
    IEC0bits.SPI1IE = 1;
    IPC2bits.SPI1IP = 6; //Interrupts

    SPI1CON1bits.MSTEN = 1;

    _SDI1R = DataInPort;
    if (ClockOutPort == -1) {
        SPI1CON1bits.DISSCK = 1;
    } else {
        SPI1CON1bits.DISSCK = 0;
        SetRPOut(ClockOutPort, 8);
    }
}

```

```

if (DataOutPort == -1) {
    SPI1CON1bits.DISSDO = 1;
} else {
    SPI1CON1bits.DISSDO = 0; //sd used
    SetRPOut(DataOutPort, 7);
}

if (SelectPort == -1) {
    SPI1CON1bits.SSEN = 1;
} else {
    SPI1CON1bits.SSEN = 0; //sd used
    SetRPOut(SelectPort, 9);
}
// SPI1CON1bits.SSEN = 0;
SPI1CON1bits.MODE16 = 1; //16 bit mode
SPI1CON1bits.SMP = 1; //Input change at mid time
SPI1CON1bits.CKP = 1; //Clock is normally low
SPI1CON1bits.CKE = 0; //#####
SPI1CON1bits.PPRE = 0b11; //1x slower
SPI1CON1bits.SPRE = 2; //additional 6x slower

SPI1CON2bits.SPIFE = 0;

SPI1CON2bits.FRMEN = 1;
SPI1CON2bits.SPIFPOL = 1;

SPI1STATbits.SISEL = 0b110; //interrupt when last byte out of FIFO;

SPI1STATbits.SPIROV = 0;
SPI1CON2bits.SPIBEN = 1;
SPI1STATbits.SPIEN = 1;

IFS0bits.SPF1IF = 0;
//WriteSPI1(SwipeNum);
//WriteSPI1((0b0000000000000000)|0b01110111);
}

void WriteSPI1(unsigned int word) {

    SPI1BUF = word;
}

```

system.h

```
/******  
/* System Level #define Macros */  
/******  
  
/* Microcontroller MIPs (FCY) */  
#define SYS_FREQ 3200000L  
#define FCY SYS_FREQ/2  
/******  
/* System Function Prototypes */  
/******  
void ConfigureOscillator(void); /* Handles clock switching/osc initialization */
```

system.c

```

/*****
/* Files to Include
*****/

/* Device header file */
#if defined(__XC16__)
#include <xc.h>
#elif defined(__C30__)
#if defined(__PIC24E__)
#include <p24Exxxx.h>
#elif defined (__PIC24F__) || defined (__PIC24FK__)
#include <p24Fxxx.h>
#elif defined(__PIC24H__)
#include <p24Hxxx.h>
#endif
#endif

#include <stdint.h> /* For uint32_t definition */
#include <stdbool.h> /* For true/false definition */

#include "system.h" /* variables/params used by system.c */

/*****
/* System Level Functions
*/
/* Custom oscillator configuration funtions, reset source evaluation */
/* functions, and other non-peripheral microcontroller initialization */
/* functions get placed in system.c
*/
*****/

/* Refer to the device Family Reference Manual Oscillator section for
information about available oscillator configurations. Typically
this would involve configuring the oscillator tuning register or clock
switching using the compiler's __builtin_write_OSCCON functions.
Refer to the C Compiler for PIC24 MCUs and dsPIC DSCs User Guide in the
compiler installation directory /doc folder for documentation on the
__builtin functions. */

void ConfigureOscillator(void) {

#if 0

/* Disable Watch Dog Timer */
RCONbits.SWDTEN = 0;

```

```

/* When clock switch occurs switch to Prim Osc (HS, XT, EC)with PLL */
__builtin_write_OSCCONH(0x03); /* Set OSCCONH for clock switch */
__builtin_write_OSCCONL(0x01); /* Start clock switching */
while (OSCCONbits.COSC != 0b011);

/* Wait for Clock switch to occur */
/* Wait for PLL to lock, if PLL is used */
/* while(OSCCONbits.LOCK != 1); */

#endif

}

```

uart2.h

```

#ifndef UART2_H
#define UART2_H

// External oscillator frequency
#define SYSCLK      32000000
#define FCY        16000000

/*****
 * DEFINITIONS
 *****/

// Baudrate
#define BAUDRATE      9600
#define TXBUFFERSIZE  50
#define RXBUFFERSIZE  50

/*****
 * U2BRG register value and baudrate mistake calculation
 *****/
#define BAUDRATEREG FCY/4/BAUDRATE-1

/*****
 * Function: UART1Init
 *
 * Precondition: None.
 *
 * Overview: Setup UART2 module.
 *
 * Input: None.
 *
 * Output: None.
 *****/

```

```

*****/
extern void InitUART(char UARTnum);

/*****
* Function: TXPutChar
*
* Precondition: InitUART1 must be called before.
*
* Overview: Puts a char in TX Buffer. Characters are moved to hardware buffer
* when empty.
*
* Input: Byte to be sent.
*
* Output: Bool. If Tx Buffer is full
*
*****/
extern void TXPutChar(char txc, char UARTnum);

/*****
* Function: TXPutStr
*
* Precondition: InitUART1 must be called before.
*
* Overview: Puts a char in TX Buffer. Characters are moved to hardware buffer
* when empty.
*
* Input: Byte to be sent.
*
* Output: Bool. If Tx Buffer is full
*
*****/
extern void TXPutStr(char *str, unsigned int txcount, char UARTnum);

/*****
* Function: RXGetChar
*
* Precondition: UART2Init must be called before.
*
* Overview: Reads next char in RX Buffer.
*
* Input: None.
*
* Output: Next char.
*
*****/
extern char RXGetChar(char UARTnum);

```

```

/*****
 * Function: RXLookChar
 *
 * Precondition: UART2Init must be called before.
 *
 * Overview: Looks at next char in RX Buffer but doesn't move pointer.
 *
 * Input: None.
 *
 * Output: Next char.
 *****/
extern char RXLookChar(unsigned int LookAheadNum, char UARTnum);

/*****
 * Function: RXGetChar
 *
 * Precondition: UART2Init must be called before.
 *
 * Overview: Reads next char in RX Buffer.
 *
 * Input: None.
 *
 * Output: Next char.
 *****/
extern unsigned int RXGetStr(char *str, unsigned int rxcount, char UARTnum);

typedef struct {
    char txbuffer[TXBUFFERSIZE];
    unsigned int txputpos;
    unsigned int txgetpos;
} tx_buf_struct;

typedef struct {
    char rxbuffer[RXBUFFERSIZE];
    unsigned int rxputpos;
    unsigned int rxgetpos;
    unsigned int RXDataReady : 1;
} rx_buf_struct;

#endif

```

uart2.c

```

#include <stdint.h>
#include "uart2.h"

```

```

#include "PinDefs.h"
#include <xc.h>
tx_buf_struct tx_buf1;
rx_buf_struct rx_buf1;

tx_buf_struct tx_buf2;
rx_buf_struct rx_buf2;

//*****
//UART1 Interrupts
void __attribute__((interrupt, no_auto_psv)) _U1RXInterrupt(void) {
    char temp_c = U1RXREG;

    rx_buf1.rxbuffer[rx_buf1.rxputpos] = temp_c;
    rx_buf1.rxputpos++;

    if (rx_buf1.rxputpos == TXBUFFERSIZE) {
        rx_buf1.rxputpos = 0;
    }
    rx_buf1.RXDataReady=1;
    IFS0bits.U1RXIF = 0;
}

void __attribute__((interrupt, no_auto_psv)) _U1TXInterrupt(void) {

    while ((tx_buf1.txputpos != tx_buf1.txgetpos) && !U1STAbits.UTXBF) {
        U1TXREG = tx_buf1.txbuffer[tx_buf1.txgetpos];
        tx_buf1.txgetpos++;
        if (tx_buf1.txgetpos == TXBUFFERSIZE) {
            tx_buf1.txgetpos = 0;
        }
    }
    IFS0bits.U1TXIF = 0;
}

//*****
//UART2 Interrupts
void __attribute__((interrupt, no_auto_psv)) _U2RXInterrupt(void) {
    char temp_c = U2RXREG;

    rx_buf2.rxbuffer[rx_buf2.rxputpos] = temp_c;
    rx_buf2.rxputpos++;
}

```

```

if (rx_buf2.rxputpos == TXBUFFERSIZE) {
    rx_buf2.rxputpos = 0;
}
rx_buf2.RXDataReady=1;
IFS1bits.U2RXIF = 0;
}

void __attribute__((interrupt, no_auto_psv)) _U2TXInterrupt(void) {

while ((tx_buf2.txputpos != tx_buf2.txgetpos) && !U2STAbits.UTXBF) {
    U2TXREG = tx_buf2.txbuffer[tx_buf2.txgetpos];
    tx_buf2.txgetpos++;
    if (tx_buf2.txgetpos == TXBUFFERSIZE) {
        tx_buf2.txgetpos = 0;
    }
}
IFS1bits.U2TXIF = 0;
}

//*****
//UART IO Functions
void TXPutStr(char *str, unsigned int txcount, char UARTnum) {
    unsigned int i;
    if (UARTnum==1)
    {
        for (i = 0; i < txcount; i++) {
            tx_buf1.txbuffer[tx_buf1.txputpos] = str[i];
            tx_buf1.txputpos++;
            if (tx_buf1.txputpos == TXBUFFERSIZE) {
                tx_buf1.txputpos = 0;
            }
        }

        if (U1STAbits.TRMT) {
            unsigned int txgettemp = tx_buf1.txgetpos;
            tx_buf1.txgetpos++;
            if (tx_buf1.txgetpos == TXBUFFERSIZE) {
                tx_buf1.txgetpos = 0;
            }
            U1TXREG = tx_buf1.txbuffer[txgettemp];
        }
    }
    else if (UARTnum==2)
    {
        for (i = 0; i < txcount; i++) {
            tx_buf2.txbuffer[tx_buf2.txputpos] = str[i];

```

```

tx_buf2.txputpos++;
if (tx_buf2.txputpos == TXBUFFERSIZE) {
    tx_buf2.txputpos = 0;
}
}

if (U2STAbits.TRMT) {
    unsigned int txgettemp = tx_buf2.txgetpos;
    tx_buf2.txgetpos++;
    if (tx_buf2.txgetpos == TXBUFFERSIZE) {
        tx_buf2.txgetpos = 0;
    }
    U2TXREG = tx_buf2.txbuffer[txgettemp];
}
}
}

void TXPutChar(char txc, char UARTnum) {

    if (UARTnum==1)
    {
        tx_buf1.txbuffer[tx_buf1.txputpos] = txc;
        tx_buf1.txputpos++;

        if (tx_buf1.txputpos == TXBUFFERSIZE) {
            tx_buf1.txputpos = 0;
        }

        if (U1STAbits.TRMT) {
            unsigned int txgettemp = tx_buf1.txgetpos;
            tx_buf1.txgetpos++;
            if (tx_buf1.txgetpos == TXBUFFERSIZE) {
                tx_buf1.txgetpos = 0;
            }
            U1TXREG = tx_buf1.txbuffer[txgettemp];
        }
    }
    else if (UARTnum==2)
    {
        tx_buf2.txbuffer[tx_buf2.txputpos] = txc;
        tx_buf2.txputpos++;

        if (tx_buf2.txputpos == TXBUFFERSIZE) {
            tx_buf2.txputpos = 0;
        }

        if (U1STAbits.TRMT) {

```

```

    unsigned int txgettemp = tx_buf2.txgetpos;
    tx_buf2.txgetpos++;
    if (tx_buf2.txgetpos == TXBUFFERSIZE) {
        tx_buf2.txgetpos = 0;
    }
    U2TXREG = tx_buf2.txbuffer[txgettemp];
}
}
}

char RXGetChar(char UARTnum) {
    if (UARTnum==1)
    {
        if (rx_buf1.rxputpos != rx_buf1.rxgetpos) {
            char char_return = rx_buf1.rxbuffer[rx_buf1.rxgetpos];

            rx_buf1.rxgetpos++;
            if (rx_buf1.rxgetpos == RXBUFFERSIZE) {
                rx_buf1.rxgetpos = 0;
            }
            return char_return;
        }
    }
    else if (UARTnum==2)
    {
        if (rx_buf2.rxputpos != rx_buf2.rxgetpos) {
            char char_return = rx_buf2.rxbuffer[rx_buf2.rxgetpos];

            rx_buf2.rxgetpos++;
            if (rx_buf2.rxgetpos == RXBUFFERSIZE) {
                rx_buf2.rxgetpos = 0;
            }
            return char_return;
        }
    }
    return '\0';
}

unsigned int RXGetStr(char *str, unsigned int rxcount, char UARTnum) {
    unsigned int rx_returned = 0;

    if (UARTnum==1)
    {
        while ((rx_buf1.rxputpos != rx_buf1.rxgetpos) && (rx_returned < rxcount)) {
            str[rx_returned] = rx_buf1.rxbuffer[rx_buf1.rxgetpos];
            rx_buf1.rxgetpos++;
            if (rx_buf1.rxgetpos == RXBUFFERSIZE) {

```

```

        rx_buf1.rxgetpos = 0;
    }
    rx_returned++;
}
}
else if (UARTnum==2)
{
    while ((rx_buf2.rxputpos != rx_buf2.rxgetpos) && (rx_returned < rxcount)) {
        str[rx_returned] = rx_buf2.rxbuffer[rx_buf2.rxgetpos];
        rx_buf2.rxgetpos++;
        if (rx_buf2.rxgetpos == RXBUFFERSIZE) {
            rx_buf2.rxgetpos = 0;
        }
        rx_returned++;
    }
}
return rx_returned;
}

extern char RXLookChar(unsigned int LookAheadNum, char UARTnum)
{
    if (UARTnum==1)
    {
        unsigned int LookPos=(rx_buf1.rxgetpos+LookAheadNum);
        if(LookPos>=RXBUFFERSIZE)
        {
            LookPos-=RXBUFFERSIZE;
        }

        return rx_buf1.rxbuffer[LookPos];
    }
    if (UARTnum==2)
    {
        unsigned int LookPos=(rx_buf2.rxgetpos+LookAheadNum);
        if(LookPos>=RXBUFFERSIZE)
        {
            LookPos-=RXBUFFERSIZE;
        }

        return rx_buf2.rxbuffer[LookPos];
    }
    return '\0';
}

void InitUART(char UARTnum) {
    // This is an EXAMPLE, so brutal typing goes into explaining all bit sets

```

```

// The Explorer 16 board has a DB9 connector wired to UART2, so we will
// be configuring this port only

tx_buf1.txgetpos = 0;
tx_buf1.txputpos = 0;

rx_buf2.rxgetpos = 0;
rx_buf2.rxputpos = 0;

if((UARTnum==1)|(UARTnum>2))
{
    // configure U1MODE
    U1MODEbits.UARTEN = 0; // Bit15 TX, RX DISABLED, ENABLE at end of func
    U1MODEbits.USIDL = 0; // Bit13 Continue in Idle
    U1MODEbits.IREN = 0; // Bit12 No IR translation
    U1MODEbits.RTSMD = 1; // Bit11 Simplex Mode
    U1MODEbits.UEN = 0; // Bits8,9 TX,RX enabled, CTS,RTS not
    U1MODEbits.WAKE = 0; // Bit7 No Wake up (since we don't sleep here)
    U1MODEbits.LPBACK = 0; // Bit6 No Loop Back
    U1MODEbits.ABAUD = 0; // Bit5 No Autobaud (would require sending '55')
    U1MODEbits.RXINV = 0; // Bit4 IdleState = 1
    U1MODEbits.BRGH = 1; // Bit3 16 clocks per bit period
    U1MODEbits.PDSEL = 0; // Bits1,2 8bit, No Parity
    U1MODEbits.STSEL = 0; // Bit0 One Stop Bit

    U1BRG = BAUDRATEREG; // baud rate

    // Load all values in for U1STA SFR
    U1STAbits.UTXISEL1 = 1; //Bit15 Int when Char is transferred (1/2 config!)
    U1STAbits.UTXINV = 0; //Bit14 N/A, IRDA config
    U1STAbits.UTXISEL0 = 0; //Bit13 Other half of Bit15
    U1STAbits.UTXBRK = 0; //Bit11 Disabled
    U1STAbits.UTXEN = 0; //Bit10 TX pins controlled by periph
    U1STAbits.UTXBF = 0; //Bit9 *Read Only Bit*
    U1STAbits.TRMT = 0; //Bit8 *Read Only bit*
    U1STAbits.URXISEL = 0; //Bits6,7 Int. on character recieved
    U1STAbits.ADDEN = 0; //Bit5 Address Detect Disabled
    U1STAbits.RIDLE = 0; //Bit4 *Read Only Bit*
    U1STAbits.PERR = 0; //Bit3 *Read Only Bit*
    U1STAbits.FERR = 0; //Bit2 *Read Only Bit*
    U1STAbits.OERR = 0; //Bit1 *Read Only Bit*
    U1STAbits.URXDA = 0; //Bit0 *Read Only Bit*

```

```

IPC3bits.U1TXIP2 = 0; //Set Uart TX Interrupt Priority
IPC3bits.U1TXIP1 = 0;
IPC3bits.U1TXIP0 = 1;
IPC2bits.U1RXIP2 = 1; //Set Uart RX Interrupt Priority
IPC2bits.U1RXIP1 = 0;
IPC2bits.U1RXIP0 = 0;

U1MODEbits.UARTEN = 1; // And turn the peripheral on

U1STAbits.UTXEN = 1;

IFS0bits.U1TXIF = 0; // Clear the Transmit Interrupt Flag
IEC0bits.U1TXIE = 1; // Enable Transmit Interrupts
IFS0bits.U1RXIF = 0; // Clear the Recieve Interrupt Flag
IEC0bits.U1RXIE = 1; // Enable Recieve Interrupts

RPNR18bits.U1RXR = U1RX_RP; //UART1 receive set to RB2
U1TX_RP = U1TX_RPval; //UART1 transmit set to RB3
}
else if(UARTnum>=2)
{
    // configure U2MODE
    U2MODEbits.UARTEN = 0; // Bit15 TX, RX DISABLED, ENABLE at end of func
    U2MODEbits.USIDL = 0; // Bit13 Continue in Idle
    U2MODEbits.IREN = 0; // Bit12 No IR translation
    U2MODEbits.RTSMD = 1; // Bit11 Simplex Mode
    U2MODEbits.UEN = 0; // Bits8,9 TX,RX enabled, CTS,RTS not
    U2MODEbits.WAKE = 0; // Bit7 No Wake up (since we don't sleep here)
    U2MODEbits.LPBACK = 0; // Bit6 No Loop Back
    U2MODEbits.ABAUD = 0; // Bit5 No Autobaud (would require sending '55')
    U2MODEbits.RXINV = 0; // Bit4 IdleState = 1
    U2MODEbits.BRGH = 1; // Bit3 16 clocks per bit period
    U2MODEbits.PDSEL = 0; // Bits1,2 8bit, No Parity
    U2MODEbits.STSEL = 0; // Bit0 One Stop Bit

    U2BRG = BAUDRATEREG; // baud rate

    // Load all values in for U1STA SFR
    U2STAbits.UTXISEL1 = 1; //Bit15 Int when Char is transferred (1/2 config!)
    U2STAbits.UTXINV = 0; //Bit14 N/A, IRDA config
    U2STAbits.UTXISEL0 = 0; //Bit13 Other half of Bit15
    U2STAbits.UTXBRK = 0; //Bit11 Disabled
    U2STAbits.UTXEN = 0; //Bit10 TX pins controlled by periph
    U2STAbits.UTXBF = 0; //Bit9 *Read Only Bit*
    U2STAbits.TRMT = 0; //Bit8 *Read Only bit*
    U2STAbits.URXISEL = 0; //Bits6,7 Int. on character recieved
    U2STAbits.ADDEN = 0; //Bit5 Address Detect Disabled

```

```

U2STAbits.RIDLE = 0; //Bit4 *Read Only Bit*
U2STAbits.PERR = 0; //Bit3 *Read Only Bit*
U2STAbits.FERR = 0; //Bit2 *Read Only Bit*
U2STAbits.OERR = 0; //Bit1 *Read Only Bit*
U2STAbits.URXDA = 0; //Bit0 *Read Only Bit*

IPC7bits.U2TXIP2 = 0; //Set Uart TX Interrupt Priority
IPC7bits.U2TXIP1 = 0;
IPC7bits.U2TXIP0 = 1;
IPC7bits.U2RXIP2 = 1; //Set Uart RX Interrupt Priority
IPC7bits.U2RXIP1 = 0;
IPC7bits.U2RXIP0 = 0;

U2MODEbits.UARTEN = 1; // And turn the peripheral on

U2STAbits.UTXEN = 1;

IFS1bits.U2TXIF = 0; // Clear the Transmit Interrupt Flag
IEC1bits.U2TXIE = 1; // Enable Transmit Interrupts
IFS1bits.U2RXIF = 0; // Clear the Recieve Interrupt Flag
IEC1bits.U2RXIE = 1; // Enable Recieve Interrupts

RPINR19bits.U2RXR = U2RX_RP; //UART1 receive set to RB2
U2TX_RP = U2TX_RPval; //UART1 transmit set to RB3
}
AD1PCFGL = 0xFFFF; //set to all digital I/O
//U1TXREG = 0x55;
//_TRISB2 = 1; //configure all PortB as input
//_TRISB3 = 1; //configure all PortB as input
}

```

user.h

```

void InitApp(void); /* I/O and Peripheral Initialization */

```

user.c

```

/*****
/* Files to Include
*****/

/* Device header file */
#if defined(__XC16__)
#include <xc.h>
#elif defined(__C30__)
#if defined(__PIC24E__)
#include <p24Exxxx.h>
#elif defined (__PIC24F__) || defined (__PIC24FK__)
#include <p24Fxxx.h>
#elif defined(__PIC24H__)
#include <p24Hxxx.h>
#endif
#endif

#include <stdint.h> /* For uint32_t definition */
#include <stdbool.h> /* For true/false definition */

#include "user.h" /* variables/params used by user.c */
#include "PinDefs.h"
#include "IOPorts.h"
#include "SPI.h"
#include "QuadEncoder.h"
#include "uart2.h"
#include "PWM.h"

/*****
/* User Functions
*****/

/* <Initialize variables in user.h and insert code for user algorithms.> */
void InitApp(void)
{
/* Setup analog functionality and port direction */

InitPWM('1', _PMW1_RP, 0x0FFF, 0x03FF);
InitSPI1_Mast( _SDI1_RP, _SDO1_RPPort, _SSEN_RPPort, _SCK1OUT_RPPort);
/* Initialize peripherals */
SetupQuadEncoder();
InitUART(1);
_Button1_TRIS = 1;
_CN0PUE = 1;
}

```

WS2812.h

```
#ifndef WS2812_H
#define WS2812_H

#ifdef __cplusplus
extern "C" {
#endif

    void Write_WS2812(unsigned int LEDnum,unsigned char LEDgreen,unsigned char
LEDred,unsigned char LEDblue);

#ifdef __cplusplus
}
#endif

#endif /* WS2812_H */
```

WS2812_Lookup.h

```
#ifndef WS2812_LOOKUP_H
#define WS2812_LOOKUP_H

#ifdef __cplusplus
extern "C" {
#endif

#define MAXWS2812_LEDS 4

    void Write_WS2812_Lookup(unsigned int LEDnum,unsigned char LEDgreen,unsigned
char LEDred,unsigned char LEDblue);
    void Setup_WS2812_Lookup();
    void Setup_WS2812_Lookup(unsigned int init);

#ifdef __cplusplus
}
#endif

#endif /* WS2812_LOOKUP_H */
```

WS2812_Lookup.c

```
#include "\WS2812_Lookup.h"
```

```

#include "SPI.h"
#include <stdlib.h>
#include <xc.h>

const unsigned int WS2812LookupArray[16] = {
    0b1000100010001000,
    0b1000100010001100,
    0b1000100011001000,
    0b1000100011001100,
    0b1000110010001000,
    0b1000110010001100,
    0b1000110011001000,
    0b1000110011001100,
    0b1100100010001000,
    0b1100100010001100,
    0b1100100011001000,
    0b1100100011001100,
    0b1100110010001000,
    0b1100110010001100,
    0b1100110011001000,
    0b1100110011001100,
};
unsigned int LEDGreenArray1[MAXWS2812_LEDS];
unsigned int LEDRedArray1[MAXWS2812_LEDS];
unsigned int LEDBlueArray1[MAXWS2812_LEDS];
unsigned int LEDGreenArray2[MAXWS2812_LEDS];
unsigned int LEDRedArray2[MAXWS2812_LEDS];
unsigned int LEDBlueArray2[MAXWS2812_LEDS];

unsigned int CurrentSend;
unsigned int TotSend;

void Setup_WS2812_Lookup(unsigned int init) {
    unsigned int initTable1 = WS2812LookupArray[init & 0b1111];
    unsigned int initTable2 = WS2812LookupArray[init >> 4];
    unsigned int i = MAXWS2812_LEDS;
    while(i)
    {
        i--;
        LEDGreenArray1[i] = initTable1;
        LEDRedArray1[i] = initTable1;
        LEDBlueArray1[i] = initTable1;
    }
}

```

```

    LEDGreenArray2[i] = initTable2;
    LEDRedArray2[i] = initTable2;
    LEDBlueArray2[i] = initTable2;
}

CurrentSend = 0;
TotSend = MAXWS2812_LEDS+1;
IFS0bits.SPI1IF = 1;

}

void Write_WS2812_Lookup(unsigned int LEDnum, unsigned char LEDgreen, unsigned
char LEDred, unsigned char LEDblue) {

    LEDGreenArray1[LEDnum] = WS2812LookupArray[LEDgreen & 0b1111];
    LEDRedArray1[LEDnum] = WS2812LookupArray[LEDred & 0b1111];
    LEDBlueArray1[LEDnum] = WS2812LookupArray[LEDblue & 0b1111];

    LEDGreenArray2[LEDnum] = WS2812LookupArray[LEDgreen >> 4];
    LEDRedArray2[LEDnum] = WS2812LookupArray[LEDred >> 4];
    LEDBlueArray2[LEDnum] = WS2812LookupArray[LEDblue >> 4];

    CurrentSend =0;
    TotSend = LEDnum+1;
    IFS0bits.SPI1IF = 1;
}

void __attribute__((interrupt, no_auto_psv)) _SPI1Interrupt(void) {

    if ((CurrentSend < TotSend)&(!_SPIBEC)) {
        SPI1BUF = LEDGreenArray1[CurrentSend];
        SPI1BUF = LEDGreenArray2[CurrentSend];

        SPI1BUF = LEDRedArray2[CurrentSend];
        SPI1BUF = LEDRedArray1[CurrentSend];

        SPI1BUF = LEDBlueArray1[CurrentSend];
        SPI1BUF = LEDBlueArray2[CurrentSend];
        CurrentSend++;
    }
    IFS0bits.SPI1IF = 0;
}

```

APPENDIX B: Integrated motor controller source code

Main.c

```
#include "16F690.H"
#include "16F687_config.H"
#include "int16CXX.h" // device dependent interrupt definitions
#include "RS232Setup.h"
#include "InterruptSetup.h"

#pragma sharedAllocation

#pragma config=_INTRC_OSC_NOCLKOUT & _WDT_OFF & _PWRTE_OFF &
_MCLRE_OFF & _CP_OFF & _BOR_OFF & _IESO_OFF & _FCMEN_OFF

#define DEVICEID_CHAR1 'A'
#define DEVICEID_CHAR2 '1'

#define COMMANDSIZE 5
#define STARTCHAR '&'
#define ENDCHAR '*'
#define CONTINUECHAR ';'
#define MOTORFLAG 'M'
#define SWITCHFLAG 'S'
#define CONFIGFLAG 'C'
#define CONFIGMOTORINTERRUPTSFLAG 'T'
#define VOLTAGEFLAG 'V'
#define CONFIGSPEEDFLAG 'S'
#define CONFIGCHANGERABIEFLAG 'R'
#define CONFIGPRESCALERFLAG 'P'
#define MAKEQUERYFLAG 'Q'
#define DEVICEIDFLAG 'D'
#define PORTAFLAG 'A'
#define GETREGISTERFLAG 'G'

#define CONFIG_ENABLE_TIMEOUT_PROMPT 'E'
#define CONFIG_TIMEOUT_PROMPT 'T'

#define FORWARD_VAL 'F'
#define REVERSE_VAL 'R'
#define STATE1_VAL '1'
#define STATE2_VAL '2'

#define PARSING_ERROR_CHAR 'P'
#define RECEIVING_ERROR_CHAR 'R'
#define RCTIMEOUT_ERROR_CHAR 'T'
#define ENDCHAR_ERROR_CHAR 'E'
#define BAD_COMMAND_ERROR_CHAR 'B'
```

```

#define MOTORNUM 4
#define MOTORPORT PORTC
#define STEP1 0
#define DIRECTION1 1
#define STEP2 2
#define DIRECTION2 3
#define STEP3 6
#define DIRECTION3 7
#define STEP4 4
#define DIRECTION4 5

#define SWITCHPORT PORTB.4

#define TXBUFFERSIZE 25
#define PRESCALERDEFAULT 10

#pragma rambank 1
char TXBuffer[TXBUFFERSIZE];
char TXWordLength;
char TXBufferPos;

struct Motor {
    uns16 steps;
    bit direction;
    uns8 scaler;
} Motors[MOTORNUM];

#pragma rambank 2
char j;
char tempchar, test;
uns16 temp;

uns8 SwitchSetting;
char DutyCycleL;

char BufferOffset;
char RCCCommandPos;
char LastPORTA;
char PORTAChanges;
char MotorInterruptEnabledMask;
char MotorInterruptMask;
int HighADC;
char mask;
char Timer1StartH;
char Timer1StartL;
char MotorPrescaler;
char tempmask;

```

```

bit ReceivingChar;
bit RCCharReady;
bit DoneParsing;
bit ContinuingRC;
bit SuccessfulRC;
bit StepToggle;
bit ConfigReady;
bit NextTXCharReady;
#pragma rambank 0

#pragma codepage 2
bit TXNextBufferChar();
bit FillTXBuffer(const char *string, char wordsize);
bit AddTXBuffer(char ch);
#pragma codepage 0

#pragma origin 4 // start address of interrupt routine (14 bit core)

interrupt serverX(void) {
    int_save_registers // W, STATUS (and PCLATH if required)
        char sv_FSR = FSR;
    // handle the interrupt

    if (TMR1IF) {
        TMR1L = Timer1StartL;
        TMR1H = Timer1StartH;

        StepToggle = 1;
        TMR1IF = 0;
    } else if (RCIF && RCIE) {
        if (!ReceivingChar) {
            if (DoneParsing) {
                RCchar = RCREG;
                if ((RCchar) == STARTCHAR) {
                    ReceivingChar = 1;

                    RCCommandPos = -1;
                    BufferOffset = 0;
                    ContinuingRC = 1;
                    SuccessfulRC = 0;
                }
            } else {
                AddTXBuffer(PARSING_ERROR_CHAR);
            }
        } else {
            RCchar = RCREG;

```

```

    RCCharReady = 1;
    RCCommandPos++;
}
}
else if (RABIF) {
    if (RABIE) {

        PORTAChanges = LastPORTA^PORTA;
        LastPORTA = PORTA;

        if (PORTAChanges) {
            AddTXBuffer('C');
            j = 0;
            while (j < 6) {
                mask = 1 << j;
                if (PORTAChanges & mask) {
                    AddTXBuffer(j + '0');
                }
                j++;
            }
            MotorInterruptMask = PORTAChanges&MotorInterruptEnabledMask;
        }
    }
    test = PORTA;
    RABIF = 0;
}
else if (TXIF) {
    if (TXBufferPos < TXWordLength) {
        TXNextBufferChar();
    } else {
        TXIE = 0;
    }
    TXIF = 0;
}

FSR = sv_FSR;
int_restore_registers // W, STATUS (and PCLATH if required)
}

bit RCCommand(char bufferoffset); //waits for
void PMWSetup();
void TMR1Setup(char prescaler);
void PortInputSetup(unsigned char Ainputs, unsigned char Binputs, unsigned char
Cinputs); //changes ports to input. Output by default.
bit ParseCommand(char bufferoffset);
bit TakeMotorCommand(char bufferoffset);
bit TakeSwitchCommand(char bufferoffset);

```

```

bit TakeConfigCommand(char bufferoffset);
bit TakeVoltageCommand(char bufferoffset);
bit TakeQueryCommand(char bufferoffset);
void TakePartStep();

void main(void) {
    ReceivingChar = 0;
    DoneParsing = 1;
    ContinuingRC = 0;
    RCCharReady = 0;
    RCCommandPos = 0;

    SwitchSetting = 0;
    ConfigReady = 0;
    NextTXCharReady = 0;

    TXWordLength = 0;
    TXBufferPos = 0;

    DutyCycleL = 0b01101011;

    Motors[0].steps = 0;
    Motors[1].steps = 0;
    Motors[2].steps = 0;
    Motors[3].steps = 0;

    Motors[0].direction = 0;
    Motors[1].direction = 0;
    Motors[2].direction = 0;
    Motors[3].direction = 0;

    MotorInterruptEnabledMask = 0;
    MotorInterruptMask = 0;
    mask = 0;

    TRISC = 0b0000.0000; // 0=output; 1=input
    TRISB = 0b0000.0000; // 0=output; 1=input
    TRISA = 0xFF;
    LastPORTA = PORTA;

    Timer1StartH = 0xFF;
    Timer1StartL = 0;
    MotorPrescaler = PRESCALERDEFAULT;

    TMR1Setup(4);
    InterruptSetup(_RCIE | _TMR1IE | _TXIE);
    RABInterruptSetup(0b1111.1111, 0b0000.0000);

```

```

RS232Setup();

HighADC = CCP1L;

PORTA.2 = 0;

uns8 i;

for (;;) { // infinite loop

    if (ReceivingChar) {
        DoneParsing = 0;
        if (RCCharReady) {
            SuccessfulRC = RCCommand(BufferOffset);
            RCCharReady = 0;
            if (!SuccessfulRC) {
                AddTXBuffer(RECEIVING_ERROR_CHAR);

                ContinuingRC = 0;
                ReceivingChar = 0;
                DoneParsing = 1;
            }
        }
    } //end Receiving
    else {
        if (!DoneParsing) {

            for (i = BufferOffset - COMMANDSIZE; i < BufferOffset; i = i - COMMANDSIZE)
            {

                if (!ParseCommand(i)) {
                    AddTXBuffer(BAD_COMMAND_ERROR_CHAR);

                }
            }
            DoneParsing = 1;
        }

    } //end Parsing
    if (MotorInterruptMask) {
        for (i = 0; i < MOTORNUM; i++) {
            j = i + i;
            mask = 1 << (j);
            if (MotorInterruptMask & mask) {
                Motors[j].steps = 0;
                MotorInterruptMask &= !mask;
            }
            j = i + i + 1;
        }
    }
}

```

```

        mask = 1 << (j);
        if (MotorInterruptMask & mask) {
            Motors[j].steps = 0;
            MotorInterruptMask &= !mask;
        }
    }
    MotorInterruptMask = 0;
}
if (StepToggle) {

    TakePartStep();

    StepToggle = 0;
}
SWITCHPORT = SwitchSetting;
if (ConfigReady) {

}
} //end for
}

void PortInputSetup(unsigned char Ainputs, unsigned char Binputs, unsigned char
Cinputs) {
    TRISA = Ainputs;
    TRISB = Binputs;
    TRISC = Cinputs;
}

void TMR1Setup(char prescaler) {
    T1CON = 0;
    if (prescaler < 4) {
        T1CON = T1CON | (prescaler << 4);
    }
    T1CON = T1CON | 0b0000.0001;
}

void PMWSetup() {
    PIR1 = 0x00;
    PR2 = 0b10011011; // set this for 50Hz Servo PWM frequency
    // see page 129 of the datasheet to see how to configure this register(CCP1CON) properly
in order to use PWM.
    //it is configured as 1) single output; 2) PWM mode; 3) PWM mode; P1A, P1C active-high;
P1B, P1D active-high
    CCP1CON = 0b1000.1100;
    T2CON = 0b00000101; // prescaler = 16 + turn on TMR2(timer2)
    TMR2IF = 0; // clear this bit
}

```

```

ADCON0.1 = 1; //Start/Restart ADC
CCPR1L = 0b01101011;
}

bit RCCCommand(uns8 bufferoffset) {

    if ((bufferoffset + COMMANDSIZE) > RCBUFFERSIZE) {
        return 0;
    }
    if (RCCCommandPos < COMMANDSIZE) {

        uns8 n = bufferoffset + RCCCommandPos;

        RCBuffer[n] = RCchar;
        return 1;
    }

    if (RCCCommandPos == (COMMANDSIZE)) {
        if (RCchar == ENDCHAR) {
            ContinuingRC = 0;
            ReceivingChar = 0;
            BufferOffset = BufferOffset + COMMANDSIZE;
            return 1;
        } else if (RCchar == CONTINUECHAR) {
            ContinuingRC = 1;
            BufferOffset = BufferOffset + COMMANDSIZE;

            return 1;
        }
        AddTXBuffer('H');
    }
    AddTXBuffer(ENDCHAR_ERROR_CHAR);
    return 0;
}

bit ParseCommand(char bufferoffset) {
    tempchar = RCBuffer[bufferoffset];
    if (tempchar == MOTORFLAG) {
        return TakeMotorCommand(bufferoffset + 1);
    } else if (tempchar == SWITCHFLAG) {
        return TakeSwitchCommand(bufferoffset + 1);
    } else if (tempchar == CONFIGFLAG) {
        return TakeConfigCommand(bufferoffset + 1);
    } else if (tempchar == VOLTAGEFLAG) {
        return TakeVoltageCommand(bufferoffset + 1);
    } else if (tempchar == MAKEQUERYFLAG) {
        return TakeQueryCommand(bufferoffset + 1);
    }
}

```

```

}

return 0;
}

bit TakeMotorCommand(char bufferoffset) {
    char thismotornum = RCBuffer[bufferoffset] - 49;
    if ((thismotornum >= MOTORNUM)//by definition >0
    {
        return 0;
    }

    tempchar = RCBuffer[bufferoffset + 1];
    if (tempchar == FORWARD_VAL) {
        Motors[thismotornum].direction = 1;
    }
    else if (tempchar == REVERSE_VAL) {
        Motors[thismotornum].direction = 0;
    } else {
        return 0;
    }
    temp = ((long) RCBuffer[bufferoffset + 2]) << 8;
    temp |= RCBuffer[bufferoffset + 3];
    Motors[thismotornum].steps = temp;
    AddTXBuffer(CONFIGPRESCALERFLAG);
    tempchar = Motors[thismotornum].scaler;
    AddTXBuffer(tempchar);
    AddTXBuffer('M');
    AddTXBuffer(RCBuffer[bufferoffset + 2]);
    AddTXBuffer(RCBuffer[bufferoffset + 3]);
    Motors[thismotornum].scaler = 0;
    return 1;
}

bit TakeSwitchCommand(char bufferoffset) {
    if (RCBuffer[bufferoffset] == STATE1_VAL) {
        SwitchSetting = 0;
    }
    else if (RCBuffer[bufferoffset] == STATE2_VAL) {
        SwitchSetting = 1;
    } else {
        return 0;
    }
    return 1;
}

```

```

bit TakeConfigCommand(char bufferoffset) {
    tempchar = RCBuffer[bufferoffset];
    if (tempchar == CONFIGMOTORINTERRUPTSFLAG) {
        if (RCBuffer[bufferoffset + 1] == '1') {
            MotorInterruptEnabledMask |= 0b0000.0011;
        } else if (RCBuffer[bufferoffset + 1] == '0') {
            MotorInterruptEnabledMask &= 0b1111.1100;
        } else {
            return 0;
        }

        if (RCBuffer[bufferoffset + 2] == '1') {
            MotorInterruptEnabledMask |= 0b0000.1100;
        } else if (RCBuffer[bufferoffset + 2] == '0') {
            MotorInterruptEnabledMask &= 0b1111.0011;
        } else {
            return 0;
        }

        if (RCBuffer[bufferoffset + 3] == '1') {
            MotorInterruptEnabledMask |= 0b0011.0000;
        } else if (RCBuffer[bufferoffset + 3] == '0') {
            MotorInterruptEnabledMask &= 0b1100.1111;
        } else {
            return 0;
        }
        MotorInterruptMask &= MotorInterruptEnabledMask;
        return 1;

    } else if (tempchar == CONFIGSPEEDFLAG) {
        Timer1StartH = RCBuffer[bufferoffset + 1];
        Timer1StartL = RCBuffer[bufferoffset + 2];
    } else if (tempchar == CONFIGCHANGERABIEFLAG) {
        if (RCBuffer[bufferoffset + 2] == '1') {
            LastPORTA = PORTA;
            RABIF = 0;
            RABIE = 1;
        } else if (RCBuffer[bufferoffset + 2] == '0') {
            RABIE = 0;
        } else {
            return 0;
        }
    } else if (tempchar == CONFIGPRESCALERFLAG) {
        MotorPrescaler = RCBuffer[bufferoffset + 2];
    } else {
        return 0;
    }
}

```

```

    return 1;
}

bit TakeVoltageCommand(char bufferoffset) {

    DutyCycleL = (RCBuffer[bufferoffset]);

    return 1;
}

bit TakeQueryCommand(char bufferoffset) {
    tempchar = RCBuffer[bufferoffset];
    if (tempchar == MOTORFLAG) {
        AddTXBuffer('M');
        char n;
        for (n = 0; n < MOTORNUM; n++) {
            j = Motors[n].direction;
            if (j) {
                AddTXBuffer('F');
            } else {
                AddTXBuffer('R');
            }
            char offset = Motors;
            offset = offset + n + n + n + n + 1;
            FSR = (offset);
            AddTXBuffer(INDF);
            j = Motors[n].steps;
            AddTXBuffer(j);
        }
    } else if (tempchar == SWITCHFLAG) {
        AddTXBuffer(SWITCHFLAG);
        if (j) {
            AddTXBuffer(STATE1_VAL);
        } else {
            AddTXBuffer(STATE2_VAL);
        }
    } else if (tempchar == CONFIGFLAG) {
        if (RCBuffer[bufferoffset + 1] == CONFIGMOTORINTERRUPTSFLAG) {
            AddTXBuffer(CONFIGMOTORINTERRUPTSFLAG);
            AddTXBuffer(MotorInterruptEnabledMask);
        } else if (RCBuffer[bufferoffset + 1] == CONFIGCHANGERABIEFLAG) {
            AddTXBuffer(CONFIGCHANGERABIEFLAG);
            if (RABIE) {
                AddTXBuffer('1');
            } else {
                AddTXBuffer('0');
            }
        }
    }
}

```

```

    }
    } else if (RCBuffer[bufferoffset + 1] == CONFIGSPEEDFLAG) {
        AddTXBuffer(CONFIGSPEEDFLAG);
        AddTXBuffer(Timer1StartH);
        AddTXBuffer(Timer1StartL);
    }
    } else if (tempchar == VOLTAGEFLAG) {
        AddTXBuffer(VOLTAGEFLAG);
        AddTXBuffer(DutyCycleL);
    } else if (tempchar == PORTAFLAG) {
        AddTXBuffer(PORTAFLAG);
        AddTXBuffer(PORTA);
    } else if (tempchar == GETREGISTERFLAG) {
        char offset = RCBuffer[bufferoffset + 1];
        char FSRBankFlag = 0;
        bit IRPFlag = 0;

        if (RCBuffer[bufferoffset + 2] == '1') {
            IRPFlag = 1;
        }
        if (RCBuffer[bufferoffset + 3] == '1') {
            FSRBankFlag = 0b1000.0000;
        }

        AddTXBuffer(GETREGISTERFLAG);
        FSR = (offset) | FSRBankFlag;
        IRP = IRPFlag;
        AddTXBuffer(INDF);
    } else if (tempchar == DEVICEIDFLAG) {
        AddTXBuffer(DEVICEID_CHAR1);
        AddTXBuffer(DEVICEID_CHAR2);
    }
    }
    return 1;
}

void TakePartStep() {
    MOTORPORT.DIRECTION1 = Motors[0].direction;
    MOTORPORT.DIRECTION2 = Motors[1].direction;
    MOTORPORT.DIRECTION3 = Motors[2].direction;
    MOTORPORT.DIRECTION4 = Motors[3].direction;

    if (Motors[0].steps != 0) {
        if (MOTORPORT.STEP1) {
            MOTORPORT.STEP1 = 0;
        } else {
            MOTORPORT.STEP1 = 1;
            if (Motors[0].scaler == 0) {

```

```

        Motors[0].scaler = MotorPrescaler;
        Motors[0].steps--;
    } else {
        Motors[0].scaler--;
    }
}
}
if (Motors[1].steps != 0) {
    if (MOTORPORT.STEP2) {
        MOTORPORT.STEP2 = 0;
    } else {
        MOTORPORT.STEP2 = 1;
        if (Motors[1].scaler == 0) {
            Motors[1].scaler = MotorPrescaler;
            Motors[1].steps--;
        } else {
            Motors[1].scaler--;
        }
    }
}
if (Motors[2].steps != 0) {
    if (MOTORPORT.STEP3) {
        MOTORPORT.STEP3 = 0;
    } else {
        MOTORPORT.STEP3 = 1;
        if (Motors[2].scaler == 0) {
            Motors[2].scaler = MotorPrescaler;
            Motors[2].steps--;
        } else {
            Motors[2].scaler--;
        }
    }
}
if (Motors[3].steps != 0) {
    if (MOTORPORT.STEP4) {
        MOTORPORT.STEP4 = 0;
    } else {
        MOTORPORT.STEP4 = 1;

        if (Motors[3].scaler == 0) {
            Motors[3].scaler = MotorPrescaler;
            Motors[3].steps--;
        } else {
            Motors[3].scaler--;
        }
    }
}
}

```

```

}

}

bit FillTXBuffer(const char *string, char wordsize) {
    uns8 n = 0;
    uns8 offset = 0;
    uns8 newlength;

    if (TXBufferPos < TXWordLength) {
        offset = TXWordLength;
    } else {
        TXBufferPos = 0;
    }

    newlength = offset + wordsize;
    if ((newlength) > TXBUFFERSIZE) {
        return 0;
    }

    for (n = offset; n < wordsize; n++) {
        temp = string[n];
        TXBuffer[n] = temp;
    }
    TXWordLength = newlength;

    TXIE = 1;
    return 1;
}

bit TXNextBufferChar() {
    TXREG = TXBuffer[TXBufferPos];
    TXBufferPos++;
    return 1;
}

bit AddTXBuffer(char ch) {

    uns8 offset = 0;

    if (TXBufferPos < TXWordLength) {
        offset = TXWordLength;
    } else {
        TXBufferPos = 0;
    }

    if ((offset) > TXBUFFERSIZE) {

```

```

    return 0;
}

TXBuffer[offset] = ch;
TXWordLength = offset + 1;

TXIE = 1;
return 1;
}

```

InterruptSetup.h

```

#pragma codepage 1
//Interupt setup
#define _TOIE 0b0000.0000.0001
#define _INTE 0b0000.0000.0010
#define _RABIE 0b0000.0000.0100
#define _ADIE 0b0000.0000.1000
#define _RCIE 0b0000.0001.0000
#define _TXIE 0b0000.0010.0000
#define _SSPIE 0b0000.0100.0000
#define _CCP1IE 0b0000.1000.0000
#define _TMR2IE 0b0001.0000.0000
#define _TMR1IE 0b0010.0000.0000
#define _OSFIE 0b0100.0000.0000
#define _C2IE 0b1000.0000.0000
#define _C1IE 0b0001.0000.0000.0000
#define _EEIE 0b0010.0000.0000.0000

void InteruptSetup(uns16 InteruptFlags)// OR flags above together. No need to worry
about
{
    if (InteruptFlags) {
        GIE = 1;
        if (InteruptFlags & (_TOIE)) {
            TOIE = 1;
        }

        if (InteruptFlags & (_INTE)) {
            INTE = 1;
        }
    }
}

```

```

if (InteruptFlags & (_RABIE)) {
    RABIE = 1;
}
if (InteruptFlags > 8) {

    PEIE = 1;
    if (InteruptFlags & _ADIE) {

        ADIE = 1;

    }
    if (InteruptFlags & _RCIE) {
        RCIE = 1;
    }
    if (InteruptFlags & _TXIE) {
        TXIE = 1;
        TXIF = 0;
    }
    if (InteruptFlags & _SSPIE) {
        SSPIE = 1;
    }
    if (InteruptFlags & _CCP1IE) {
        CCP1IE = 1;
    }
    if (InteruptFlags & _TMR2IE) {
        TMR2IE = 1;
    }
    if (InteruptFlags & _TMR1IE) {
        TMR1IE = 1;
    }
    if (InteruptFlags & _OSFIE) {
        OSFIE = 1;
    }
    if (InteruptFlags & _C2IE) {
        C2IE = 1;
    }
    if (InteruptFlags & _C1IE) {
        C1IE = 1;
    }
    if (InteruptFlags & _EEIE) {
        EEIE = 1;
    }
}
}
}

```

```

void RABInterruptSetup(uns8 AInterruptFlags, uns8 BInterruptFlags)// OR flags above
together. No need to worry about
{
    IOCA = AInterruptFlags;
    IOCB = BInterruptFlags;
}

```

RS232Setup.c

```

//Assumes 4MHz clock and 9600 baud
#pragma codepage 1
#define Clock_4MHz
#define Baud9600 //sets baud rate using ifdef's

#ifndef Baud9600
#define UART_PERIOD_10_USEC 11
#define BRG16_SETTING 0 //setting up for 9600 baud assuming 4Mhz clock
#define BRGH_SETTING 1 //low speed bit
#define SPBRGH_SETTING 0 //upper part of period word
#define SPBRG_SETTING 25
#endif //end ifdef Baud9600

unsigned char RCchar;
unsigned char RCBuffer[10];

void RS232Setup(bit RXInterrupt, bit TXInterrupt) {
    TRISB.5 = 1;
    TRISB.7 = 0;

    ANSEL = 0;
    ANSELH = 0;

    //Sets the baud rate based on the #define baud_____
    BRG16 = BRG16_SETTING;
    BRGH = BRGH_SETTING;

    SPBRGH = SPBRGH_SETTING;
    SPBRG = SPBRG_SETTING;
    SYNC = 0; //asynchronous
    TXEN = 1; //enable transmission

    SPEN = 1; //enable USART
    CREN = 1; //enable receiver

    RCchar = RCREG;
    RCchar = RCREG;
    RCchar = RCREG;
}

```

```

    /*if(RXInterupt)
    {
        InteruptSetup(_RXIE)
    }
    if(TXInterupt)
    {
        InteruptSetup(_TXIE)
    }*/
}

void sendchar(char c) {

    while (TRMT != 1) {
    }

    TXREG = c;
}

bit waitForRC(unsigned char usec_10)
// Delays a multiple of 10 milliseconds at 4 MHz
{
    do {
        if (RCIF) {
            return 1;
        }
        usec_10--;
    } while (usec_10 != 0);
    return 0;
}

```

16F687_config.h

```
#asm
```

```

=====
;
; Configuration Bits
;
=====

_FCMEN_ON      EQU  H'3FFF'
_FCMEN_OFF     EQU  H'37FF'
_IESO_ON       EQU  H'3FFF'
_IESO_OFF      EQU  H'3BFF'
_BOR_ON        EQU  H'3FFF'
_BOR_NSLEEP    EQU  H'3EFF'
_BOR_SBODEN    EQU  H'3DFF'
_BOR_OFF       EQU  H'3CFF'
_CPD_ON        EQU  H'3F7F'
_CPD_OFF       EQU  H'3FFF'
_CP_ON         EQU  H'3FBF'
_CP_OFF        EQU  H'3FFF'
_MCLRE_ON      EQU  H'3FFF'
_MCLRE_OFF     EQU  H'3FDF'
_PWRTE_OFF     EQU  H'3FFF'
_PWRTE_ON      EQU  H'3FEF'
_WDT_ON        EQU  H'3FFF'
_WDT_OFF       EQU  H'3FF7'
_LP_OSC        EQU  H'3FF8'
_XT_OSC        EQU  H'3FF9'
_HS_OSC        EQU  H'3FFA'
_EC_OSC        EQU  H'3FFB'
_INTRC_OSC_NOCLKOUT EQU  H'3FFC'
_INTRC_OSC_CLKOUT EQU  H'3FFD'
_EXTRC_OSC_NOCLKOUT EQU  H'3FFE'
_EXTRC_OSC_CLKOUT EQU  H'3FFF'
_INTOSCIO      EQU  H'3FFC'
_INTOSC        EQU  H'3FFD'
_EXTRCIO       EQU  H'3FFE'
_EXTRC         EQU  H'3FFF'

#endasm

```

APPENDIX C: Multipurpose spectroscopy station SOP

SOP: Multipurpose Spectroscopy Station

1. Purpose:

- a. To define the safe operation of the Multipurpose Spectroscopy Station.

2. Safety

- a. This system uses a high power xenon lamp. This has invisible emission in the UV and IR. The light path is covered but care should be taken to ensure this covering is intact.

3. Quick Shutdown

- a. Turn off Motor Driver power supply
- b. Turn off the Lock-in power strip
- c. Turn off the Lamp power supply switch

4. Procedure:

a. Startup

- i. Turn on the Lock-in power strip
 1. Allow a few seconds to let the Lock-in start.
- ii. Turn on Motor Driver power supply
 1. Adjust the chopper speed as desired by rotating the knob on the chopper wheel control box. By depressing the knob, the speed will change quickly in the direction of the last knob turn. Note: speed setting can potentially change faster than chopper can accelerate.
- iii. Turn on the Lamp power supply switch
 1. Allow a few seconds for the Lamp Supply to start up then press the lamp start button.
 2. The lamp should start, indicated by white light leaking from the lamp housing and the power supply should read ~150W on the display.
 3. The output of the lamp will change significantly as it warms. For good results 15 minutes or more should be allowed for this output power to plateau.
- iv. Open Labview interface
 1. This can be found on the desktop labeled "USE THIS TO RUN QE".
 2. Press the run arrow to start the Labview program.
 3. Set current wavelength
 - a. A popup will request the current spectrometer wavelength in nm.

b. Read the wavelength from the back of the spectrometer and enter it in the popup.

i. If desired, a USB webcam is available to view the current spectrometer reading. To use, ensure the USB is plugged in and the illumination knob is turned all the way up. Use any web cam viewer you like to see the image (<https://webcamtoy.com/> for instance is a web based service).

c. It is critical that this is correct. Incorrect input at this stage will cause errors and potentially damage the equipment.

4. The program is now running but waiting for user input.

b. Manual Options

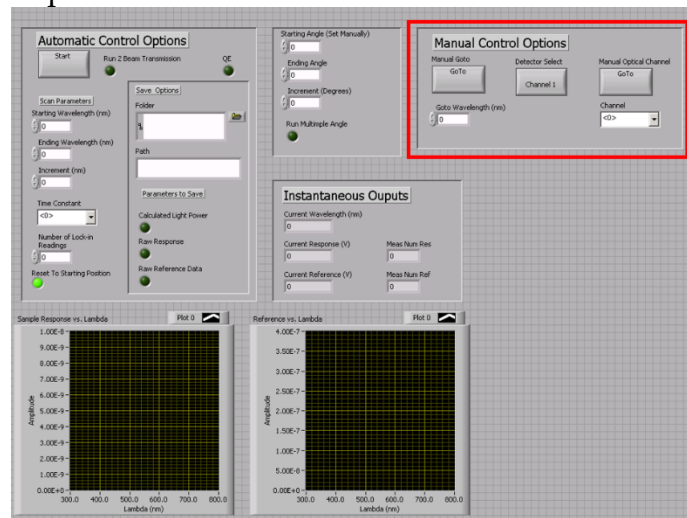


Figure 1: Highlighting the “Manual Control Options”

i. Three manual options are available, “Manual Goto”, “Detector Select”, and “Manual Optical Channel”.

1. “Manual Goto”

a. To set the spectrometer output to a desired wavelength, enter the desired wavelength in nm in the box below the “Manual Goto” button.

i. Acceptable range is 0-9000 nm. Settings outside this range can damage the equipment.

b. Press the “Manual Goto” button.

c. Observe the wavelength setting on the back of the spectrometer to ensure the setting is changing in the

desired direction and is not going past the setpoint. If either of these events occur it indicates improper setup and **you should power down the motor supply immediately.**

2. "Detector Select"

a. Press the "Detector Select" button to toggle between the two system detectors.

3. "Manual Optical Channel"

a. Select the desired optical channel (optical path) from the drop-down menu below the "Manual Optical Channel" button and press the "Manual Optical Channel" button.

c. Automatic options

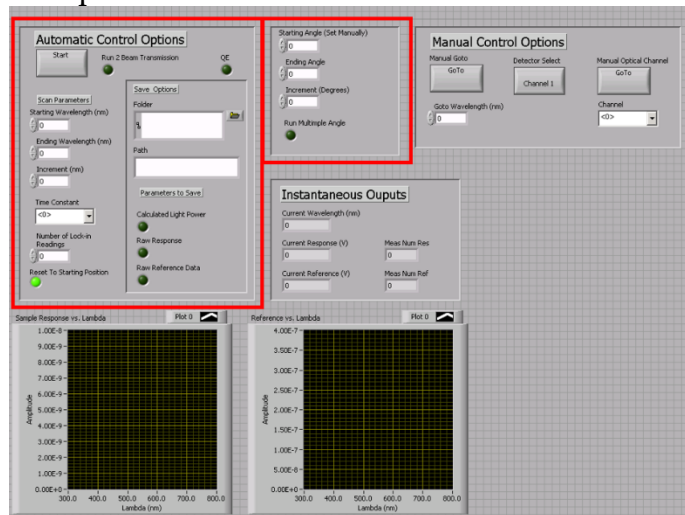


Figure 2: Highlighting the Automatic Control Options

i. These will be discussed in the relevant sections

d. Measuring QE

i. Measuring QE requires two measurements: one using a calibrated detector and one using the sample of interest.

ii. Calibrated detector run

1. Set automatic options

a. Turn on/off the light-up buttons as shown below

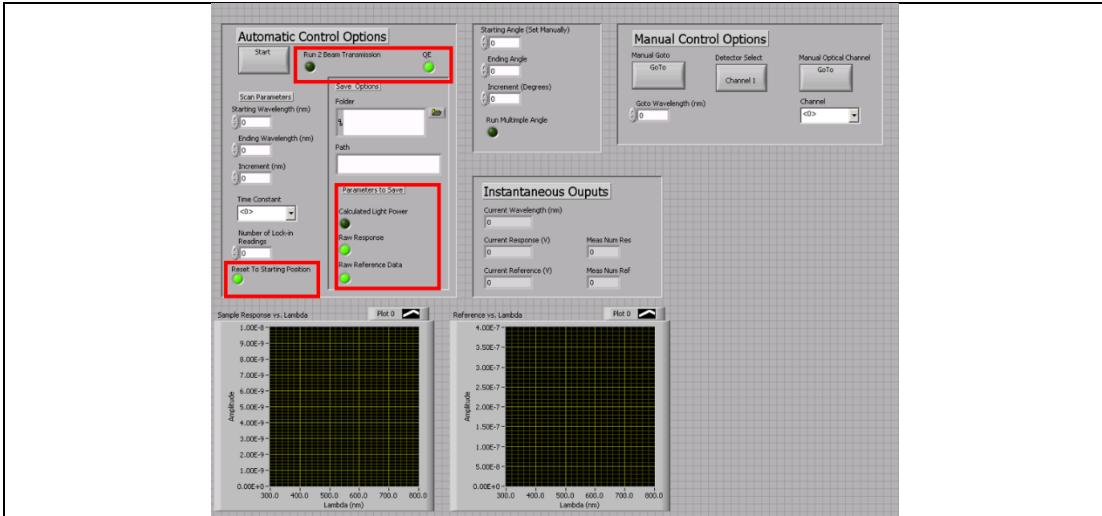


Figure 3: Highlighting settings for QE measurements.

- b. Press the folder icon to select a destination folder
 - c. Enter a descriptive name for the run under “Path”
 - d. Set the starting and ending wavelength. Starting must be less than ending.
 - e. Set the increment. This must be non-zero
 - f. Set the time constant. A shorter time constant allows the run to complete faster. A longer time constant gives higher precision. 1 s is a standard choice.
 - g. Set Number of Lock-in readings per measurement. Higher number give more precision but is slower. If possible it is better to increase integration time. Generally 1 should be entered here.
2. Set up calibrated detector
 - a. Connect a calibrated detector to the sample BNC cable.
 - b. Under “Manual Control Options” set the spectrometer to a visible wavelength and set the optical channel to “QE”.
 - c. Set the calibrated detector at the focal point of the light path. It is essential that the focal spot is on the detector only.
 3. Press the “Start” button and the equipment will automatically run.
 4. When the run is finished the program will ask for 2 files. These are unimportant at this time. Select any “.csv” file and with 2 columns for both of these.

5. Locate the saved file, open it, delete the last column, and save this file under a new name. This file will be used later.
- iii. Sample run
1. Setup the automatic settings as above.
 2. Replace the calibrated detector with the sample following the same procedure above.
 3. Press the “Start” button and the equipment will automatically run.
 4. The system will ask for a reference file. Select the file saved above.
 5. The system will ask for a calibration file. Select the responsivity calibration file for the calibrated detector used above.
- e. Integrating Sphere Measurements
- i. These measurements require two runs, a baseline run and a measurement run.
 - ii. Baseline Run
 1. Set automatic options
 - a. Turn on/off the light-up buttons as shown below

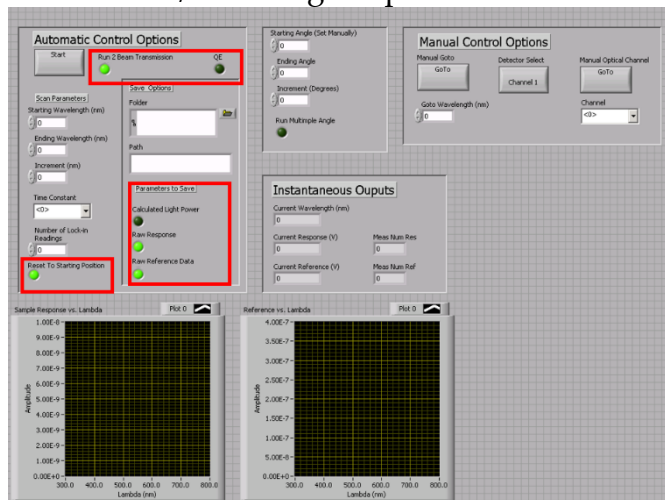


Figure 4: Highlighting settings for integrating sphere run.

- b. Press the folder icon to select a destination folder
- c. Enter a descriptive name for the run under “Path”
- d. Set the starting and ending wavelength. Starting must be less than ending.
- e. Set the increment. This must be non-zero

- f. Set the time constant. A shorter time constant allows the run to complete faster. A longer time constant gives higher precision.
 2. Connect the integrating sphere connector to the sample BNC cable.
 3. Press the "Start" button and the equipment will automatically run.
- iii. Sample run
1. Setup the automatic settings as above.
 2. Setup sample
 - a. **Note: ALWAYS wear gloves when opening the integrating sphere. Never let the white parts of the integrating sphere lid touch anything else. Any contact can damage the coating.**
 - b. For absorption measurements:
 - i. Remove the integrating sphere lid and place it carefully on the stand without touching any of the white parts to the stand.
 - ii. Clip the sample to the center post of the integrating sphere and carefully replace the integrating sphere lid. Note that the alignment studs on the lid must line up with the holes on the base.

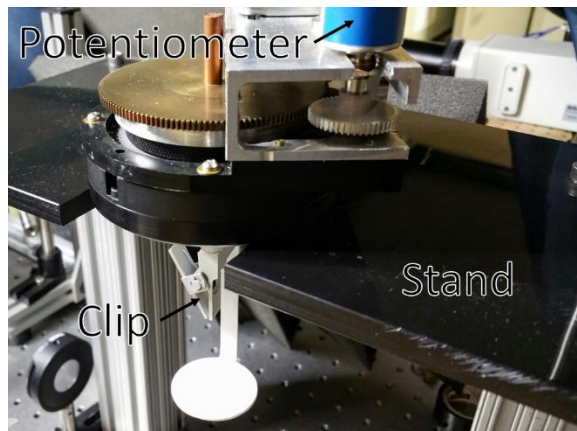


Figure 5: Image showing lid of integrating sphere on stand.

- iii. If a specific incident angle is required or if that angle must be accurately known, set up the angle measurement system.

1. Connect a multimeter to the top and middle electrodes of the potentiometer on the integrating sphere lid.
 2. If this is the first measurement of the day, find the zero angle potentiometer reading by rotating the gear on the lid until light shines directly back along its incident path. Excellent alignment is indicated by a reflected light spot hitting the exit of the monochromator.
 3. Set the desired incident angle using $8.26 \Omega/^\circ$.
 4. The minimum setting is 13 degrees in the counter clockwise direction.
- iv. If incident angle is not critical, manually align the incident beam.
1. remove a cap from the back of the sphere and use a mirror to see the light spot reflected from the sample. If there is no specularly reflected light skip to step 3 of this section.
 2. Move the reflected light spot using the dial on the top of the sphere until all of the specularly reflected light is counter-clockwise (seen from above) from the set of three ports that most closely face the beam. This should require ~12 degree offset from the center of the last port.
- v. With the monochromator set to a visible wavelength, peer through one of the integrating sphere ports and confirm that the light spot falls fully on the sample.
- vi. If not, either reduce the light spot size with the iris or remove the lid per i and ii of this section and move the sample slightly.
- c. For transmission measurements:
- i. Place the sample in the transmission clip at the front of the main port.
 - ii. Ensure light falls fully on the sample.
 - iii. If not, either reduce the light spot size with the iris or realign the sample.
3. Press the "Start" button and the equipment will automatically run.
4. Data can be analyzed by the following formulas:

$$\text{Absorption} = 1 - (\text{Trans. of Air} = 1) \frac{((\text{Sample})_{\text{Port1}})}{\left((\text{No Sample})_{\text{Port1}} * \frac{(\text{Sample})_{\text{Port2}}}{(\text{No Sample})_{\text{Port2}}} \right)}$$

$$\text{Transmission} = (\text{Trans. of Air} = 1) \frac{((\text{Sample})_{\text{Port1}})}{\left((\text{No Sample})_{\text{Port1}} * \frac{(\text{Sample})_{\text{Port2}}}{(\text{No Sample})_{\text{Port2}}} \right)}$$

Where port 1 and port 2 are the main port and secondary port respectively (these are labeled on the file names as well).

Bibliography

- [1] R. E. D. Book, “NREL,” *US Dep. Energy*, 2014.
- [2] Observ’ER, “Photovoltaic barometer,” *Syst. Sol. J. Photovoltaïque*, pp. 60–81, 2014.
- [3] “U.S. Solar Market Insight,” *SEIA*. [Online]. Available: <http://www.seia.org/research-resources/us-solar-market-insight>. [Accessed: 18-May-2016].
- [4] “Solar Market Insight Report 2016 Q2,” *SEIA*. [Online]. Available: <http://www.seia.org/research-resources/solar-market-insight-report-2016-q2>. [Accessed: 11-Jun-2016].
- [5] C. Breyer and A. Gerlach, “Global overview on grid-parity,” *Prog. Photovolt. Res. Appl.*, vol. 21, no. 1, pp. 121–136, Jan. 2013.
- [6] P. Y. Gan and Z. Li, “Quantitative study on long term global solar photovoltaic market,” *Renew. Sustain. Energy Rev.*, vol. 46, pp. 88–99, Jun. 2015.
- [7] N. S. Lewis, “Toward Cost-Effective Solar Energy Use,” *Science*, vol. 315, no. 5813, pp. 798–801, 2007.
- [8] T. Mai, M. M. Hand, S. F. Baldwin, R. H. Wiser, G. L. Brinkman, P. Denholm, D. J. Arent, G. Porro, D. Sandor, D. J. Hostick, M. Milligan, E. A. DeMeo, and M. Bazilian, “Renewable Electricity Futures for the United States,” *IEEE Trans. Sustain. Energy*, vol. 5, no. 2, pp. 372–378, Apr. 2014.
- [9] E. Yablonovitch, “Statistical ray optics,” *J. Opt. Soc. Am.*, vol. 72, no. 7, pp. 899–907, Jul. 1982.
- [10] J. N. Munday, D. M. Callahan, and H. A. Atwater, “Light trapping beyond the $4n^2$ limit in thin waveguides,” *Appl. Phys. Lett.*, vol. 100, no. 12, p. 121121, 2012.
- [11] Z. Yu, A. Raman, and S. Fan, “Fundamental limit of light trapping in grating structures,” *Opt. Express*, vol. 18, no. S3, pp. A366–A380, Sep. 2010.
- [12] H. A. Macleod, *Thin Film Optical Filters*. Bristol: Institute of Physics, 2001.
- [13] J. K. Kim, S. Chhajed, M. F. Schubert, E. F. Schubert, A. J. Fischer, M. H. Crawford, J. Cho, H. Kim, and C. Sone, “Light-Extraction Enhancement of GaInN Light-Emitting Diodes by Graded-Refractive-Index Indium Tin Oxide Anti-Reflection Contact,” *Adv. Mater.*, vol. 20, no. 4, pp. 801–804, Feb. 2008.
- [14] S. Chhajed, M. F. Schubert, J. K. Kim, and E. F. Schubert, “Nanostructured multilayer graded-index antireflection coating for Si solar cells with broadband and omnidirectional characteristics,” *Appl. Phys. Lett.*, vol. 93, no. 25, p. 251108, Dec. 2008.
- [15] S. R. Kennedy and M. J. Brett, “Porous broadband antireflection coating by glancing angle deposition,” *Appl. Opt.*, vol. 42, no. 22, pp. 4573–4579, Aug. 2003.
- [16] X. Yan, D. J. Poxson, J. Cho, R. E. Welsch, A. K. Sood, J. K. Kim, and E. F. Schubert, “Enhanced Omnidirectional Photovoltaic Performance of Solar Cells Using Multiple-Discrete-Layer Tailored- and Low-Refractive Index Anti-Reflection Coatings,” *Adv. Funct. Mater.*, vol. 23, no. 5, pp. 583–590, Feb. 2013.

- [17] A. Rahman, A. Ashraf, H. Xin, X. Tong, P. Sutter, M. D. Eisaman, and C. T. Black, "Sub-50-nm self-assembled nanotextures for enhanced broadband antireflection in silicon solar cells," *Nat. Commun.*, vol. 6, p. 5963, Jan. 2015.
- [18] H. M. Branz, V. E. Yost, S. Ward, K. M. Jones, B. To, and P. Stradins, "Nanostructured black silicon and the optical reflectance of graded-density surfaces," *Appl. Phys. Lett.*, vol. 94, no. 23, p. 231121, Jun. 2009.
- [19] A. Mahdjoub and L. Zighed, "New designs for graded refractive index antireflection coatings," *Thin Solid Films*, vol. 478, no. 1–2, pp. 299–304, May 2005.
- [20] J. A. Dobrowolski, D. Poitras, P. Ma, H. Vakil, and M. Acree, "Toward Perfect Antireflection Coatings: Numerical Investigation," *Appl. Opt.*, vol. 41, no. 16, p. 3075, Jun. 2002.
- [21] D. Poitras and J. A. Dobrowolski, "Toward Perfect Antireflection Coatings. 2. Theory," *Appl. Opt.*, vol. 43, no. 6, p. 1286, 2004.
- [22] K.-H. Kim and Q.-H. Park, "Perfect anti-reflection from first principles," *Sci. Rep.*, vol. 3, Jan. 2013.
- [23] V. E. Ferry, J. N. Munday, and H. A. Atwater, "Design Considerations for Plasmonic Photovoltaics," *Adv. Mater.*, vol. 22, no. 43, pp. 4794–4808, 2010.
- [24] G. W. Ford and W. H. Weber, "Electromagnetic interactions of molecules with metal surfaces," *Phys. Rep.*, vol. 113, no. 4, pp. 195–287, 1984.
- [25] J. Oh, H.-C. Yuan, and H. M. Branz, "An 18.2%-efficient black-silicon solar cell achieved through control of carrier recombination in nanostructures," *Nat. Nanotechnol.*, vol. 7, no. 11, pp. 743–748, Nov. 2012.
- [26] I.-K. Ding, J. Zhu, W. Cai, S.-J. Moon, N. Cai, P. Wang, S. M. Zakeeruddin, M. Grätzel, M. L. Brongersma, Y. Cui, and M. D. McGehee, "Plasmonic Dye-Sensitized Solar Cells," *Adv. Energy Mater.*, vol. 1, no. 1, pp. 52–57, Jan. 2011.
- [27] S. W. Sheehan, H. Noh, G. W. Brudvig, H. Cao, and C. A. Schmuttenmaer, "Plasmonic Enhancement of Dye-Sensitized Solar Cells Using Core–Shell–Shell Nanostructures," *J. Phys. Chem. C*, vol. 117, no. 2, pp. 927–934, Jan. 2013.
- [28] H. R. Stuart and D. G. Hall, "Island size effects in nanoparticle-enhanced photodetectors," *Appl. Phys. Lett.*, vol. 73, no. 26, pp. 3815–3817, 1998.
- [29] S. Pillai, K. R. Catchpole, T. Trupke, and M. A. Green, "Surface plasmon enhanced silicon solar cells," *J. Appl. Phys.*, vol. 101, no. 9, p. 93105, 2007.
- [30] A. Basch, F. J. Beck, T. Söderström, S. Varlamov, and K. R. Catchpole, "Combined plasmonic and dielectric rear reflectors for enhanced photocurrent in solar cells," *Appl. Phys. Lett.*, vol. 100, no. 24, p. 243903, Jun. 2012.
- [31] F. J. Beck, S. Mokkapati, and K. R. Catchpole, "Light trapping with plasmonic particles: beyond the dipole model," *Opt. Express*, vol. 19, no. 25, pp. 25230–25241, Dec. 2011.
- [32] H. R. Stuart and D. G. Hall, "Enhanced Dipole-Dipole Interaction between Elementary Radiators Near a Surface," *Phys. Rev. Lett.*, vol. 80, no. 25, pp. 5663–5666, Jun. 1998.
- [33] S.-S. Kim, S.-I. Na, J. Jo, D.-Y. Kim, and Y.-C. Nah, "Plasmon enhanced performance of organic solar cells using electrodeposited Ag nanoparticles," *Appl. Phys. Lett.*, vol. 93, no. 7, p. 73307, Aug. 2008.

- [34] N. C. Lindquist, W. A. Luhman, S.-H. Oh, and R. J. Holmes, “Plasmonic nanocavity arrays for enhanced efficiency in organic photovoltaic cells,” *Appl. Phys. Lett.*, vol. 93, no. 12, p. 123308, Sep. 2008.
- [35] A. J. Morfa, K. L. Rowlen, T. H. R. Iii, M. J. Romero, and J. van de Lagemaat, “Plasmon-enhanced solar energy conversion in organic bulk heterojunction photovoltaics,” *Appl. Phys. Lett.*, vol. 92, no. 1, p. 13504, Jan. 2008.
- [36] T. H. Reilly, III, J. van de Lagemaat, R. C. Tenent, A. J. Morfa, and K. L. Rowlen, “Surface-plasmon enhanced transparent electrodes in organic photovoltaics,” *Appl. Phys. Lett.*, vol. 92, no. 24, p. 243304, 2008.
- [37] C. Battaglia, C.-M. Hsu, K. Söderström, J. Escarré, F.-J. Haug, M. Charrière, M. Boccard, M. Despeisse, D. T. L. Alexander, M. Cantoni, Y. Cui, and C. Ballif, “Light Trapping in Solar Cells: Can Periodic Beat Random?,” *ACS Nano*, vol. 6, no. 3, pp. 2790–2797, Mar. 2012.
- [38] K. Vynck, M. Burrese, F. Riboli, and D. S. Wiersma, “Photon management in two-dimensional disordered media,” *Nat. Mater.*, Oct. 2012.
- [39] F. Pratesi, M. Burrese, F. Riboli, K. Vynck, and D. S. Wiersma, “Disordered photonic structures for light harvesting in solar cells,” *Opt. Express*, vol. 21, no. S3, p. A460, Apr. 2013.
- [40] S. J. Kim, P. Fan, J.-H. Kang, and M. L. Brongersma, “Creating semiconductor metafilms with designer absorption spectra,” *Nat. Commun.*, vol. 6, Jul. 2015.
- [41] M. L. Brongersma, Y. Cui, and S. Fan, “Light management for photovoltaics using high-index nanostructures,” *Nat. Mater.*, vol. 13, no. 5, pp. 451–460, May 2014.
- [42] L. Cao, P. Fan, A. P. Vasudev, J. S. White, Z. Yu, W. Cai, J. A. Schuller, S. Fan, and M. L. Brongersma, “Semiconductor Nanowire Optical Antenna Solar Absorbers,” *Nano Lett.*, vol. 10, no. 2, pp. 439–445.
- [43] E. Garnett and P. Yang, “Light Trapping in Silicon Nanowire Solar Cells,” *Nano Lett.*, vol. 10, no. 3, pp. 1082–1087.
- [44] R. Yan, D. Gargas, and P. Yang, “Nanowire photonics,” *Nat Photon*, vol. 3, no. 10, pp. 569–576, 2009.
- [45] J. Wallentin, N. Anttu, D. Asoli, M. Huffman, I. Åberg, M. H. Magnusson, G. Siefert, P. Fuss-Kailuweit, F. Dimroth, B. Witzigmann, H. Q. Xu, L. Samuelson, K. Deppert, and M. T. Borgström, “InP Nanowire Array Solar Cells Achieving 13.8% Efficiency by Exceeding the Ray Optics Limit,” *Science*, vol. 339, no. 6123, pp. 1057–1060, Mar. 2013.
- [46] K. Seo, M. Wober, P. Steinvurzel, E. Schonbrun, Y. Dan, T. Ellenbogen, and K. B. Crozier, “Multicolored Vertical Silicon Nanowires,” *Nano Lett.*, vol. 11, no. 4, pp. 1851–1856, Apr. 2011.
- [47] P. Krogstrup, H. I. Jørgensen, M. Heiss, O. Demichel, J. V. Holm, M. Aagesen, J. Nygard, and A. Fontcuberta i Morral, “Single-nanowire solar cells beyond the Shockley-Queisser limit,” *Nat. Photonics*, vol. 7, no. 4, pp. 306–310, Apr. 2013.
- [48] S. Arnold, D. Keng, S. I. Shopova, S. Holler, W. Zurawsky, and F. Vollmer, “Whispering gallery mode carousel? a photonic mechanism for enhanced nanoparticle detection in biosensing,” *Opt Express*, vol. 17, no. 8, pp. 6230–6238, 2009.

- [49] Y. Yao, J. Yao, V. K. Narasimhan, Z. Ruan, C. Xie, S. Fan, and Y. Cui, "Broadband light management using low-Q whispering gallery modes in spherical nanoshells," *Nat. Commun.*, vol. 3, p. 664, Feb. 2012.
- [50] J. Grandidier, D. M. Callahan, J. N. Munday, and H. A. Atwater, "Light Absorption Enhancement in Thin-Film Solar Cells Using Whispering Gallery Modes in Dielectric Nanospheres," *Adv. Mater.*, vol. 23, no. 10, pp. 1272–1276, Mar. 2011.
- [51] J. Zhu, C.-M. Hsu, Z. Yu, S. Fan, and Y. Cui, "Nanodome Solar Cells with Efficient Light Management and Self-Cleaning," *Nano Lett.*, vol. 10, no. 6, pp. 1979–1984, 2009.
- [52] B. Wang and P. W. Leu, "Enhanced absorption in silicon nanocone arrays for photovoltaics," *Nanotechnology*, vol. 23, no. 19, p. 194003, May 2012.
- [53] Z. Y. Wang, R. J. Zhang, S. Y. Wang, M. Lu, X. Chen, Y. X. Zheng, L. Y. Chen, Z. Ye, C. Z. Wang, and K. M. Ho, "Broadband optical absorption by tunable Mie resonances in silicon nanocone arrays," *Sci. Rep.*, vol. 5, Jan. 2015.
- [54] Z. Yu, A. Raman, and S. Fan, "Fundamental limit of nanophotonic light trapping in solar cells," *Proc. Natl. Acad. Sci.*, vol. 107, no. 41, pp. 17491–17496, 2010.
- [55] J. Gjessing, E. S. Marstein, and A. Sudb^o, "2D back-side diffraction grating for improved light trapping in thin silicon solar cells," *Opt Express*, vol. 18, no. 6, pp. 5481–5495.
- [56] J. Li, K. Li, C. Schuster, R. Su, X. Wang, B.-H. V. Borges, T. F. Krauss, and E. R. Martins, "Spatial resolution effect of light coupling structures," *Sci. Rep.*, vol. 5, p. 18500, Dec. 2015.
- [57] P. Campbell and M. A. Green, "The limiting efficiency of silicon solar cells under concentrated sunlight," *IEEE Trans. Electron Devices*, vol. 33, no. 2, pp. 234–239, 1986.
- [58] M. A. Green, "Lambertian light trapping in textured solar cells and light-emitting diodes: analytical solutions," *Prog. Photovolt. Res. Appl.*, vol. 10, no. 4, pp. 235–241, 2002.
- [59] H. R. Stuart and D. G. Hall, "Thermodynamic limit to light trapping in thin planar structures," *J Opt Soc Am A*, vol. 14, no. 11, pp. 3001–3008, 1997.
- [60] E. A. Schiff, "Thermodynamic limit to photonic-plasmonic light-trapping in thin films on metals," *J. Appl. Phys.*, vol. 110, no. 10, pp. 104501–104501–9, Nov. 2011.
- [61] D. M. Callahan, J. N. Munday, and H. A. Atwater, "Solar Cell Light Trapping beyond the Ray Optic Limit," *Nano Lett.*, vol. 12, no. 1, pp. 214–218, 2012.
- [62] M. S. Tomaš and Z. Lenac, "Decay of excited molecules in absorbing planar cavities," *Phys. Rev. A*, vol. 56, no. 5, pp. 4197–4206, Nov. 1997.
- [63] O. Di Stefano, N. Fina, S. Savasta, R. Girlanda, and M. Pieruccini, "Calculation of the local optical density of states in absorbing and gain media," *J. Phys. Condens. Matter Inst. Phys. J.*, vol. 22, no. 31, p. 315302, Aug. 2010.
- [64] K. H. Drexhage, "Influence of a dielectric interface on fluorescence decay time," *J. Lumin.*, vol. 1–2, pp. 693–701, 1970.
- [65] W. Lukosz and R. E. Kunz, "Light emission by magnetic and electric dipoles close to a plane interface. I. Total radiated power," *J. Opt. Soc. Am.*, vol. 67, no. 12, pp. 1607–1615, Dec. 1977.

- [66] J. E. Sipe, “The dipole antenna problem in surface physics: A new approach,” *Surf. Sci.*, vol. 105, no. 2–3, pp. 489–504, Apr. 1981.
- [67] M. S. Tomaš, “Green function for multilayers: Light scattering in planar cavities,” *Phys. Rev. A*, vol. 51, no. 3, pp. 2545–2559, Mar. 1995.
- [68] S. A. Maier, *Plasmonics: Fundamentals and Applications*. Springer, 2007.
- [69] Z. Yu, A. Raman, and S. Fan, “Thermodynamic Upper Bound on Broadband Light Coupling with Photonic Structures,” *Phys. Rev. Lett.*, vol. 109, no. 17, p. 173901, Oct. 2012.
- [70] D. Redfield, “Multiple-pass thin-film silicon solar cell,” *Appl. Phys. Lett.*, vol. 25, no. 11, pp. 647–648, 1974.
- [71] P. Campbell and M. A. Green, “Light trapping properties of pyramidally textured surfaces,” *J. Appl. Phys.*, vol. 62, no. 1, pp. 243–249, Jul. 1987.
- [72] U. Rau, U. W. Paetzold, and T. Kirchartz, “Thermodynamics of light management in photovoltaic devices,” *Phys. Rev. B*, vol. 90, no. 3, p. 35211, Jul. 2014.
- [73] J. N. Munday, “The effect of photonic bandgap materials on the Shockley-Queisser limit,” *J. Appl. Phys.*, vol. 112, no. 6, p. 64501, Sep. 2012.
- [74] M. Peters, J. C. Goldschmidt, and B. Bläsi, “Angular confinement and concentration in photovoltaic converters,” *Sol. Energy Mater. Sol. Cells*, vol. 94, no. 8, pp. 1393–1398, Aug. 2010.
- [75] F.-J. Haug, K. Söderström, A. Naqavi, J. Li, and C. Ballif, “Super-Lambertian photocurrent-generation in solar cells with periodically textured interfaces,” *Appl. Phys. Lett.*, vol. 103, no. 13, p. 131108, Sep. 2013.
- [76] S. Eyderman, S. John, and A. Deinega, “Solar light trapping in slanted conical-pore photonic crystals: Beyond statistical ray trapping,” *J. Appl. Phys.*, vol. 113, no. 15, p. 154315, Apr. 2013.
- [77] E. R. Martins, J. Li, Y. Liu, J. Zhou, and T. F. Krauss, “Engineering gratings for light trapping in photovoltaics: The supercell concept,” *Phys. Rev. B*, vol. 86, no. 4, p. 41404, Jul. 2012.
- [78] J. Gjessing, A. S. Sudbø, and E. S. Marstein, “Comparison of periodic light-trapping structures in thin crystalline silicon solar cells,” *J. Appl. Phys.*, vol. 110, no. 3, p. 33104, Aug. 2011.
- [79] A. Bozzola, M. Liscidini, and L. C. Andreani, “Photonic light-trapping versus Lambertian limits in thin film silicon solar cells with 1D and 2D periodic patterns,” *Opt. Express*, vol. 20, no. S2, pp. A224–A244, Mar. 2012.
- [80] V. E. Ferry, M. A. Verschuuren, M. C. van Lare, R. E. I. Schropp, H. A. Atwater, and A. Polman, “Optimized Spatial Correlations for Broadband Light Trapping Nanopatterns in High Efficiency Ultrathin Film a-Si:H Solar Cells,” *Nano Lett.*, vol. 11, no. 10, pp. 4239–4245, Oct. 2011.
- [81] S. Wiesendanger, M. Zilk, T. Pertsch, F. Lederer, and C. Rockstuhl, “A path to implement optimized randomly textured surfaces for solar cells,” *Appl. Phys. Lett.*, vol. 103, no. 13, p. 131115, Sep. 2013.
- [82] D. Ha, J. Murray, Z. Fang, L. Hu, and J. N. Munday, “Advanced Broadband Antireflection Coatings Based on Cellulose Microfiber Paper,” *IEEE J. Photovolt.*, vol. 5, no. 2, pp. 577–583, Mar. 2015.

- [83] C. Preston, Z. Fang, J. Murray, H. Zhu, J. Dai, J. N. Munday, and L. Hu, "Silver nanowire transparent conducting paper-based electrode with high optical haze," *J. Mater. Chem. C*, vol. 2, no. 7, pp. 1248–1254, Jan. 2014.
- [84] D. Ha, C. Gong, M. S. Leite, and J. N. Munday, "Dielectric micro-resonator arrays for optical coupling to solar cells," *Bull. Am. Phys. Soc.*, 2016.
- [85] "APS -APS March Meeting 2016 - Event - Measurement and Applications of Radiation Pressure," in *Bulletin of the American Physical Society*.
- [86] D. Ha, Z. Fang, L. Hu, and J. N. Munday, "Paper-Based Anti-Reflection Coatings for Photovoltaics," *Adv. Energy Mater.*, vol. 4, no. 9, Jun. 2014.
- [87] T. Gong and J. N. Munday, "Angle-Independent Hot Carrier Generation and Collection Using Transparent Conducting Oxides," *Nano Lett.*, vol. 15, no. 1, pp. 147–152, Jan. 2015.
- [88] Z. Fang, H. Zhu, Y. Yuan, D. Ha, S. Zhu, C. Preston, Q. Chen, Y. Li, X. Han, S. Lee, and others, "Novel nanostructured paper with ultrahigh transparency and ultrahigh haze for solar cells," *Nano Lett.*, vol. 14, no. 2, pp. 765–773, 2014.
- [89] E. M. Tennyson, J. L. Garrett, J. A. Frantz, J. D. Myers, R. Y. Bekele, J. S. Sanghera, J. N. Munday, and M. S. Leite, "Nanoimaging of Open-Circuit Voltage in Photovoltaic Devices," *Adv. Energy Mater.*, vol. 5, no. 23, Dec. 2015.
- [90] H. Tan, L. Sivec, B. Yan, R. Santbergen, M. Zeman, and A. H. M. Smets, "Improved light trapping in microcrystalline silicon solar cells by plasmonic back reflector with broad angular scattering and low parasitic absorption," *Appl. Phys. Lett.*, vol. 102, no. 15, p. 153902, Apr. 2013.
- [91] R. A. Pala, J. S. Q. Liu, E. S. Barnard, D. Askarov, E. C. Garnett, S. Fan, and M. L. Brongersma, "Optimization of non-periodic plasmonic light-trapping layers for thin-film solar cells," *Nat. Commun.*, vol. 4, Jul. 2013.
- [92] Y.-R. Lin, H.-P. Wang, C.-A. Lin, and J.-H. He, "Surface profile-controlled close-packed Si nanorod arrays for self-cleaning antireflection coatings," *J. Appl. Phys.*, vol. 106, no. 11, Dec. 2009.
- [93] K. X. Wang, Z. Yu, V. Liu, Y. Cui, and S. Fan, "Absorption enhancement in ultrathin crystalline silicon solar cells with antireflection and light-trapping nanocone gratings," *Nano Lett.*, vol. 12, no. 3, pp. 1616–1619, Mar. 2012.
- [94] A. Basch, F. Beck, T. Söderström, S. Varlamov, and K. R. Catchpole, "Enhanced light trapping in solar cells using snow globe coating," *Prog. Photovolt. Res. Appl.*, vol. 20, no. 7, pp. 837–842, 2012.
- [95] Z. Ouyang, X. Zhao, S. Varlamov, Y. Tao, J. Wong, and S. Pillai, "Nanoparticle-enhanced light trapping in thin-film silicon solar cells," *Prog. Photovolt. Res. Appl.*, vol. 19, no. 8, pp. 917–926, Dec. 2011.
- [96] B. G. Lee, P. Stradins, D. L. Young, K. Alberi, T.-K. Chuang, J. G. Couillard, and H. M. Branz, "Light trapping by a dielectric nanoparticle back reflector in film silicon solar cells," *Appl. Phys. Lett.*, vol. 99, no. 6, p. 64101, Aug. 2011.
- [97] B. Lipovšek, J. Krč, O. Isabella, M. Zeman, and M. Topič, "Modeling and optimization of white paint back reflectors for thin-film silicon solar cells," *J. Appl. Phys.*, vol. 108, no. 10, p. 103115, Nov. 2010.
- [98] W. E. Vargas, A. Amador, and G. A. Niklasson, "Diffuse reflectance of TiO₂ pigmented paints: Spectral dependence of the average pathlength parameter and

- the forward scattering ratio,” *Opt. Commun.*, vol. 261, no. 1, pp. 71–78, May 2006.
- [99] M. C. W. van Rossum and T. M. Nieuwenhuizen, “Multiple scattering of classical waves: microscopy, mesoscopy, and diffusion,” *Rev. Mod. Phys.*, vol. 71, no. 1, pp. 313–371, Jan. 1999.
- [100] P. Nitz, J. Ferber, R. Stangl, H. Rose Wilson, and V. Wittwer, “Simulation of multiply scattering media,” *Sol. Energy Mater. Sol. Cells*, vol. 54, no. 1–4, pp. 297–307, Jul. 1998.
- [101] W. E. Vargas, P. Greenwood, J. E. Otterstedt, and G. A. Niklasson, “Light Scattering in Pigmented Coatings:: Experiments and Theory,” *Sol. Energy*, vol. 68, no. 6, pp. 553–561, 2000.
- [102] A. Lin, S. M. Fu, Y. K. Zhong, C. W. Tseng, P. Y. Chen, and N. P. Ju, “The rigorous wave optics design of diffuse medium reflectors for photovoltaics,” *J. Appl. Phys.*, vol. 115, no. 15, p. 153105, Apr. 2014.
- [103] J. E. Cotter, “Optical intensity of light in layers of silicon with rear diffuse reflectors,” *J. Appl. Phys.*, vol. 84, no. 1, pp. 618–624, Jul. 1998.
- [104] M. A. Green, “Lambertian light trapping in textured solar cells and light-emitting diodes: analytical solutions,” *Prog. Photovolt. Res. Appl.*, vol. 10, no. 4, pp. 235–241, 2002.
- [105] E. Yablonovitch, “Statistical ray optics,” *J Opt Soc Am*, vol. 72, no. 7, pp. 899–907, 1982.
- [106] E. Yablonovitch and G. D. Cody, “Intensity enhancement in textured optical sheets for solar cells,” *IEEE Trans. Electron Devices*, vol. 29, no. 2, pp. 300–305, Feb. 1982.
- [107] C. L. Butner, J. B. Schutt, and M. C. Shai, “Comparison of the reflectance characteristics of polytetrafluoroethylene and barium sulfate paints,” *Appl. Opt.*, vol. 23, no. 8, pp. 1139–1140, Apr. 1984.
- [108] Z. Yu, N. P. Sergeant, T. Skauli, G. Zhang, H. Wang, and S. Fan, “Enhancing far-field thermal emission with thermal extraction,” *Nat. Commun.*, vol. 4, p. 1730, Apr. 2013.
- [109] C. C. Katsidis and D. I. Siapkas, “General Transfer-Matrix Method for Optical Multilayer Systems with Coherent, Partially Coherent, and Incoherent Interference,” *Appl. Opt.*, vol. 41, no. 19, pp. 3978–3987, Jul. 2002.
- [110] L. A. A. Pettersson, L. S. Roman, and O. Inganäs, “Modeling photocurrent action spectra of photovoltaic devices based on organic thin films,” *J. Appl. Phys.*, vol. 86, no. 1, pp. 487–496, Jul. 1999.
- [111] E. Centurioni, “Generalized matrix method for calculation of internal light energy flux in mixed coherent and incoherent multilayers,” *Appl. Opt.*, vol. 44, no. 35, p. 7532, Dec. 2005.
- [112] V. Liu and S. Fan, “S4 : A free electromagnetic solver for layered periodic structures,” *Comput. Phys. Commun.*, vol. 183, no. 10, pp. 2233–2244, Oct. 2012.
- [113] J. Grandidier, D. M. Callahan, J. N. Munday, and H. A. Atwater, “Light Absorption Enhancement in Thin-Film Solar Cells Using Whispering Gallery Modes in Dielectric Nanospheres,” *Adv. Mater.*, vol. 23, no. 10, pp. 1272–1276, Mar. 2011.

- [114] A. Abass, C. Trompoukis, S. Leyre, M. Burgelman, and B. Maes, “Modeling combined coherent and incoherent scattering structures for light trapping in solar cells,” *J. Appl. Phys.*, vol. 114, no. 3, p. 33101, Jul. 2013.
- [115] J. D. Joannopoulos, S. G. Johnson, J. N. Winn, and R. D. Meade, *Photonic Crystals: Molding the Flow of Light (Second Edition)*. Princeton University Press, 2011.
- [116] Z. Yu, A. Raman, and S. Fan, “Fundamental limit of nanophotonic light trapping in solar cells,” *Proc. Natl. Acad. Sci.*, Sep. 2010.
- [117] E. A. Schiff, “Thermodynamic limit to photonic-plasmonic light-trapping in thin films on metals,” *J. Appl. Phys.*, vol. 110, no. 10, pp. 104501–9, 2011.
- [118] J. Murray and J. N. Munday, “Experimental demonstration and modeling of the internal light scattering profile within solar cells due to random dielectric scatterers,” *J. Appl. Phys.*, vol. 119, no. 2, p. 23104, Jan. 2016.
- [119] C. L. Mitsas and D. I. Siapkas, “Generalized matrix method for analysis of coherent and incoherent reflectance and transmittance of multilayer structures with rough surfaces, interfaces, and finite substrates,” *Appl. Opt.*, vol. 34, no. 10, p. 1678, Apr. 1995.
- [120] W. E. Vargas and G. A. Niklasson, “Generalized method for evaluating scattering parameters used in radiativetransfer models,” *J. Opt. Soc. Am. A*, vol. 14, no. 9, pp. 2243–2252, Sep. 1997.
- [121] W. E. Vargas, P. Greenwood, J. E. Otterstedt, and G. A. Niklasson, “Light Scattering in Pigmented Coatings:: Experiments and Theory,” *Sol. Energy*, vol. 68, no. 6, pp. 553–561, 2000.
- [122] G. E. Jellison, “Optical functions of GaAs, GaP, and Ge determined by two-channel polarization modulation ellipsometry,” *Opt. Mater.*, vol. 1, no. 3, pp. 151–160, Sep. 1992.
- [123] H. A. Atwater and A. Polman, “Plasmonics for improved photovoltaic devices,” *Nat Mater*, vol. 9, no. 3, pp. 205–213, 2010.
- [124] F. Bloisi, P. Terrecuso, L. Vicari, and F. Simoni, “Voltage Controlled Light Transmittance in Polymer Dispersed Liquid Crystals,” *Mol. Cryst. Liq. Cryst. Sci. Technol. Sect. Mol. Cryst. Liq. Cryst.*, vol. 266, no. 1, pp. 229–239, Jun. 1995.
- [125] K. R. Catchpole and A. Polman, “Design principles for particle plasmon enhanced solar cells,” *Appl. Phys. Lett.*, vol. 93, no. 19, p. 191113, 2008.
- [126] C.-C. Chen, L. Dou, R. Zhu, C.-H. Chung, T.-B. Song, Y. B. Zheng, S. Hawks, G. Li, P. S. Weiss, and Y. Yang, “Visibly Transparent Polymer Solar Cells Produced by Solution Processing,” *ACS Nano*, vol. 6, no. 8, pp. 7185–7190, Aug. 2012.
- [127] R. Betancur, P. Romero-Gomez, A. Martinez-Otero, X. Elias, M. Maymó, and J. Martorell, “Transparent polymer solar cells employing a layered light-trapping architecture,” *Nat. Photonics*, vol. 7, no. 12, pp. 995–1000, Dec. 2013.
- [128] H. Zhang, S. Jenatsch, J. De Jonghe, F. Nüesch, R. Steim, A. C. Véron, and R. Hany, “Transparent Organic Photodetector using a Near-Infrared Absorbing Cyanine Dye,” *Sci. Rep.*, vol. 5, p. 9439, Mar. 2015.

- [129] Y. Zhao and R. R. Lunt, “Transparent Luminescent Solar Concentrators for Large-Area Solar Windows Enabled by Massive Stokes-Shift Nanocluster Phosphors,” *Adv. Energy Mater.*, vol. 3, no. 9, pp. 1143–1148, Sep. 2013.
- [130] Y. Zhao, G. A. Meek, B. G. Levine, and R. R. Lunt, “Near-Infrared Harvesting Transparent Luminescent Solar Concentrators,” *Adv. Opt. Mater.*, vol. 2, no. 7, pp. 606–611, Jul. 2014.
- [131] M. G. Debije, “Solar Energy Collectors with Tunable Transmission,” *Adv. Funct. Mater.*, vol. 20, no. 9, pp. 1498–1502, May 2010.
- [132] H. Khandelwal, R. C. G. M. Loonen, J. L. M. Hensen, M. G. Debije, and A. P. H. J. Schenning, “Electrically switchable polymer stabilised broadband infrared reflectors and their potential as smart windows for energy saving in buildings,” *Sci. Rep.*, vol. 5, p. 11773, Jul. 2015.
- [133] K.-S. Ahn, S. J. Yoo, M.-S. Kang, J.-W. Lee, and Y.-E. Sung, “Tandem dye-sensitized solar cell-powered electrochromic devices for the photovoltaic-powered smart window,” *J. Power Sources*, vol. 168, no. 2, pp. 533–536, Jun. 2007.
- [134] T. Ameri, G. Dennler, C. Waldauf, H. Azimi, A. Seemann, K. Forberich, J. Hauch, M. Scharber, K. Hingerl, and C. J. Brabec, “Fabrication, Optical Modeling, and Color Characterization of Semitransparent Bulk-Heterojunction Organic Solar Cells in an Inverted Structure,” *Adv. Funct. Mater.*, vol. 20, no. 10, pp. 1592–1598, May 2010.
- [135] F. Guo, T. Ameri, K. Forberich, and C. J. Brabec, “Semitransparent polymer solar cells,” *Polym. Int.*, vol. 62, no. 10, pp. 1408–1412, Oct. 2013.
- [136] K.-S. Chen, J.-F. Salinas, H.-L. Yip, L. Huo, J. Hou, and A. K.-Y. Jen, “Semitransparent polymer solar cells with 6% PCE, 25% average visible transmittance and a color rendering index close to 100 for power generating window applications,” *Energy Environ. Sci.*, vol. 5, no. 11, pp. 9551–9557, Oct. 2012.
- [137] G. E. Eperon, V. M. Burlakov, A. Goriely, and H. J. Snaith, “Neutral Color Semitransparent Microstructured Perovskite Solar Cells,” *ACS Nano*, vol. 8, no. 1, pp. 591–598, Jan. 2014.
- [138] F. Guo, S. Chen, Z. Chen, H. Luo, Y. Gao, T. Przybilla, E. Spiecker, A. Osvet, K. Forberich, and C. J. Brabec, “Printed Smart Photovoltaic Window Integrated with an Energy-Saving Thermochromic Layer,” *Adv. Opt. Mater.*, vol. 3, no. 11, pp. 1524–1529, Nov. 2015.
- [139] H. Jin, J. Qian, L. Zhou, J. Yuan, H. Huang, Y. Wang, W. M. Tang, and H. L. W. Chan, “Suppressing the Coffee-Ring Effect in Semitransparent MnO₂ Film for a High-Performance Solar-Powered Energy Storage Window,” *ACS Appl. Mater. Interfaces*, vol. 8, no. 14, pp. 9088–9096, Apr. 2016.
- [140] W. Yu, X. Jia, Y. Long, L. Shen, Y. Liu, W. Guo, and S. Ruan, “Highly Efficient Semitransparent Polymer Solar Cells with Color Rendering Index Approaching 100 Using One-Dimensional Photonic Crystal,” *ACS Appl. Mater. Interfaces*, vol. 7, no. 18, pp. 9920–9928, May 2015.
- [141] R. Baetens, B. P. Jelle, and A. Gustavsen, “Properties, requirements and possibilities of smart windows for dynamic daylight and solar energy control in buildings: A state-of-the-art review,” *Sol. Energy Mater. Sol. Cells*, vol. 94, no. 2, pp. 87–105, Feb. 2010.

- [142] L. L. Min-Hsin Yeh, "Motion-Driven Electrochromic Reactions for Self-Powered Smart Window System," *ACS Nano*, vol. 9, no. 5, 2015.
- [143] A. Piccolo, "Thermal performance of an electrochromic smart window tested in an environmental test cell," *Energy Build.*, vol. 42, no. 9, pp. 1409–1417, Sep. 2010.
- [144] J. Wang, L. Zhang, L. Yu, Z. Jiao, H. Xie, X. W. (David) Lou, and X. Wei Sun, "A bi-functional device for self-powered electrochromic window and self-rechargeable transparent battery applications," *Nat. Commun.*, vol. 5, p. 4921, Sep. 2014.
- [145] C. M. Lampert, "Large-area smart glass and integrated photovoltaics," *Sol. Energy Mater. Sol. Cells*, vol. 76, no. 4, pp. 489–499, Apr. 2003.
- [146] Y. Gao, H. Luo, Z. Zhang, L. Kang, Z. Chen, J. Du, M. Kanehira, and C. Cao, "Nanoceramic VO₂ thermochromic smart glass: A review on progress in solution processing," *Nano Energy*, vol. 1, no. 2, pp. 221–246, Mar. 2012.
- [147] H. Kim, Y. Kim, K. S. Kim, H. Y. Jeong, A.-R. Jang, S. H. Han, D. H. Yoon, K. S. Suh, H. S. Shin, T. Kim, and W. S. Yang, "Flexible Thermochromic Window Based on Hybridized VO₂/Graphene," *ACS Nano*, vol. 7, no. 7, pp. 5769–5776, Jul. 2013.
- [148] J. Zhu, Y. Zhou, B. Wang, J. Zheng, S. Ji, H. Yao, H. Luo, and P. Jin, "Vanadium Dioxide Nanoparticle-based Thermochromic Smart Coating: High Luminous Transmittance, Excellent Solar Regulation Efficiency, and Near Room Temperature Phase Transition," *ACS Appl. Mater. Interfaces*, vol. 7, no. 50, pp. 27796–27803, Dec. 2015.
- [149] Y. Kim, D. Jung, S. Jeong, K. Kim, W. Choi, and Y. Seo, "Optical properties and optimized conditions for polymer dispersed liquid crystal containing UV curable polymer and nematic liquid crystal," *Curr. Appl. Phys.*, vol. 15, no. 3, pp. 292–297, 2015.
- [150] S. Park and J. W. Hong, "Polymer dispersed liquid crystal film for variable-transparency glazing," *Thin Solid Films*, vol. 517, no. 10, pp. 3183–3186, Mar. 2009.
- [151] D. J. Gardiner, S. M. Morris, and H. J. Coles, "High-efficiency multistable switchable glazing using smectic A liquid crystals," *Sol. Energy Mater. Sol. Cells*, vol. 93, no. 3, pp. 301–306, Mar. 2009.
- [152] H.-K. Kwon, K.-T. Lee, K. Hur, S. H. Moon, M. M. Quasim, T. D. Wilkinson, J.-Y. Han, H. Ko, I.-K. Han, B. Park, B. K. Min, B.-K. Ju, S. M. Morris, R. H. Friend, and D.-H. Ko, "Optically Switchable Smart Windows with Integrated Photovoltaic Devices," *Adv. Energy Mater.*, vol. 5, no. 3, p. n/a-n/a, Feb. 2015.
- [153] S. C. Sekhar and K. Lim Cher Toon, "On the study of energy performance and life cycle cost of smart window," *Energy Build.*, vol. 28, no. 3, pp. 307–316, Nov. 1998.
- [154] D. Cupelli, F. Pasquale Nicoletta, S. Manfredi, M. Vivacqua, P. Formoso, G. De Filpo, and G. Chidichimo, "Self-adjusting smart windows based on polymer-dispersed liquid crystals," *Sol. Energy Mater. Sol. Cells*, vol. 93, no. 11, pp. 2008–2012, Nov. 2009.
- [155] A. Cannavale, M. Manca, L. De Marco, R. Grisorio, S. Carallo, G. P. Suranna, and G. Gigli, "Photovoltachromic Device with a Micropatterned Bifunctional

- Counter Electrode,” *ACS Appl. Mater. Interfaces*, vol. 6, no. 4, pp. 2415–2422, Feb. 2014.
- [156] J. W. Doane, N. A. Vaz, B.-G. Wu, and S. Žumer, “Field controlled light scattering from nematic microdroplets,” *Appl. Phys. Lett.*, vol. 48, no. 4, pp. 269–271, Jan. 1986.
- [157] J. A. Firehammer, G. P. Crawford, and N. M. Lawandy, “Voltage-controlled lasing pixels for projection display,” *Appl. Phys. Lett.*, vol. 73, no. 5, pp. 590–592, Aug. 1998.
- [158] T. L. Chiu, W. F. Chang, C. C. Wu, C. F. Lin, J. Y. Lee, S. W. Liu, C. T. Chen, and J. H. Lee, “Tandem Organic Light-Emitting Diode and Organic Photovoltaic Device Inside Polymer Dispersed Liquid Crystal Cell,” *J. Disp. Technol.*, vol. 9, no. 10, pp. 787–793, Oct. 2013.
- [159] H. Hosseinzadeh, K. Liew, Y. Han, N. Mohieddin, and I. a Goldthorpe, “Silver nanowire transparent electrodes for liquid crystal-based smart windows,” *Sol. Energy Mater. Sol. Cells*, vol. 132, pp. 337–341, 2015.
- [160] K. Joulain, J.-P. Mulet, F. Marquier, R. Carminati, and J.-J. Greffet, “Surface electromagnetic waves thermally excited: Radiative heat transfer, coherence properties and Casimir forces revisited in the near field,” *Surf. Sci. Rep.*, vol. 57, no. 3–4, pp. 59–112, 2005.
- [161] D. A. Higgins, “Probing the Mesoscopic Chemical and Physical Properties of Polymer-Dispersed Liquid Crystals,” *Adv. Mater.*, vol. 12, no. 4, pp. 251–264, Feb. 2000.
- [162] J. Murray and J. N. Munday, “A generalized approach to modeling absorption and photocurrent in solar cells with light scattering structures,” 2016.
- [163] P. S. Drzaic, *Liquid Crystal Dispersions*. WORLD SCIENTIFIC, 1995.
- [164] M. A. Green, K. Emery, Y. Hishikawa, W. Warta, and E. D. Dunlop, “Solar cell efficiency tables (Version 45),” *Prog. Photovolt. Res. Appl.*, vol. 23, no. 1, pp. 1–9, Jan. 2015.
- [165] T. Matsui, H. Sai, T. Suezaki, M. Matsumoto, K. Saito, I. Yoshida, and M. Kondo, “Development of highly stable and efficient amorphous silicon based solar cells,” *Proc. 28th EU PVSEC*, pp. 2213–2217, 2013.
- [166] L. T. Sharpe, A. Stockman, W. Jagla, and H. Jagle, “A luminous efficiency function, $V^*(\lambda)$, for daylight adaptation,” *J. Vis.*, vol. 5, no. 11, pp. 3–3, Dec. 2005.
- [167] P. S. Drzaic, “Droplet density, droplet size, and wavelength effects in PDLC light scattering,” *Mol. Cryst. Liq. Cryst. Sci. Technol. Sect. Mol. Cryst. Liq. Cryst.*, vol. 261, no. 1, pp. 383–392, Mar. 1995.
- [168] F. Guo, T. Ameri, K. Forberich, and C. J. Brabec, “Semitransparent polymer solar cells,” *Polym. Int.*, vol. 62, no. 10, pp. 1408–1412, Oct. 2013.
- [169] R. R. Lunt and V. Bulovic, “Transparent, near-infrared organic photovoltaic solar cells for window and energy-scavenging applications,” *Appl. Phys. Lett.*, vol. 98, p. 113305, Mar. 2011.